Improving Accuracy and Precision in Biological Applications of Fluorescence Lifetime Imaging Microscopy

by

Ching-Wei Chang

A dissertation submitted in partial fulfillment
of the requirements for the degree of
Doctor of Philosophy
(Biomedical Engineering)
in The University of Michigan
2009

Doctoral Committee:

Associate Professor Mary-Ann Mycek, Chair
Professor Scott J. Hollister
Professor Nicholas Kotov
Associate Professor Shuichi Takayama

Acknowledgements

First, I would like to thank Dr. Mary-Ann Mycek for providing me plenty of advices on this work. She gave me correct research directions while still giving me sufficient freedom to conduct detailed experiments and analyses. I definitely cannot complete this work without her great support and help.

I also would like to thank Dr. Hollister, Dr. Kotov, and Dr. Takayama for participating in the dissertation committee and providing me very useful advices.

I want to thank previous Mycek lab members Dr. Wei Zhong and Dr. Dhruv Sud for their helpful discussions on FLIM techniques and experiments. I also want to thank the members from our collaborating lab Dr. Sofia Merajver, Dr. Mei Wu, Dr. Zhi-Fen Wu, Devin Rosenthal, and Elliot Rhee for their work and discussions on the RhoC project. They all contribute a lot to this work.

In addition, I need to thank Dr. Selim Esedoglu in the Department of Mathematics for his class and advices on image processing, which provided me the basis to do further advanced analyses.

Finally, I want to thank my parents. I am very grateful to them for raising me and providing me support in all these years that let me concentrate on my Ph.D. work without worrying them.

Table of contents

List of Figures

List of Tables

List of Abbreviations

α: the pre-exponential term in fluorescence decay equations

C: ECFP, enhanced cyan fluorescent protein

Ce: Cerulean

Cit: Citrine

conROF: constrained Rudin-Osher-Fatemi total variation model

delt: the time interval (between two consecutive iterations) used in denoising

dt: the time interval between the beginning time points of two consecutive gates

f: the acquired image, corrupted by noise

fid: *λ*, the fidelity constant (or coefficient) used in total variation models

FLIM: fluorescence lifetime imaging microscopy

FRET: Förster (fluorescence) resonance energy transfer

FWTV: *f*-weighted total variation model

g: gate width

G: gain = counts/photon counts, but used as variance/*N* in general

Γ : radiative decay rate constant

GDI: RhoGDIγ, or Rho Guanine nucleotide Dissociation Inhibitor gamma

I(t): fluorescence intensity, as a function of time

IC: initial condition

k : non-radiative decay rate constant

k_T: energy transfer rate constant

λ: *fid*, the fidelity constant (or coefficient) used in total variation models

m': the 1st dimension (the number of rows) of an image

mc: the number of iterations for Monte Carlo simulations

MC: Monte Carlo

n: number of samples for statistical analysis

n: number of gates in gated FLIM

N: local mean intensity counts (from pixels with the same mean source photon counts)

N(t): the number of fluorescent molecules in the first excited state, as a function of time

n': the 2nd dimension (the number of columns) of an image

n_{avg}: number of averaged images

ND: neutral density filter

n_{pix}: number of pixels

nt: the number of time steps (i.e. iterations) used in denoising

o: the original, uncorrupted image

PC: photon counts

PoissTV: Poisson-noise adapted total variation model

Q: quantum yield

RC: RhoC, or Ras Homology Protein C

RhoC: Ras Homology Protein C

RhoGDIγ: Rho Guanine nucleotide Dissociation Inhibitor gamma

RME: relative mean error %, defined as [(mean value – correct value) / correct value] × 100

ROF: Rudin-Osher-Fatemi total variation model

ROI: region of interest

RSD: relative standard deviation %, defined as [standard deviation / mean value] × 100

SNR: signal-to-noise ratio

std.: standard deviation

τ: fluorescence lifetime

TV: total variation

u: the image created along or after denoising process

UWTV: u-weighted total variation model

var.: variance

Y: EYFP, enhanced yellow fluorescent protein

Abstract

The quantitative understanding of cellular and molecular responses in living cells is important for many reasons, including identifying potential molecular targets for treatments of diseases like cancer. Fluorescence lifetime imaging microscopy (FLIM) can quantitatively measure these responses in living cells by producing spatially resolved images of fluorophore lifetime, and has advantages over intensity-based measurements. However, in live-cell microscopy applications using high-intensity light sources such as lasers, maintaining biological viability remains critical. Although high-speed, time-gated FLIM significantly reduces light delivered to live cells, making measurements at low light levels remains a challenge affecting quantitative FLIM results.

We can significantly improve both accuracy and precision in gated FLIM applications. We use fluorescence resonance energy transfer (FRET) with fluorescent proteins to detect molecular interactions in living cells: the use of FLIM, better fluorophores, and temperature / CO_2 controls can improve live-cell FRET results with higher consistency, better statistics, and less non-specific FRET (for negative control comparisons, *p*-value = 0.93 (physiological) vs. 9.43E-05 (non-physiological)). Several lifetime determination methods are investigated to optimize gating schemes. We demonstrate a reduction in relative standard deviation (RSD) from 52.57% to 18.93% with optimized gating in an example under typical experimental conditions. We develop two novel total variation (TV) image denoising algorithms, FWTV (*f*-weighted TV) and UWTV (*u*-weighted TV), that

can achieve significant improvements for real imaging systems. With live-cell images, they improve the precision of local lifetime determination without significantly altering the global mean lifetime values (<5% lifetime changes). Finally, by combining optimal gating and TV denoising, even low-light excitation can achieve precision better than that obtained in high-light cases (RSD = 12.76% at total photon counts (TC) = 100 vs. RSD = 23.03% at TC = 400). Therefore, high-intensity excitation of living cells can be avoided. Notable five-fold improvements in precision (RSD from 49.90% to 11.94%) are easily observed in our extreme low-light example.

This study overcomes several challenges associated with making quantitative measurements of cellular responses, by enabling novel fluorescence lifetime map construction for better quantitation of molecular interactions and sub-cellular environmental changes in live cells.

Chapter 1 Introduction

1.1 Background and motivation

1.1.1 Quantitative understanding of living cells

The quantitative understanding of how living organisms behave has received high attention in the area of biological sciences and has clinical applications such as proposing potential molecular targets and doses for disease treatments. This will greatly help the development of biomedicine. For example, the determination of doses for disease treatments, in some cases, is limited to medical doctors' experience, precedent, and trial-and-error methods without a rigorous theoretical basis, and this often poses problems such as unexpected severe side-effects for a certain group of patients. Such problems may be avoided by a quantitative understanding of living human cells, which would provide a rigorous theoretical basis for disease treatments.

To be applied in potential clinical use, the quantitative understanding is utilized first by constructing quantitative models of biological systems. This can involve both tissue level models, for dosage determination and overall effects of drugs, and cellular level models, for a basis of understanding the kinetics of molecular interactions and proposing potential molecular targets for disease treatments.

An accurate and precise model can take into account individual patient sensitivity for dose and treatment predictions. A good model can resolve the dynamics of drugs in

patients, such as steady states, oscillations, and chaotic behaviors, and can predict when the changes of system dynamics will occur. This would be a key point in quantitative biomedicine because, when aiming at a target in bio-molecular signaling, the effects of changing its concentration and changing its interactions with other molecules might not be intuitive. As an example, enhancing the concentration of an inhibitor of an oncogene might later increase the effects of this oncogene after a certain time point, if the system is altered such that it is attracted to an unexpected (and unfavorable) steady state, such as death. Whether it happens or not to a certain group of patients is based on their sensitivities to some molecular interactions, hence their different kinetic parameters describing the molecular pathway. This is directly reflected by the effects and side-effects of medicine which differ on a case-by-case basis. Therefore, determination of concentration and kinetic parameters accurately and precisely is the first step in such quantitative analyses. Individual patient differences can be quantified by some key kinetic parameters and therefore these parameters can be used for pre-determination of proper target and doses for disease treatments [1-5].

One good example of mathematical models for potential clinical use is pharmacokinetics (PK) and pharmacodynamics (PD) models. Pharmacodynamics explores what a drug does to the body, whereas pharmacokinetics explores what the body does to the drug. They (especially PD) may be studied at many organizational levels – sub-molecular, molecular, cellular, tissue/organ and whole body – using *in vivo*, *ex vivo* and *in vitro* methods and utilizing a wide range of techniques [6]. There is current emphasis for extended integration of PK and PD into all phases of new drug development, including large-scale clinical trials [7]. In fact, PK and PD modeling and simulation are well-recognized powerful tools that enable effective implementation of the learn-and-confirm paradigm in drug development [8].

There are several model-building strategies in population PK-PD analyses [9]. Some model-based methodology can help analysis of drug efficacy and safety in diverse therapeutic areas, while some other kinds of modeling provide new tools for analysis of response vs. dose and response vs. time data [7]. An example is simultaneous PK-PD population analysis using an Iterative Two-Stage Bayesian (ITSB) algorithm. This method was evaluated using clinical data and Monte Carlo simulations [10]. Further examples include Identifying optimal biologic doses of everolimus (or RAD001, an orally active inhibitor of the mammalian target of rapamycin (mTOR) currently in clinical trials. mTOR is a multifunctional signal transduction kinase1 which has been implicated in cancer) in patients with cancer based on the modeling of preclinical and clinical PK-PD data [11], the use of concentration measurements of parent drug and metabolites during clinical-trials [12], and preclinical PK-PD models of gefitinib (an epidermal growth factor receptor (EGFR) inhibitor that is undergoing clinical evaluation in numerous cancer types and is conditionally approved for the treatment of non-small cell lung cancer) and the design of equivalent dosing regimens in EGFR wild-type and mutant tumor models [13].

Particularly at cellular level, the *in vivo* and *in silico* understanding of genomes and networks in cellular and multi-cellular systems is essential for drug discovery for multi-cellular diseases as well [14]. *In silico* methodologies, when integrated with *in vivo* engineering methods, lay the groundwork for understanding multi-cellular organisms and their genomes. The quest to construct a minimal cell can be followed by designed, minimal multi-cellular organisms. *In silico* multi-cellular systems biology will be essential in the design and construction of minimal genomes for minimal multi-cellular organisms. In addition, advanced methodologies combined with systems biology can further aid drug discovery. These novel approaches include multi-cellular PD and networked multi-cellular PD [14].

In this study, we focus on the cellular level to quantitatively resolve potential molecular target for disease treatments and potentially predictive kinetic parameters involved in molecular interactions. To construct a good quantitative model at the cellular level, it is, therefore, necessary to accurately and precisely determine the time-evolved molecular concentrations and the relevant kinetic parameters of molecular interactions by determining cellular and molecular responses to various environmental changes in living cells.

1.1.2 Fluorescence measurement and FLIM

The cellular and molecular responses in living cells can be determined by fluorescence measurements. There has been significant growth in the use of fluorescence in the biological sciences during the past two decades. Besides environmental monitoring, clinical chemistry, DNA sequencing, and genetic analysis by fluorescence in situ hybridization (FISH), fluorescence is used for cell identification and sorting in flow cytometry, and to reveal the localization and movement of intracellular substances in cellular imaging by means of fluorescence microscopy [15].

Steady-state or intensity-based fluorescence microscopy is routinely employed for studies in cell biology to reveal information regarding cellular morphology, intracellular ion concentrations, protein binding, lipid content, and membrane status [16]. However, it is sensitive to some intensity-based artifacts such as variation in excitation source intensity, detection gain setting, optical loss in the optical path or sample, variation in sample fluorophore (fluorescence molecule) concentration, photobleaching (damage of molecules due to light excitation), and microscope focusing. Further, fluorophores with similar excitation and emission spectra may be impossible to differentiate in steady-state intensity imaging.

Recently, fluorescence lifetime measurements have become very popular in biological applications [17, 18], and it has advantages over intensity-based measurements. Fluorescence lifetime, characterizing how fast the excited fluorescent molecules decay to the ground state, is an intrinsic property of fluorophores, depending only on the micro-environmental conditions such as temperature, pH, and interactions with other molecules. It is relatively insensitive to the factors affecting intensity, and therefore can serve as indicators for fluorophores' micro-environment [17].

As an example, photobleaching can be a huge issue in live-cell fluorescence measurement. Although photostable fluorophores, such as quantum dots, are becoming popular in fluorescence applications, organic molecules are still mostly used in live-cell applications. For example, GFP (Green Fluorescent Proteins) and its variants [19, 20] are very commonly used since they can be encoded with the proteins of interest to detect their levels of expression, localization, and interactions with other proteins as cells are responding to various environmental stimulations. However, fluorescent proteins can be vulnerable to photobleaching. Although researchers have been studying to create more photostable fluorescent proteins and appropriate correction procedures to compensate for photobleaching [21], using FLIM is another way to circumvent this problem, since photobleaching affects intensity-based measurement but in most cases does not affect lifetime-based measurement.

Combining lifetime measurement with microscopy, fluorescence lifetime imaging microscopy (FLIM) produces spatially resolved images of fluorescence lifetime, providing another dimension of quantitative information for visualizing fluorophore responses. FLIM can be used with various microscopy techniques for different applications, and greatly helps reveal sub-cellular environmental changes in live cells and provide better detection of localization of molecular interactions.

FLIM can be used with various microscopy techniques. Depending on the mechanism of illumination and detection, microscopes can be classified into wide-field, confocal, and multi-photon systems, on each of which lifetime imaging can be implemented. While wide-field microscopy illuminates the entire specimen to provide single-shot image acquisition and is rapid, confocal and multi-photon systems can provide better resolution and deeper optical sections, respectively.

In live-cell applications, FLIM can be used to detect fluorescence resonance energy transfer (FRET). FRET is a quantum mechanical process that has been used for detection of molecular interactions in live cells. FRET can be regarded as a nano-scale *in vivo* ruler to measure the distance between two or multiple fluorophores. In commonly used two-component FRET system, non-radiative energy transfer occurs from donor to acceptor if they are in close proximity, and the fluorescence lifetime of the donor decreases.

As mentioned in the previous section, at cellular level, the *in vivo* and *in silico* understanding of genomes and networks in cellular and multi-cellular systems is essential for drug discovery for multi-cellular diseases. Apparently, this understanding can be facilitated by using FLIM or FLIM-based FRET with living cells since these techniques help us construct genetic and biochemical reaction networks by indicating the kinetics and dynamics of molecular interactions and cellular responses and help us understand these models quantitatively [1, 22-24].

As for pharmacokinetics (PK) and pharmacodynamics (PD) models for potential clinical use, indeed FLIM and FRET have been demonstrated to assist the understanding of PK and PD. For example, they can help outline the main trafficking pathways of relevance to intracellular drug delivery and cellular uptake, to characterize intracellular trafficking and targeting, by providing time-lapse imaging and associated

computational analyses [25]. In another example, advanced microscopy technique such as FLIM was used to uncover the complexity of drug targeting in single cells and monitor the kinetics and dynamics of drug–DNA targeting in living cells [26]. FRET can be used with wavelet and fast Fourier transforms to study the dynamics of spatiotemporal properties of complex pharmacological systems [27]. Another example demonstrated that a genetically encoded fusion of native protein kinase C (PKC) delta with flanking CFP and YFP peptides could be used to analyze the *in vivo* pharmacokinetics and pharmacodynamics of twelve well-characterized PKC ligands [28].

1.1.3 Challenges in live-cell FLIM

To resolve fluorescence lifetime, high-intensity light sources, such as lasers, are needed for fluorescence excitation. Therefore, one major challenge in live-cell FLIM applications is caused by the effects of high-intensity sources on live-cell samples:

- Cell damage may occur with high-intensity light sources.
    a. It was reported that cell vitality and cellular reproduction could be affected with laser excitation, and destructive effects were more pronounced for shorter laser pulses [29].
    b. Laser could induce cell lysis in time-resolved imaging [30].

  Therefore, maintaining biological viability and minimizing the perturbation in living-cell systems have been an important issue in lifetime measurement with relatively high-intensity source excitation.

Other challenges can also be encountered in live-cell FLIM:

- The spatial and temporal features in cellular responses of interest may not be resolved in FLIM results if laser scanning is required, because:

a. During fluorescence measurement, cell movement may occur.

b. The molecular interactions of interest may have very fast kinetics in live cells [1].

- In live-cell fluorescence measurement, the detected photon counts (or the intensity signals) could be low, and this can be attributed to low signals from fluorophores in live cells. Fluorophores used in live-cell systems can be either endogenous or exogenous:

    a. When endogenous fluorophores are used [31], low photon counts may be directly due to:

        i. Low concentration of the molecules of interest in live cells

        ii. Unfavorable optical properties of the molecules of interest in live cells (such as the excitation / emission wavelengths, extinction coefficient, quantum yield, and photo-sensitivity)

    b. Exogenous fluorophores are introduced into cells by means of transferring genes (in the case of fluorescent proteins), or transporting fluorescent molecules / particles through cell membrane. In this case, low photon counts may be due to:

        i. Reasons mentioned above for the endogenous fluorophores

        ii. Low transfer / transcription / translation efficiency of genes

        iii. Low transporting efficiency of fluorescent molecules / particles

    Although FLIM is usually insensitive to intensity issues, low photon counts may still cause imprecision in lifetime determination.

As mentioned previously, FLIM can be used with various microscopy techniques. While confocal or multi-photon microscopy can be combined with FLIM for better light penetration ability and higher resolution, higher focused light energy and longer dwell time for excitation may make the first two challenges mentioned above huge issues. These problems could be even worse since shorter laser pulses such as those of femto-second lasers are usually needed in these applications.

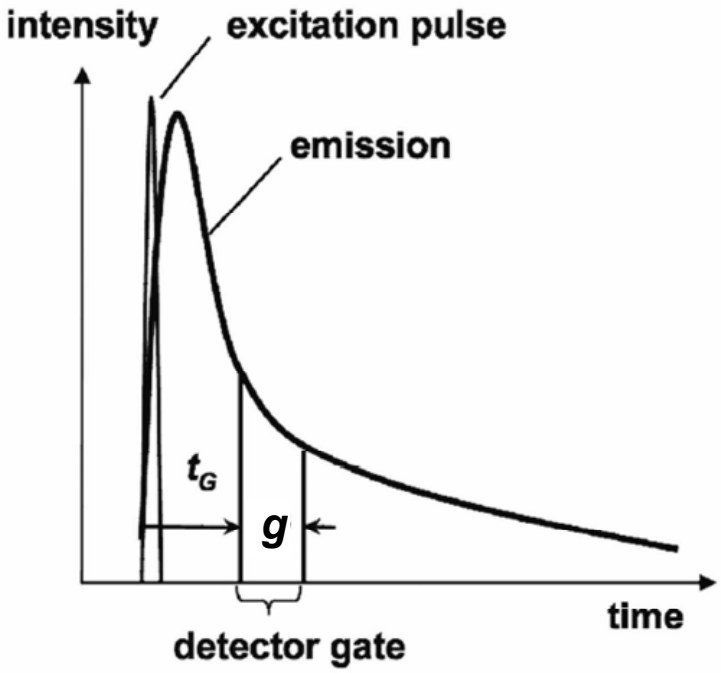

Figure 1-1 Time-gated FLIM concept. The system captures fluorescence intensity image at a time t_G after the excitation pulse over the interval *g*. Lifetime can be created using intensity images captured at several different t_G. [32]

On the other hand, wide-field time-gated FLIM (Figure 1-1) can be used for high-speed imaging with fluorescent lifetime as image contrast. It provides high-speed snap shots of lifetime distributions because no laser scanning is required. In addition, it has advantages such as reducing light delivery into live cells. Therefore, the use of wide-field time-gated FLIM can reduce or remove the first two problems mentioned above.

Still, one challenge remains with current live-cell time-gated FLIM applications: low detected photon counts, resulting from maintaining biological viability or low fluorophore concentrations in live cells.

To demonstrate that low photon counts greatly deteriorate the precision of FLIM applications, we take an example of one of the various FLIM applications: The detection of FRET. Assuming in commonly used two-component FRET system there are donor-accepter complex (DA), free donor (D), and free accepter (A), with the donor fluorescence decaying single-exponentially, total photon counts = 10^2, and [DA] = ~90%([DA]+[D]), if, for example, lifetime changes from 3 ns to 0.6 ns due to FRET and two-component (DA and D) rapid lifetime determination (RLD) is used for lifetime determination, this will cause more than 35% error in FRET efficiency determination.

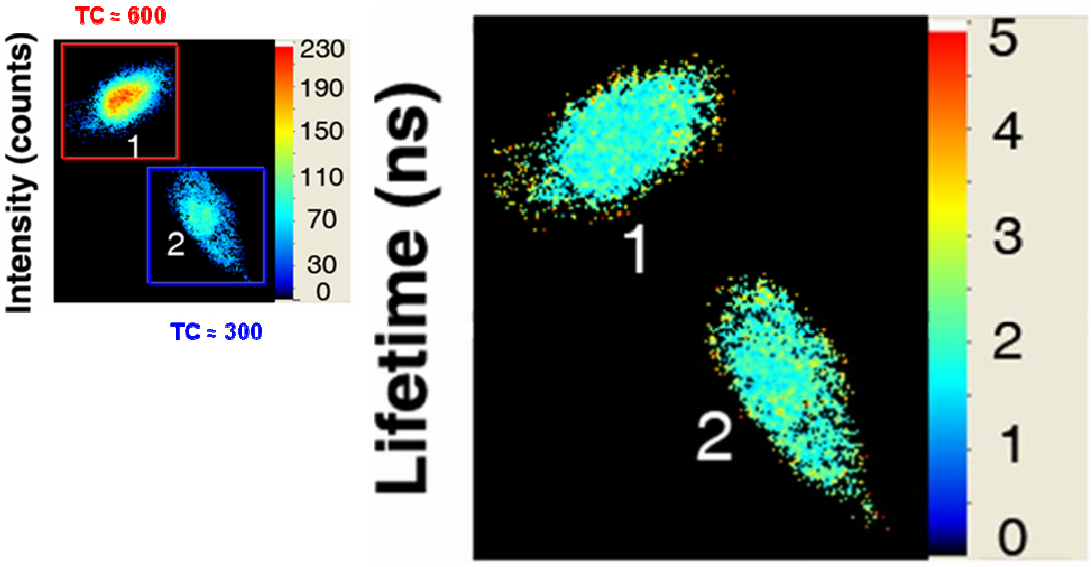

Figure 1-2 Two live cells transfected with ECFP (enhanced cyan fluorescent protein) and emitting different total photon counts due to their different ECFP concentrations. The intensity image is shown on the left with the total photon counts (TC) labeled on each cell. The corresponding lifetime map is shown on the right. The variations of the lifetime values can be clearly seen, especially for the cell with lower TC (the cell in the bottom-right region). [33]

Figure 1-2 shows an example of how low total photon counts can make the resulting lifetime maps noisy and the lifetime values uncertain. In this figure, two live cells are

shown in the intensity image and the corresponding lifetime map. These two cells were transfected with ECFP (enhanced cyan fluorescent protein), and during detection, they emitted different total photon counts due to their different ECFP concentrations. The variations of the lifetime values can be clearly seen in the lifetime map, especially for the cell with lower total photon counts, and the precision in lifetime determination of both cells needs to be improved.

In addition, it has been reported that there are several issues regarding accuracy associated with FRET experiments, including random/unexpected association of FRET pairs (non-specific FRET), spectral cross-talk and bleed-through, mixture of interacting and non-interacting FRET components, lack of FRET standards, use of various FRET indices, and possible disturbances in the fluorophores' environment such as pH and temperature [19, 21, 34-37].

Because of the challenges mentioned above, the use of fluorescence indicators and FRET in many live-cell studies in order to reveal changes in molecular interactions and sub-cellular environments are prone to errors. This hinders understanding of quantitative live-cell studies and prevents these researches from correctly proposing the potential targets and doses for disease treatments needed in clinical use.

Some methods may be used to enhance the precision:

- Development of better probes / techniques for transferring the probes
    a. This can provide us:
        i. Stronger fluorescent signals
        ii. Higher transfer efficiency
        iii. Less perturbation to cells

However, the development takes time and effort. While we are still waiting for researchers to develop better probes and techniques, we may consider the following in our experiments:

- Load more fluorophores into cells
    a. This may cause adverse effects on cell function. As an example, in our experiments, loading more genes in living cells requires adding more transfection reagents to living cells. Since some transfection reagents contain a majority of alcohol (for example, 80% for the GeneJammer transfection reagent from Stratagene), high amounts of transfection reagents may jeopardize cell viability.
- Increase the intensity of the excitation light or average over several pulses for each gate
    a. These two methods may be valid only for photostable samples, and will increase the probability of photobleaching of most of the fluorophores commonly used in *in vivo* molecular imaging such as fluorescent proteins [38], and may also cause unexpected cell response / cell ablation, and disturb the live-cell system [29, 30, 39-41].
- Average over all pixels in single cells for statistical analysis
    a. In this case, sub-cellular features in lifetime maps may be ignored.

As for the problems associated with FRET, among commonly used FRET detection methods, FLIM has been shown to be the best method in a controlled experiment with reference constructs [42]. Indeed, using lifetime techniques, some problems affecting accuracy will be removed, while others can be further solved or negligible in well-controlled, comparative, FRET-FLIM experiments.

In this work, therefore, we improve accuracy and precision in FLIM applications by using various approaches, including the choice of a better fluorophore, the incorporation of environmental controls, the search of optimal gating schemes and better lifetime determination methods (a temporal approach), and the utilization of Total Variation denoising models (a spatial approach). Since the temporal and spatial approaches apply to different dimensions, we also assume that they can work together and then we test this assumption in this study as well.

1.2 Hypotheses and specific aims

In this study, we optimize the time-gated FLIM in several ways to overcome the challenges mentioned above and enable lifetime map construction for better quantification of molecular interactions and sub-cellular environmental changes in live cells. We hypothesize that the proposed methods can remove intensity-based artifacts and provide better detection of the localization of molecular interactions.

Specific Aim 1: To improve the accuracy of FRET detection in live cells by using gated-FLIM with well-controlled experiments. We wish to determine if lifetime-based approach is more powerful in FRET detection in a live-cell system and also to specify appropriate controls required in this application of FRET in order to prevent systematic errors affecting the accuracy. These controls include temperature control, CO_2 control, proper positive and negative controls for FRET-FLIM detection, and also duplicate group confirmation. Optically improved fluorescent molecules are also included for better results. These factors are considered and compared at the same time in FRET-FLIM for the first time. The experiments are conducted in a system involving interactions of an oncogene protein with its inhibitor.

Since FLIM is a technique involving both temporal and spatial data utilization and construction, we hypothesize that the precision of lifetime determination in FLIM can therefore be enhanced with respect to either temporal data acquisition and processing (with optimal gating and curve fitting), or spatial data processing (with image denoising), or a novel combination of both of them.

Specific Aim 2: To improve the precision of gated-FLIM results by finding the optimal gating schemes (a temporally-related approach) and curve fitting methods. Gate width, time interval between consecutive gates, and number of gates are included as controllable system parameters and are optimized to achieve the best precision in this study. This approach is performed, for the first time, for a thorough analysis for double-exponential decay. Monte Carlo simulations will be used to construct distributions of lifetimes calculated from noise-corrupted integrated intensities. Precision and accuracy can then be determined. This will be applied to all fitting methods considered in this study, providing a guideline to choosing the best way for lifetime determination.

Specific Aim 3: To improve the precision of gated-FLIM results by applying total-variation (TV) denoising algorithms (a spatially-related approach) on the resulting images. TV denoising algorithms are used to eliminate noise and make the resulting image closer to the original image without corruption of noise [43-45]. In this study, several TV denoising algorithms will be applied first to artificial images, mimicking time-gated FLIM results, for which lifetimes and pre-exponential terms are known and to which random noise is added. By constructing distributions of determined lifetime values after denoising with Monte Carlo simulations, precision and accuracy of lifetime determination can be evaluated with each denoising algorithm. After the evaluations, TV algorithms will, for the first time, be applied to images acquired with the FLIM system, and further modifications may need to be made for this real imaging system.

Specific Aim 4: To improve the precision of gated-FLIM results by applying a combination of the temporal and spatial approaches. Since the temporal and spatial methods apply to different dimensions and different stages of the time-gated FLIM, we assume that they can work together to confer even better precision than any one of the two methods applied alone. Therefore, we combine these two methods, and observe how the precision can be further improved. When these two methods are applied to low-light imaging, we also explore how the precision is, compared to that in a higher-light case. In addition, to use the novel combination of the two methods more efficiently, we also explore the linearity of these two methods, including how linearly these two operations are, how independently they can work together, and how additive their precision improvements are.

The proposed studies will provide useful information to minimize errors and sample perturbation in lifetime determination with wide-field time-gated FLIM systems. In addition, the results and analysis provided can also be modified and serve as a basis to improve fitting of curves with any kinds of noise and deviations. They can also be applied to processing of images from other kind of acquisition methods and medical imaging devices providing that the forms of present noise are known or can be evaluated.

1.3 Dissertation overview

The organization of this dissertation is as follows.

Chapter 2, the next chapter, provides a thorough description of FLIM, including the concepts of fluorescence lifetime and the instrumentation / data processing of our time-gated FLIM system. It also provides the detailed analytical procedures used in the temporal and spatial approaches.

Chapter 3 describes the FLIM application to FRET detection and the improvement of its accuracy and consistency by using a better fluorophore and environment controls in a system involving interactions of an oncogene protein with its inhibitor.

Chapter 4 details the temporal approach, including introductions to various lifetime determination methods, Monte Carlo simulations for precision evaluation, optimal gating determination, analyses on gating parameters, and experimental validations.

Chapter 5 covers the spatial approach. The accuracy and precision of lifetime determination after various total variation (TV) image denoising will first be evaluated with artificial images. Improvements of some TV models will then be provided and followed by live-cell image denoising results.

Chapter 6 focuses on the combination of the two methods, including how the precision can be further enhanced by the combination, how the improved precision of a low-light case is compared to that in a higher-light case, and the discussions of the linearity of these two methods.

Chapter 7 concludes this dissertation, describes future work for further improvements, and provides potential applications.

Chapter 2 FLIM instrumentation and analytical procedures

This chapter provides the theory, instrumentation, and data processing of our time-gated FLIM system. Also, this chapter presents the detailed analytical procedures used in the temporal and spatial approaches that lead to the results demonstrated in later chapters (Chapter 4 and Chapter 5).

2.1 Fluorescence lifetime

2.1.1 Basic theory

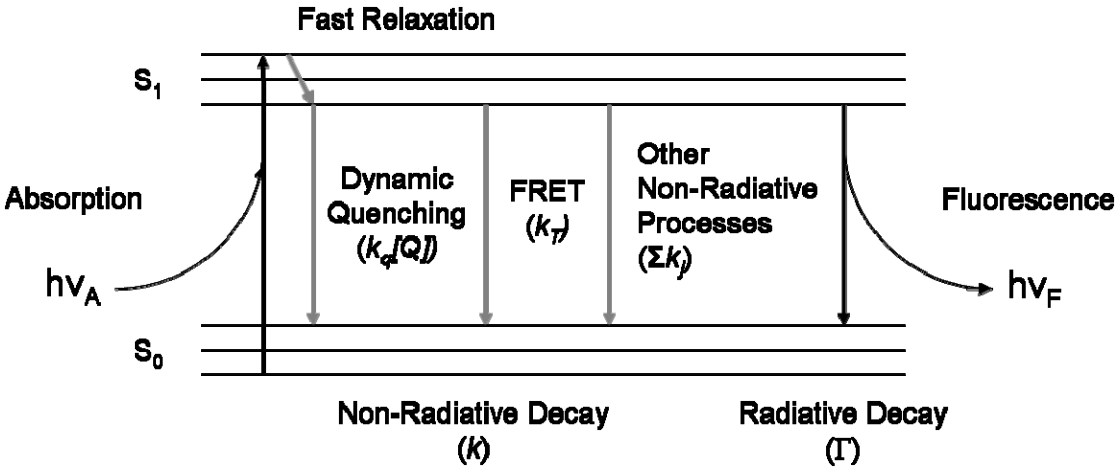

Figure 2-1 Simplified Jablonski diagram. k_q: Bimolecular quenching constant; *[Q]*: Quencher concentration (see Section 2.1.2); k_T: Energy transfer rate constant (see Section 3.1); k_i: Rate constant for non-radiative processes other than dynamic quenching and FRET. [17]

Figure 2-1 is a simplified version of a Jablonski diagram to illustrate the fluorescence process, where S_0 and S_1 are the ground and the first-excited electronic states,

respectively, and the horizontal lines represent different vibrational states of the fluorophore. In condensed phases, after light absorption, almost all molecules rapidly relax to the lowest vibrational state of the first-excited state, from which molecules return to the ground state via one of two decay processes: non-radiative (k) or radiative (Γ) decay. The radiative decay rate Γ depends on the electronic properties of an isolated fluorophore. Molecular interactions, such as dynamic (or collisional) quenching and energy transfer, are treated in the non-radiative decay rate k. Radiative decay is responsible for fluorescence emission, providing detectable photons. However, since both decays depopulate fluorescent molecules in the first excited state, with population $N(t)$, the decay of fluorescence emission intensity, proportional to $N(t)$, is attributed to both decay rates, and, in the most simple case, follows the stochastic hence exponential decay as shown in Equations (2-1) and (2-2).

$$\frac{dN(t)}{dt} = -(\Gamma + k)N(t) \tag{2-1}$$

$$N(t) = N_o e^{-(\Gamma+k)t} = N_o e^{-t/\tau} \tag{2-2}$$

where N_o is the initial number of fluorescent molecules in the first excited state, and

$$\tau = \frac{1}{\Gamma + k} \tag{2-3}$$

is the fluorescence lifetime, reflecting the average time a molecule spends in the excited state prior to return to the ground state. As is evident, both non-radiative and radiative decays play a role in the value of lifetime, and hence in the fluorescence emission process. Another important property of fluorophores is quantum yield, defined as the

ratio of the number of emitted photons to the number of absorbed photons, which is given by

$$Q = \frac{\Gamma}{\Gamma + k} \tag{2-4}$$

Note that $0 \le Q \le 1$ and Q can be close to unity if $k << \Gamma$. Generally, higher quantum yield means brighter fluorescent signals, which is usually favored in fluorescence applications. Although Q can be used as a source of contrast, experimental protocols for estimating Q are strict and controlled, making it difficult to apply in biological samples.

2.1.2 Key features of lifetime sensing

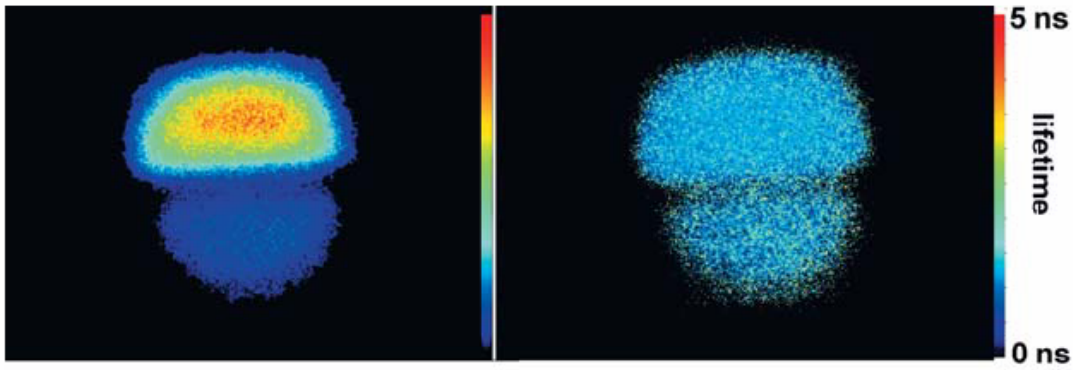

Figure 2-2 Intensity-independent fluorophore lifetimes recovered by FLIM. Despite a factor of four difference in POPOP concentration and hence signal intensity (left), the 3-gate protocol lifetime map (right) showed identical mean lifetimes for the two POPOP samples. The images were of POPOP in ethanol solutions in two quartz capillaries. The capillary interface was on the diameter, with the circular region as the illumination area. The intensity images were background subtracted before calculation of lifetime map. [46]

Fluorescence lifetime is an intrinsic property of fluorophores and is insensitive to intensity artifacts, such as variation in excitation source intensity, detection gain setting, optical loss in the optical path or sample, variation in sample fluorophore concentration, photobleaching, and microscope focusing. Figure 2-2 is an illustration of intensity-independence of lifetime imaging. Despite the fact that fluorescence intensity revealed

the fluorophore concentration difference between samples, no significant lifetime differences were observed, reflecting the insensitivity of lifetime to intensity artifacts. On the other hand, due to the nature of the non-radiative decay process, lifetimes are sensitive to the fluorophore's micro-environment, including factors such as temperature, pH, oxygen concentration, polarity, molecular associations (binding), ion concentration, and relaxation through collisional (dynamic) quenching and fluorescence resonant energy transfer (FRET).

Lifetime measurement, therefore, provides a means of probing the local fluorophore environment. FLIM was reported [47] for quantitative pH determination in living cells with the fluorescent probe c.SNAFL-1. It was found that a lifetime-based approach was easier to employ than traditional ratiometric techniques, while still providing accurate information regarding intracellular pH. Another FLIM-based pH measurement was presented in [48], which suggested that FLIM can measure the intracellular pH of resting cells and follow the pH fluctuations inside the cells after environmental perturbations. Measurement of dissolved oxygen concentration in single living cells was demonstrated by [49] and [50]. Because the probe's fluorescence emission was found to be dynamically quenched by oxygen, the probe's lifetime was directly dependent upon local oxygen concentration and could be used for quantitative imaging in cells via FLIM. Molecular associations such as binding of the endogenous fluorophore nicotinamide adenine dinucleotide (NADH) to malate dehydrogenase have been imaged with FLIM [51], by using the increase in NADH lifetime upon binding as a source of contrast. NADH lifetime increased by ~150% and was much easier to detect than the blueshift of the emission spectrum that was only ~20% of the full-width at half-maximum (FWHM) in fluorescence intensity measurement. Finally, FRET between the phospholipids NBD-PE (energy donor) and LRB-PE (energy acceptor) was employed to monitor endosomal

fusion in single living cells [52]. FRET involves non-radiative energy transfer between fluorophores, and will be discussed in detail in Chapter 3. Excellent reviews providing further historical FLIM background can be found in [53-56].

2.2 Time-gated fluorescence lifetime imaging microscopy

2.2.1 Concepts

As mentioned above, the objective of fluorescence lifetime measurement is to recover the lifetime parameter that describes fluorescence decay, which provides additional information that is lost during steady-state intensity measurement.

FLIM measures fluorescence lifetime and provides lifetime maps using various microscopy techniques. Depending on the mechanism of illumination and detection, microscopes can be classified into wide-field, confocal, and multi-photon systems, on each of which lifetime imaging can be implemented. While wide-field microscopy illuminates the entire specimen to provide single-shot image acquisition and is rapid, confocal and multi-photon systems can provide better resolution and deeper optical sections, respectively.

Among a variety of FLIM techniques, Time-Domain (TD) FLIM is more intuitive, is optimal for flexible, large temporal range systems, and is especially apt for long-lifetime measurements. It exploits the fact that the fluorescence emission is theoretically proportional to the number of molecules in the first excited state, and hence it decays exponentially, as described in Section 2.1.1. The exponential decay can be reconstructed in different ways, most commonly used of which are time-gated FLIM and Time-Correlated Single Photon Counting (TCSPC). Frequency-Domain (FD) FLIM, on the other hand, is better suited for evaluating multi-exponential decays.

Time-gated FLIM (Figure 1-1), as a Time-Domain (TD) FLIM technique, is commonly used in high-speed imaging with fluorescent lifetime as image contrast. This can be achieved with a gating device such as a gated charge-coupled device (CCD) for recording gated, integrated fluorescence signals [32, 57-59]. If fast lifetime calculation is needed, an approach called rapid lifetime determination (RLD) can be used, in which closed-form solutions of lifetime and pre-exponential terms are used.

2.2.2 Instrumentation

To implement time-gated FLIM, we have recently designed and characterized a novel wide-field, time-domain FLIM system developed for picosecond time-resolved biological imaging [30]. A nitrogen laser pumping a dye laser for UV-visible-NIR excitation offers a significantly less expensive, wide-field, and importantly for clinical applications, potentially portable alternative to multi-photon excitation for sub-nanosecond FLIM imaging of biological samples [30]. The large temporal dynamic range (750 ps – 1 μs), the 50 ps lifetime discrimination, and the spatial resolution of 1.4 μm of the system make it suitable for studying many endogenous and exogenous fluorophores that may transit through cells [20, 22, 32].

Figure 2-3 illustrates the instrumentation of our FLIM system, with some key experimental specifications for imaging living cells described below. The excitation source consisted of a pulsed nitrogen laser (GL-3300, Photon Technology International, Lawrenceville, NJ) pumping a dye laser (GL-301, Photon Technology International, Lawrenceville, NJ), with a wavelength range from UV through near infrared (NIR), depending on the dye used. The excitation light was delivered via an optical fiber (SFS600/660N, Fiberguide Industries, Stirling, NJ) to a research-grade, inverted microscope (Axiovert S100 2TV, Zeiss, Germany) in epi-illumination mode. The optical

fiber had the added benefit of homogenizing the spatial intensity distribution of the beam. A reference pulse split from the excitation light via a beam splitter was sent to an optical discriminator to generate an electronic pulse, providing a time reference to a picosecond delay generator (DEL350, Becker & Hickl, Germany). The delay generator output was used to trigger the gated intensified CCD (ICCD) camera (Picostar HR, LaVision, Germany). The ICCD had variable intensifier gain and gate width settings varying from 200 ps to 10 ms and can be used to implement high-speed imaging in other applications as well [60].

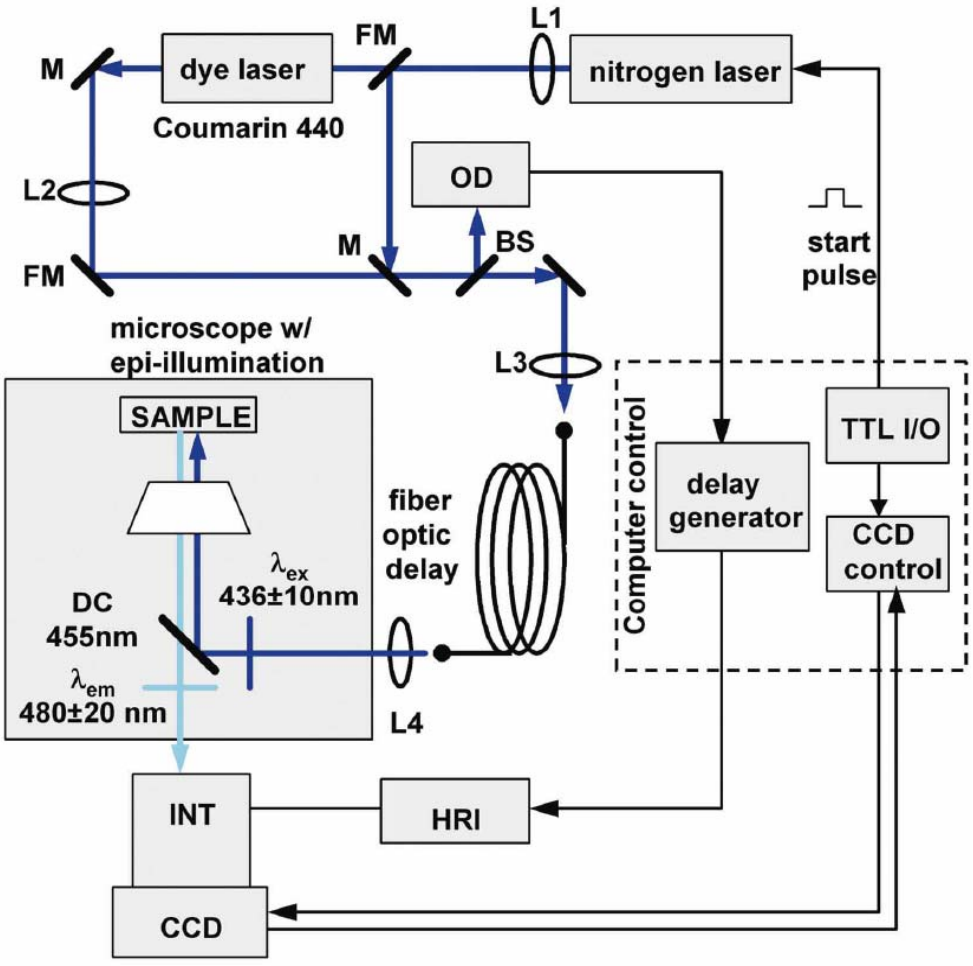

Figure 2-3 The time-gated FLIM setup used for this study. Abbreviations: CCD = charge-coupled device; HRI = high rate imager; INT = intensifier; TTL I/O = TTL input/output card; OD = optical discriminator; BS = beam splitter; DC = dichroic mirror; FM = “flippable” mirror; L1, L2, L3, L4 = quartz lenses; M = mirror. Thick solid lines = light path; thin solid line = electronic path. [32]

2.2.3 Data processing

As a first approach to creating fluorescence lifetime maps rapidly with acceptable precision, four-gate protocol with an analytic least squares lifetime determination algorithm are used on a pixel-by-pixel basis [61-63]:

$$\tau_p = -\frac{N(\sum t_i^2) - (\sum t_i)^2}{N\sum t_i \ln I_{i,p} - (\sum t_i)(\sum \ln I_{i,p})} \tag{2-5}$$

where τ_p is the lifetime of pixel p, $I_{i,p}$ is the intensity of pixel p in image i, t_i is the gate delay of image i, and N is the number of images. All sums are over i.

Other sophisticated lifetime determination methods will be further discussed in Section 2.3 and Chapter 4 because they are a part of the temporal approach for FLIM optimization.

Additional steps in data processing are needed for more accurate lifetime map production. Before lifetime calculation, the step “background subtraction” takes average of the intensities of pixels within a specified background region and subtracts that average value from all pixels. Also, the step “reject” sets intensities to zero for all pixels with intensities below a certain value (assigned as the parameter “reject”) after background subtraction. After lifetime calculation, the step “tau range” sets lifetime to zero for all pixels with lifetime above a certain value (assigned as the parameter “taurange”) after lifetime calculation, to remove lifetime values in physically meaningless regions.

2.2.4 System variations

The main variations of our FLIM system, their relative magnitudes, how they may affect the accuracy and precision of lifetime determination are considered here in this section.

First, let us consider the kinds of noise introduced by the CCD camera to the images. They affect the precision of lifetime determination with respect to different pixel locations and include shot noise, readout noise, thermal noise, and flicker noise.

Shot noise (or quantum noise) is usually the main noise in terms of magnitude especially for low-light imaging, since it follows Poisson distribution. For example, if gain = 5 (1 photon count received = 5 counts in the images) for the highest gain setting in our system, 100 counts will arise from 20 photons (quantum yield taken into account). This in turn means that there is a standard deviation of the signals, or the magnitude of noise, as $20^{1/2}$ = 4.47 photons or 22.36 counts. Therefore, in this case, the relative standard deviation (RSD) is 22.36%. In fact, as will be further described in Section 5.3.1, where a series of noise analyses will be conducted, the effective gain value for noise estimation with the highest gain setting in our system is about only 1.0 (Figure 5-2). In this case, for 100 counts, the standard deviation of the signals is $100^{1/2}$ = 10 counts and the RSD is 10%. Shot noise is intrinsic to the photon statistics of the image and cannot be reduced [64].

Readout noise is independent of temperature and is normally constant at a given readout rate [65]. It increases approximately as the square root of the readout rate [64]. In our system, the readout rate has a fixed value of 12.5 MHz, which produces readout noise with a constant variation level of ~2 counts. This is the main background noise in our system. It is lower than the shot noise of 10 counts mentioned above when the mean

signal is 100 counts. However, it becomes more and more significant with decreasing mean intensity. In addition, since it is not dependent on the mean intensity and has fixed variation level everywhere in the images, this causes some problems when the readout noise has to be taken into account along with the shot noise, which is dependent on the mean intensity value. This issue will be further discussed in Section 5.3.1, where the readout noise is incorporated into our algorithms and the magnitude of ~2 counts is confirmed by our experiments and models (Figure 5-3).

The other two kinds of noise are thermal noise and flicker noise. Thermal noise (or dark-current noise) is the fluctuation of the dark current generated in the CCD. The total dark current is a function of the integration time and the rate as which dark current is generated [65]. It can be reduced by cooling the camera [64]. The thermal noise in our system is specified as < 0.1 electron/pixel/second when the CCD is cooled to -15 ^{o}C. Flicker noise has a magnitude proportional to 1/frequency. It occurs in almost all electronic devices, and results from a variety of effects, such as impurities in a conductive channel, generation and recombination noise in a transistor due to base current. Both thermal noise and flicker noise can be neglected in our experiments, since our CCD is operated with exposure time of < 1 millisecond with a readout rate of 12.5 MHz.

Let us then consider the variations outside the CCD camera. They include variations from the intensifier, the laser, and the time jitter of gating.

The variations from the intensifier in an ICCD camera has been studied by researchers as a part of the ICCD cascade noise. A full and detailed description of ICCD cascade noise can be found in literature [66]. This cascade noise consists of five components arising from the five stages of photon-electron conversions in ICCDs:

1. Photon incident on the photocathode (causing Poisson-distributed noise)

2. Quantum efficiency of the photocathode
3. Fraction of photoelectron entering micro-channel plate (MCP)
4. Intensifier gain including MCP and phosphor
5. Coefficient of conversion of photons back to electrons (CCD) and CCD amplification

The second and the third components are negligible compared to the first one, while the fourth and the fifth components are negligible if intensifier gains are large. Since we always use the highest setting for the intensifier gain, only the first component needs to be considered, and it is merely the CCD quantum noise, which has been described above.

The variations of the cross-sectional intensity in the laser beam can play a role. These are variations inside the spatial pattern for each laser pulse. Since these variations appear to increase in proportion to the laser intensity, the resulting variation magnitude should have a fixed RSD. As we can see later in Section 5.3.1 (Figure 5-3), this is very likely the source of the extra noise included in our analysis with a magnitude of 1.2% RSD. These variations become more significant when other forms of noise are averaged out and when the intensity increases. Spatial homogeneity of the cross-sectional laser pulse intensity is improved, as mentioned previously, by the scrambling effect of the optical fiber in our system (the technical details can be found elsewhere [46]).

Finally, we also have laser pulse-to-pulse intensity variation and the time jitter of gating. The laser pulse-to-pulse intensity variation has about 2% RSD and the time jitter of gating is about 10 ps. If only one image is taken in each gating, these two kinds of variation will affect the accuracy, but not precision, of lifetime maps, and their effects can

be removed by taking several images and averaging them in each gating. Even if averaging is not performed, our later analyses regarding precision will still not be affected.

2.3 The temporal approach

2.3.1 Introduction to optimal gating and curve fitting

As an approach to improve precision, the temporal approach covers optimal selections of gating parameters and an analysis of various curve fitting / lifetime determination methods. With different gating parameters such as gate width (*g*) and time interval between two consecutive gates (*dt*), the signal-to-noise ratio (SNR) associated with each gate in time-gated FLIM can be different. These different SNR values affect the precision of lifetime determination. Given an lifetime determination method, optimal gating scheme therefore can be determined in terms of the precision of lifetime determination. In addition, different fitting methods also affect this precision.

Some researchers have studied the optimal gating and curve fitting in FLIM in the past two decades. For example, optimal gating schemes with rapid lifetime determination (RLD) for single-exponential decays with respect to relative standard deviation (RSD) of lifetime have been reported [67, 68], and an error analysis of RLD for double-exponential decay has also been addressed [63]. When longer time is available for lifetime determination, or, when higher precision is desired, especially when the available total count is low, Weighted Nonlinear Least-Squares (WNLLS) is usually a preferred method. However, Maximum Likelihood Estimation (MLE) is another approach that has been proved to be advantageous for single-exponential lifetime determination, especially for ultra-dilute dye solutions [69-73], and currently the use of MLE in TSCPC

data with multi-exponential decay has also been analyzed [74]. Recently, optimization of fluorescence lifetime sensing in frequency-domain has also been studied [75].

However, most of the previous studies did not explicitly point out what the optimal gating schemes were in the RSD analysis and most of them only covered single-exponential decay analysis. Therefore, in this dissertation, we study the performance of all the lifetime determination methods mentioned above and deal with double-exponential decay. In our analysis, we first compare the precision of these approaches, and then search the parameter space in order to find the optimal gating conditions for all combinations of the variables of interest (the lifetimes and the pre-exponential terms) within practically useful given ranges, in terms of minimal achievable RSD. Also in this section, we develop a generalized closed-form solution to lifetimes and pre-exponential terms in double-exponential RLD to address the issue of optimal gating scheme for RLD. The temporal approach for the analysis of single-exponential decay is also studied but is not described in this dissertation since it is relatively simple.

The results presented later in Chapter 4 will provide useful information to minimize errors and sample perturbation in lifetime determination with wide-field FLIM system. If high-speed imaging is desired, our results also provide optimal scheme for RLD, which can be used with both gated devices and TCSPC (Time-Correlated Single Photon Counting) techniques. Furthermore, in this report, we will discuss the errors associated with entire-curve fitting in the context of all combinations of lifetimes and pre-exponential terms for different approaches, providing a guideline to choosing the best way for lifetime determination.

2.3.2 Optimal gating and parameters used in time-gated integration

The single-exponential decay of fluorescence can be represented as

$$I(t) = \alpha \exp(-t/\tau)$$

(2-6)

where $I(t)$ is the intensity of fluorescence that can be observed following excitation, τ is the fluorescence lifetime and α is the pre-exponential term representing the initial intensity. Single-exponential decay of fluorescence is a result of random decay process where the number of decaying fluorescent molecules is proportional to the number of fluorescent molecules in the excited state [17]. The double-exponential decay has the following form,

$$I(t) = \alpha_1 \exp(-t/\tau_1) + \alpha_2 \exp(-t/\tau_2)$$

(2-7)

which is a linear combination of two single-exponential decays.

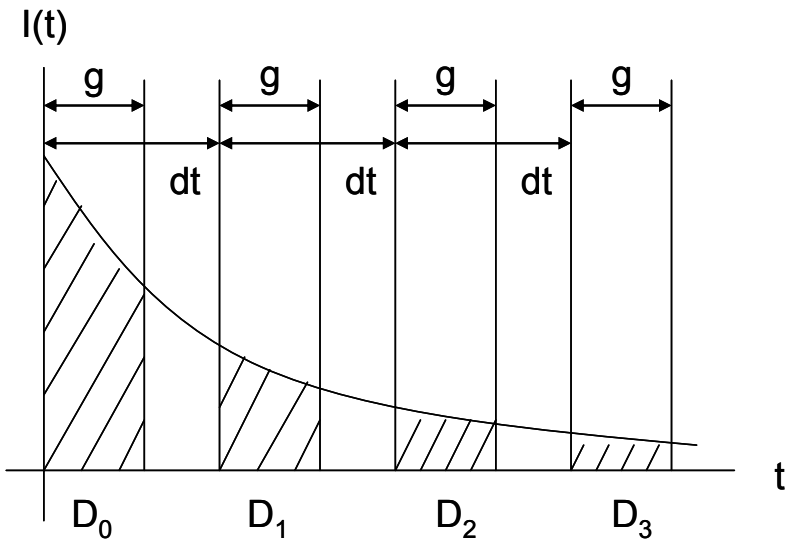

Figure 2-4 A schematic demonstration of the controllable system parameters. *g* is the gate width of each gate and *dt* is the time between starting time points of any two consecutive gates. D_0, D_1, D_2 and D_3 are the integrals of the 1st, 2nd, 3rd, and 4th gates, respectively.

The parameters in our gating scheme are shown in Figure 2-4. *g* is the gate width of each gate, *dt* is the time between starting time points of any two consecutive gates, and *n* will be the total number of gates, which is four in the example of Figure 2-4. For RLD, *n*

is fixed at 4, as will be described below. We assume the starting point of the first gate is the peak intensity following a short pulse, approximated as a delta function, without any delay from the peak, so that the pre-exponential terms can be estimated correctly. Any off-peak deviation can be corrected later with ease. In this work we explored the gating schemes where *g* and *dt* are fixed. For single-exponential decays schemes where different *g* and *dt* are adopted have been analyzed [70, 76, 77]. With varying *g* and *dt* for each gate, indeed relative standard deviation (RSD, defined below) can be further minimized, but this further complicates the problem by adding at least five more independent variables and in RLD this also involves solving a problem with no closed-form solutions.

To analyze the precision of the lifetime determination methods, RSD is defined as standard deviation of the parameter of interest (calculated via Monte Carlo simulations, which will be described below) divided by the mean of that parameter. Here, the "parameters of interest" are mainly the sample parameters α_1, α_2, τ_1, and τ_2, but the fraction of α_1 and α_2 are used: $f_1 = \alpha_1 / (\alpha_1 + \alpha_2)$, $f_2 = \alpha_2 / (\alpha_1 + \alpha_2)$ [63]. We realize that in WNLLS and MLE methods, RSD is a function of some parameters, namely RSD = f (α_1/α_2, τ_2/τ_1; g/τ_1, g/dt, n). Here we list the sample parameters α_1/α_2 and τ_2/τ_1 as independent variables while g/τ_1, g/dt and n as parameters, because apparently in real experiments α_1/α_2 and τ_2/τ_1 are variables that we are interested in but cannot be controlled manually. In order to determine the value of α_1/α_2 and τ_2/τ_1 precisely, "system parameters" in the gating scheme g/τ_1, g/dt, n are adjusted. Later in Chapter 4, our goal is to find the optimal scheme for every combination of α_1/α_2 and τ_2/τ_1, within reasonable given ranges, in terms of minimal achievable RSD:

$$\min_{g/\tau_1,\ g/dt,\ n} \mathrm{RSD} = f(\alpha_1/\alpha_2,\ \tau_2/\tau_1;\ g/\tau_1,\ g/dt,\ n)$$

or simply minRSD = f(α_1/α_2, τ_2/τ_1). However, to compare our results with previous literature, in some figures we show RSD as a function of g/τ_1 and τ_2/τ_1, where g sometimes is often symbolized by Δt in literature. This analysis will be denoted as RSD = f(g/τ_1, τ_2/τ_1).

2.3.3 Lifetime determination methods

2.3.3.1 Rapid Lifetime Determination (RLD)

With RLD, exactly four gates are needed in the double-exponential decay case, because, as shown in Equation (2-7), there are four unknowns to be determined when none of the fluorophore information (or, only rough information) is known. Sharman et al. [63] have shown the formula to calculate these four unknowns in contiguous gating conditions ($g = dt$ in our notation) and 50% overlapping gating conditions ($g = 2dt$ in our notation), and they have used closed-form solutions for overlap = 25% and 75 % as well.

Here, we develop the general closed-form solutions for double-exponential RLD with arbitrary overlap in order to find the optimal conditions including gate overlapping. This is shown as follows (D_0, D_1, D_2, and D_3 are the integrals of the 1st, 2nd, 3rd, and 4th gates, respectively, as shown in Figure 2-4).

$$\tau_1 = \frac{-dt}{\ln(y)}$$

$$\tau_2 = \frac{-dt}{\ln(x)}$$

$$\alpha_1 = \frac{-(xD_0 - D_1)^2 \ln(y)}{dt(x^2 D_0 - 2xD_1 + D_2)[1 - (\frac{xD_1 - D_2}{xD_0 - D_1})^{\frac{g}{dt}}]}$$

$$\alpha_2 = \frac{-R\ln(x)}{dt(x^2 D_0 - 2xD_1 + D_2)[x^{\frac{g}{dt}} - 1]}$$

where *R, x,* and *y* are calculated as in [63]:

$$R = D_1 D_1 - D_2 D_0$$

$$P = D_3 D_0 - D_2 D_1$$

$$Q = D_2 D_2 - D_3 D_1$$

$$DISC = P^2 - 4RQ$$

$$x = \frac{-P - \sqrt{DISC}}{2R}$$

$$y = \frac{-P + \sqrt{DISC}}{2R}$$

g/dt is a parameter describing the overlap / gap between two consecutive gates. With the following equation,

$$\frac{g/dt - 1}{g/dt} \times 100\% = overlap(gap)$$

it indicates overlap (gap) in percentage with respect to the gate width. Positive and negative values indicate overlap and gap, respectively.

2.3.3.2 Nonlinear curve fitting methods – WNLLS and MLE

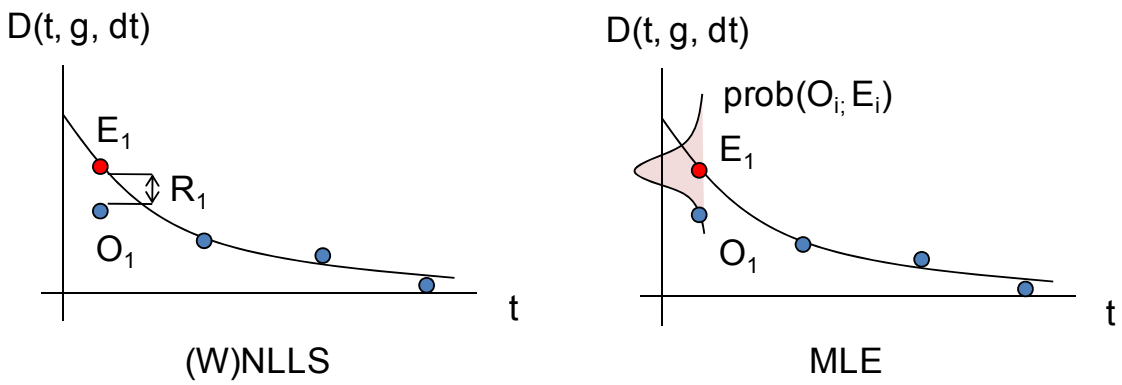

Figure 2-5 The concepts of nonlinear curve fitting used in time-gated fluorescence lifetime measurements. (W)NLLS minimizes the sum of (weighted) squares of the residuals (R_i with i for different gates) and MLE maximizes the likelihood (product of probabilities prob(O_i, E_i)), when adapting the model parameters (the lifetimes and pre-exponential terms) in order to fit the data values. O_i: Observation values (from data); E_i: Expected values (from model); R_i: Residual = O_i – E_i; prob: probability density function; $D(.)$: integral under gating as a function.

Figure 2-5 shows the concepts of the two nonlinear curve fitting methods used with time-gated fluorescence lifetime measurements: WNLLS and MLE.

The nonlinear least-squares method can be either weighted or non-weighted. Therefore, (W)NLLS is used in this study to indicate both cases. (W)NLLS minimizes the sum of (weighted) squares of the residuals (R_i with i for different gates) by adjusting the model parameters (the lifetimes and pre-exponential terms) to fit the data values:

$$\min \Sigma_i R_i^2 \text{ for NLLS and } \min \Sigma_i (R_i / \sigma_i)^2 \text{ for WNLLS}$$

where the weighting σ_i is the evaluated standard deviation of the data points. With Poisson-distributed noise,

$$\sigma_i = O_i^{1/2} \text{ or } E_i^{1/2}$$

where O_i = Observation values (from data) and E_i = Expected values (from model).

In our WNLLS approach, the least-squared method is implemented twice in each iteration: first, the pre-exponential terms are solved least-squarely, with weighting of

1/square root of the observed data values, by using Matlab backslash (\), which solves linear least-squared problem using several different matrix manipulation depending on the properties of the matrices. This is then followed by the second minimization of sum of squares with Matlab subroutine fminsearch and with the same weighting factor to find the optimal nonlinear terms τ_1 and τ_2. One of the advantages of this procedure is that there is no need to assign initial conditions (ICs) of α_1 and α_2, preventing any IC errors due to these two otherwise easily deviated parameters. This is beneficial especially for MLE, where the likelihood (described below) responds to ICs of α_1 and α_2 dramatically. Neyman's Chi-squared is minimized in this approach for simplicity ($\sigma_i = O_i^{1/2}$, Poisson noise assumed). The NLLS approach, whose results are mainly used for comparisons, is the same as described above except that there is no weighting.

The second nonlinear curve fitting method, MLE, maximizes the likelihood, which is the product of probabilities prob(O_i, E_i):

max likelihood = max π_i prob(O_i; E_i)

The expected value of photon counts (E) in each gate is given by the calculated integration of each gate under the double-exponential decay curve using evaluated fitting parameters τ_1, τ_2 and α_1, α_2. The expected value is then used to calculate the probability of acquiring the observed data value (O) via the probability density function of Poisson distribution. To simplify the computation of the likelihood, the product of probabilities is converted into a summation by taking its logarithm. With the assumption that each gate is independent, the likelihood becomes

$$L = \sum_n O \log E - E$$

where L is the likelihood function used in the code. The summation is over different gates. The expected value E is calculated with evaluated pre-exponential terms, α_1 and

α_2, solved by Matlab backslash (\) in each iteration, as in WNLLS, but without weighting. The same nonlinear optimization function in Matlab, fminsearch, is used to maximize the likelihood function.

2.3.4 Monte Carlo simulations

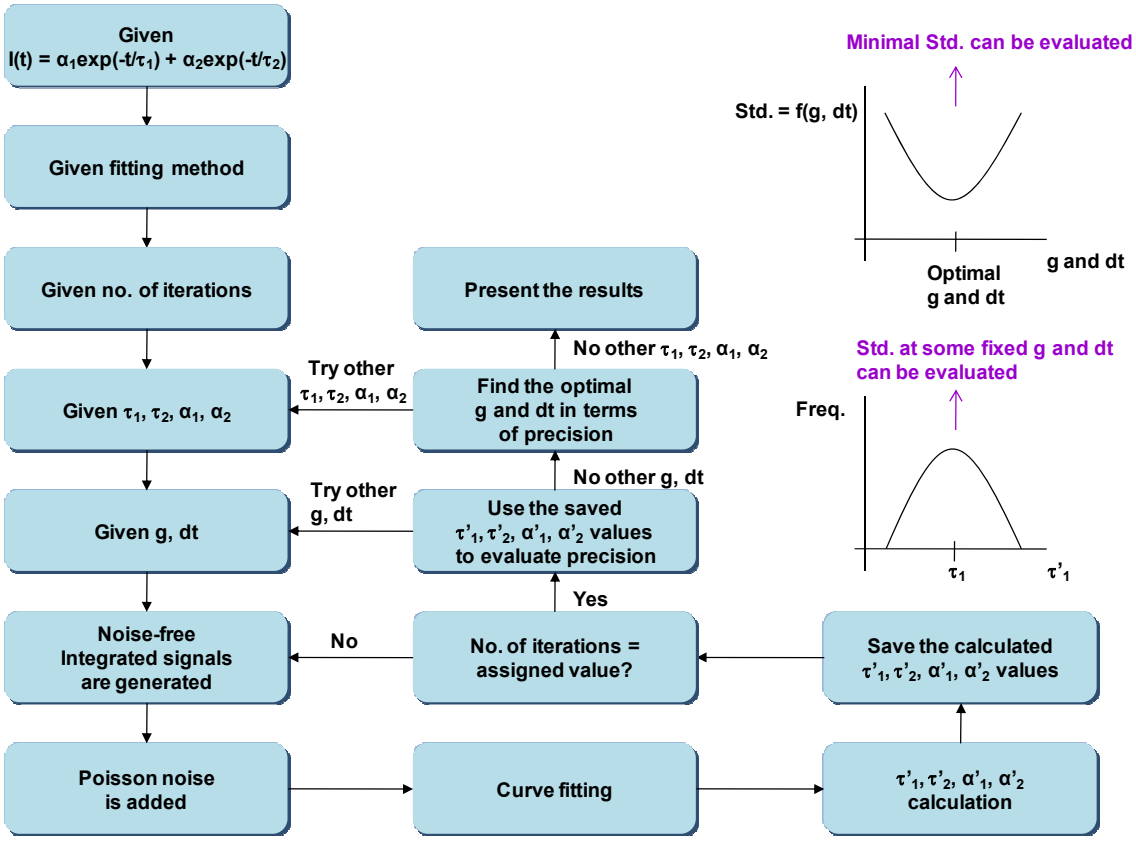

Figure 2-6 The Monte Carlo simulation procedures for the temporal method

The simulations are encoded in Matlab (see Figure 2-6). A noise-free version of double-exponential decay curve is first generated, according to the sample parameters (τ_1, τ_2 and α_1, α_2) and the controllable system parameters (g and dt). Poisson-distributed noise is then added to the time-gated integration signals, and via various lifetime determination algorithms with given system parameters, the sample parameters (noise-affected, hence deviating from the initial given values) are calculated. For each set of parameters, this procedure is repeated to form the distributions of the determined

sample parameters, and the number of Monte Carlo simulations (denoted as "*mc*" below) is 100 for RSD = f(g/τ_1, τ_2/τ_1) analysis and 50 for minRSD = f(α_1/α_2, τ_2/τ_1) analysis (see Section 2.3.2). Larger mc is not preferred not only because of shorter simulation times, but also because of the reasons that will be discussed later in Section 4.1. Finally, the standard deviations and the mean values of the distributions are calculated for each parameter of interest (τ_1, τ_2, f_1, and f_2, see Section 2.3.2) to obtain RSD.

2.4 The spatial approach

2.4.1 Introduction to total variation models

The image processing algorithms commonly used to "denoise" images can be either local or global. Local denoising algorithms are sometimes preferred because it only needs neighboring pixels to implement smoothing and works well in most cases [43]. Global denoising, on the other hand, might be best used for images with repeated patterns, in which fine structures may be preserved since the information of the whole image is adopted to determine the value of a certain pixel in the processed image. A review article provide by Buades et al. summarized a classification of currently used denoising algorithms, as well as some comparisons among them [43].

Total variation (TV) models, based on local denoising algorithms, are very commonly used in medical imaging systems and even non-imaging technologies, because they perform selective smoothing and hence are edge-preserving [44, 45]. For example, a variety of improved TV models [44, 45] and related algorithms have been used with many other image processing techniques / medical imaging systems such as 3D confocal microscope deconvolution [78], X-ray-computed tomography [79], deconvolution-based correction in positron emission tomography [80], image

segmentation [81], and they can be applied to non-imaging medical technologies such as detecting and delineating genomic regions with biased gene expression in cancer [82].

TV models are predicated on the definitions of their "energy" (*E)*, which is minimized through iterations where the processed image (symbolized as "*u*") evolves to a stable state that should be close to the original image without noise corruption. The basic form of the "energy" includes a regularization term, which utilizes total variation (defined as the integral of the absolute value of the gradient of the image, assuming the image is a continuous function) to denoise the input image (symbolized as "*f*"), and a fidelity term, which implements fitting of the processed image to the input image and decides how large the "distance" can be between these two images.

To minimize the defined energy, the gradient descent of *E*, with respect to time, *t*, along the direction of *u* is used with iterations to achieve the final stable *u*. The parameters included in the iteration process are '*delt*', the time interval between two consecutive iterations, and '*nt*', the number of time steps (or iterations). Here, the "time" is just a scale used along the iterations towards the stable *u* and does not involve real time. Sufficiently small *delt* ensures *E* decreases along iterations and sufficiently large *nt* ensures the stable *u* can be achieved.

The Rudin-Osher-Fatemi (ROF) model is an example of a commonly used TV model [83]. The energy is defined as:

$$E = \int |\nabla u| + \lambda \int (f - u)^2 \, dx \tag{2-8}$$

In this model, the fidelity term is defined as a product of a fidelity coefficient (λ) and the square of L^2 norm of $f - u$. In other words, the "distance" between *f* and *u* are evaluated in the L^2 space with the fidelity coefficient λ controlling the "distance" between *f* and the

final stable *u*. The discrepancy rule applies here [84]: the "distance" between *f* and the final stable *u* should be the same as the "distance" between *f* and the uncorrupted images without noise (sometimes negative values may be used in other TV models; therefore they may not really be "distance" in all cases). Indeed, if the denoising process drives *u* in the evaluated space (L^2 space in this case) in the direction to the uncorrupted image without noise, the model with an appropriately chosen λ value will theoretically produce the final *u* the same as the uncorrupted image.

The gradient descent of ROF energy can be derived to obtain a stable *u* and is shown in equation (2-9). A stable *u* (*u* with minimal energy) can be achieved by discretization of u_t (requiring *delt*) and by updating *u* with iterations (requiring *nt*).

$$u_t = \nabla \cdot \left(\frac{\nabla u}{|\nabla u|} \right) + 2\lambda (f - u) \tag{2-9}$$

Practically, TV models can be applied to the images from the signal integration in each gate of an ICCD under a fluorescence decay curve. Therefore, in this study, several TV denoising models are considered to improve the precision of lifetime determination with FLIM by removing the electronically introduced noise in the images. Hence, the uncertainties in lifetime determination can be removed to some degree. Precision and accuracy are investigated via Monte-Carlo simulations, assuming Poisson noise. The algorithms are then applied to live-cell images with single-exponential-decay lifetimes. The results here can deal with the major problem in low-light live-cell imaging and serve as a basis for some higher-order image processing such as image restoration.

2.4.2 Analytical procedures

2.4.2.1 Artificial images and data processing

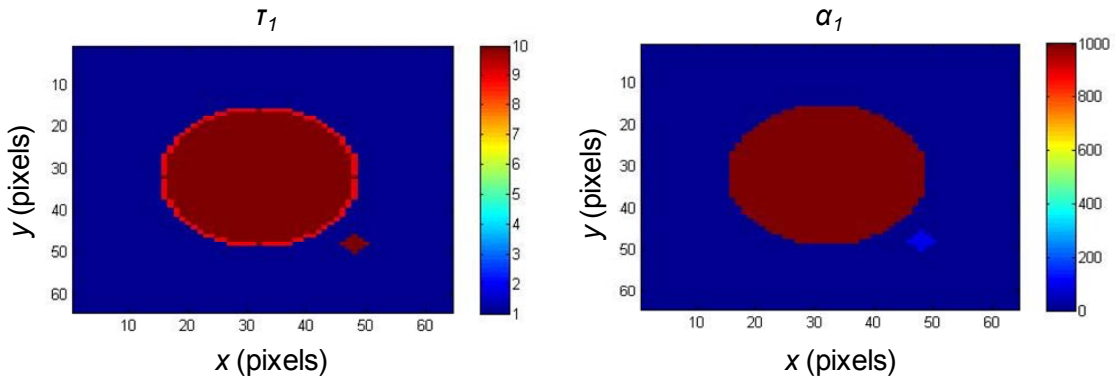

Figure 2-7 The artificial images mimicking the geometry that may be encountered in live-cell FLIM experiments

Because artificial images have predetermined parameters, we first use them to evaluate the accuracy and precision of various TV models. For simplicity, single-exponential fluorescence decay is used to construct these artificial images:

$$I(t) = \alpha_1 \exp(-t/\tau_1) \tag{2-10}$$

As a reminder, $I(t)$ is the fluorescence intensity as a function of time. τ_1 is the lifetime and α_1 is the pre-exponential term representing intensity at time zero. Subscription "1" (indicating the first component) is used here just to be general, since multi-exponential decay can be covered in future studies. In the following analysis, τ_2 and α_2 also exist but are set to some appropriate values such that they will not affect the results.

To mimic the geometry that we may encounter with live-cell FLIM, we use the geometry shown in Figure 2-7 to test various TV models. It has "the inner circle" (the centered solid circle in the left panel), "the ring" (the open circle outside the inner circle in the left panel), and "the satellite" (the small dot to the bottom right of the inner circle). As

an example of the geometry described here, a cell may have fluorophores inside it with some interactions taking place in its membrane, while in another smaller cell or organism the same fluorophores at lower concentration are present. Provided that the 1st dimension (the number of rows) of the image is *m'* and the 2nd dimension (the number of columns) is *n'*, we have the parameter setting, *m'* = *n'* = 64, shown in Table 2-1.

Table 2-1 The parameter setting of the artificial images

	The inner circle	The ring	The satellite
center	(*m'*/2, *n'*/2)	(*m'*/2, *n'*/2)	(3*m'*/4, 3*n'*/4)
radius	*n'*/4	2.1*n'*/8	*n'*/32
τ_1	10	9	10
α_1	1000	1000	100

The artificial images are encoded in Matlab because of its flexibility, and relevant details are provided as follows. The setting of the ring (the outer circle) is valid only outside the area that has been taken by the inner circle. The background τ_1 values and τ_2 are set to one to avoid possible NaN (Not a Number) since in later calculations τ is in the denominators of the exponential terms. This of course will not affect the results since the background α_1 and all α_2 are set to zero (no effective fluorophores). In addition, a global variable called "nzero2" serves as a mask, to keep the values of RSD and RME (further described below in Section 2.4.2.3) outside the regions of interest (i.e. in the background) zero. A variable "filter" serves as another mask so that the results at different locations (such as the inner circle, the ring, and the satellite) can be taken and averaged separately. Of course, we realize that different positions inside each object may have different behaviors due to different geometry (for example, the edge part of the satellite

vs. the pixels inside it), calculating the average is at least our first step to roughly represent the overall behaviors.

In the lifetime calculation module, we use the mode that deals with four gates with a linearized least squares method because it is more precise than the two-gate RLD (rapid lifetime determination) while still easy to handle. The gating scheme of this set of images is *g* (gate width) = 16 and *dt* (the time interval between the beginnings of two consecutive gates) = 4. This gating scheme is the optimal gating scheme for a certain lifetime range in which the lifetime setting above is covered. As discussed later in Section 5.1.1, this gating scheme will play a role in the results of the precision analysis. Before sending the images to the lifetime calculation module, some pre-processing (see Section 2.2.3) is still needed to remove unrealistic lifetime values. For the artificial images, only 'taurange' = 20 is used, although it actually does not affect the results because 'nzero2' covers its task.

2.4.2.2 Monte Carlo simulations

Monte Carlo (MC) simulations, similar to those used in the temporal method, are used here for the evaluation of the accuracy and precision of various TV models (Figure 2-8). In each MC simulation, one version of the images with Poisson-noise is generated. These images are then denoised and the lifetime is calculated for each pixel. The resulting lifetime map is stored and this procedure is repeated, with the same original images but different Poisson noise. A variable "*mc*" is assigned to indicate how many times this procedure is repeated. Usually, if time allows, *mc* = 100 is used. Sometimes *mc* = 50, 20, or 10 are used, too, for some smaller tests. The effect of different *mc* on the results is described below in the next Section.

2.4.2.3 RSD and RME

After all lifetime values from the MC simulations are collected, mean lifetime values and the standard deviation (std.) from all the MC simulations are calculated, and these values are used for the evaluation of accuracy and precision with RSD (relative standard deviation) and RME (relative mean error). As mentioned previously in Section 2.3.2, RSD (%) is defined as [standard deviation / mean value] × 100. RME (%), on the other hand, is defined as [(mean value – correct value) / correct value] × 100. Again, the artificial images are needed because they provide the necessary real lifetime values. Of course, highly controlled (or highly repeated) experiments can produce accurate results to serve this purpose as well, but systematic error sometimes cannot be removed entirely.

We assume there is no RME bias resulting from different mc values, although with small mc we should have greater RME variance. The reasons are as follows. If the "counts" (or the intensities) at a certain location (pixel) are sufficiently high, the distribution of the lifetime values from MC simulations at that location approximates normal distribution. In addition, even if the Poisson distribution cannot be accurately approximated by normal distribution, according to The Central Limit Theorem, we can still approximate the distribution of the mean values of the lifetimes as normal, if the number of subjects (the value of "*mc*") is sufficiently high. Therefore, we can assume the mean value from our MC simulations is most probably the mean of the population with the same setting.

However, RSDs do have bias resulting from different mc values, since the distribution of the ratio, sample variance / population variance, follows Chi-squared distribution. This distribution has a mode smaller than its mean. This effect is relatively smaller if mc is larger. Therefore, if the same setting is run with different mc values, the

calculated RSD values are likely smaller with smaller mc values. This is justified individually in the following sections.

As a summary, to do the MC simulation procedures for the spatial method as shown in Figure 2-8, we first generate noise-free artificial images with the specified parameters (α_1, τ_1, g, dt), and, after Poisson noise addition and denoising in the iterations, RSD and RME values are calculated for the estimation of accuracy and precision. Compared to Figure 2-6 (the temporal method), there are the following differences:

1. Single exponential decay (Only τ_1 is calculated)
2. Four-gate protocol is used
3. τ_1,α_1, g, and dt are all fixed
4. Both precision and accuracy are evaluated

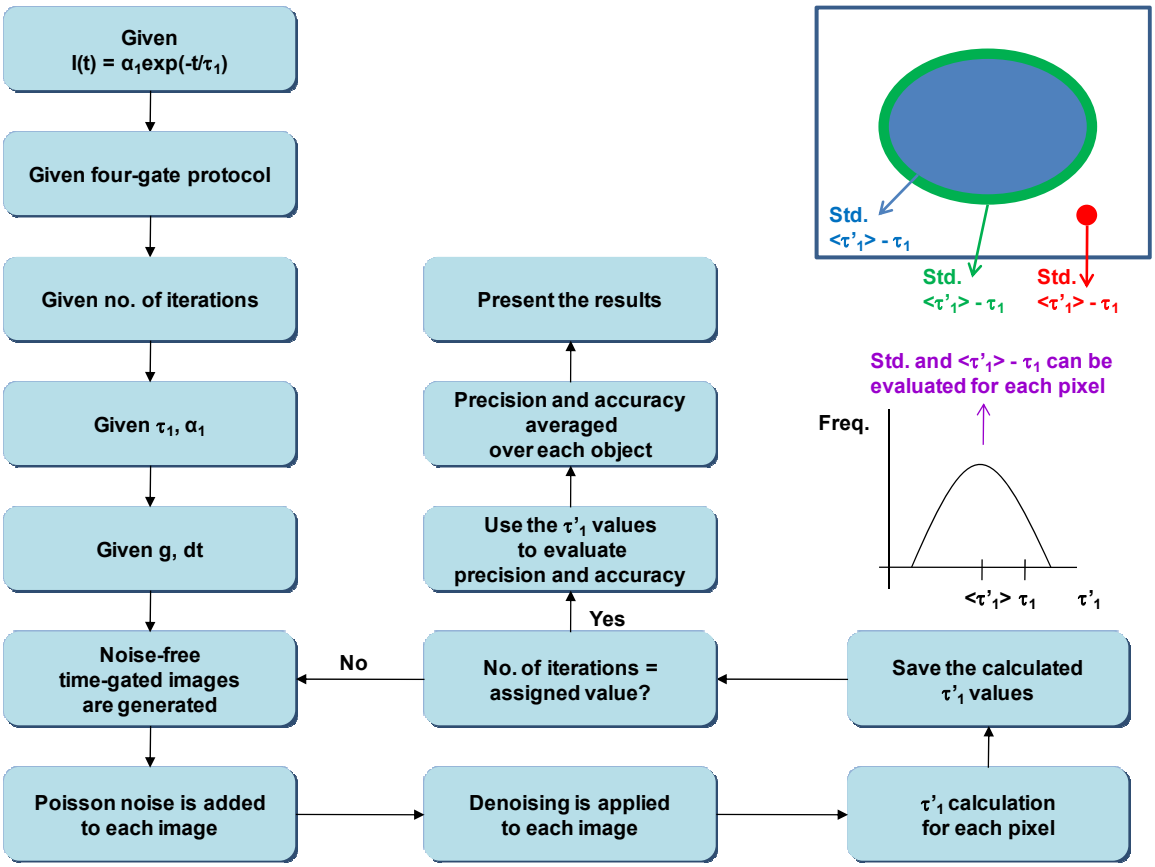

Figure 2-8 The Monte Carlo simulation procedures for the spatial method. We first generate noise-free artificial images with the specified parameters (α_1, τ_1, g, dt), and, after Poisson noise addition and denoising in the iterations, RSD and RME values are calculated for the estimation of accuracy and precision.

Chapter 3 Well-controlled FLIM for FRET detection in living cells

The goal of the study in this chapter is to provide a better quantitative FLIM-based detection of molecular interactions in living cells. We demonstrate that fluorescence resonance energy transfer (FRET) can be better detected with FLIM than with intensity. The approaches described here significantly help us determine physiologically relevant interactions in living cells that can provide us deep insight into treatments of diseases such as breast cancers as mentioned in this chapter.

3.1 Introduction to FRET and FLIM-based FRET detection

Förster (or Fluorescence) Resonance Energy Transfer (FRET) theory was developed by Professor Theodor Förster [85] and is a commonly used technique for measuring the spatial distance between two (or multiple) fluorophores. Cell biologists exploit FRET to measure the distance between two sites on a macromolecule, the distance between two proteins attached with fluorophores and hence whether and how these two proteins interact. FRET is regarded as an *in vivo* “nanoscale ruler”, since it can be monitored in living cells, and the distance for FRET to occur is usually within several nanometers, exactly the distance comparable to the dimensions of biological macromolecules. The diameter of many proteins, the distance within which proteins interact in living cells, the thickness of biological membranes, and the distance between sites on multisubunit proteins are typically within this distance.

FRET mandates the presence of at least one donor-acceptor (D-A) pair, although more than one such pairs and hence distances can be involved. FRET occurs when the donor emission spectrum overlaps with the acceptor excitation spectrum. After donor excitation, energy will be transferred non-radiatively if the D-A pair is in close proximity (i.e. via the non-radiative pathway illustrated in Figure 2-1 without photo emission), as a result of long-range dipole-dipole interaction between the D-A pair. In other words, the acceptor does not reabsorb the photons emitted from the donor as a means of energy transfer, which also implies that the intervening solvent or molecule has little effect on the efficiency of FRET.

How close exactly for the D-A pair will FRET occur? Quantitatively, Förster distance is defined as the distance at which the energy transfer efficiency is 50% and the energy transfer efficiency (E) is defined as

$$E = \frac{k_T}{\tau_D^{-1} + k_T} \tag{3-1}$$

where τ_D is the donor lifetime in the absence of acceptor and k_T is the energy transfer rate from a donor to an acceptor. k_T is given by

$$k_T = \frac{1}{\tau_D}\left(\frac{R_0}{r}\right)^6 \tag{3-2}$$

where R_0 is the Förster distance and r is the D-A distance. As we can see, when $r = R_0$, E = 50%, as described in the definition of Förster distance. Also, the dependence of k_T on r is highly nonlinear and strong with D-A distance near R_0; when $r = 2R_0$, the energy transfer efficiency drops to only 1.56%, according to Equations (3-1) and (3-2).

In order to detect FRET efficiently, D-A pairs with longer R_0 are preferred. The typical value of R_0 is in the range of 20-60 Å, depending on the extent of D-A spectra overlap, the D-A orientation, the refractive index of the medium, and the quantum yield (see Equation (2-4)) of the donor in the absence of acceptor. Since the D-A orientation is usually assumed to be dynamic and random, while the refractive index of the medium is typically treated as a constant for biomolecules in aqueous solutions, in usual cases R_0 is considered dependent only on the optical properties of the fluorophore pairs and is approximately fixed for a given D-A pair.

The most common application of FRET is to measure the distances between two sites on a macromolecule. FRET can be used to monitor any phenomena with changes in the D-A distance, such as conformational changes of a macromolecule, or the cleavage of a macromolecule by enzymes. In these cases, endogenous fluorophores are usually used. For instance, tryptophan can be used as a donor, and a ligand that binds to a ligand binding site can be an acceptor.

Exogenous fluorophores (eg. CFP-YFP) are also used as D-A pairs in cell biology. In this case, donor and acceptor vectors are constructed with the proteins of interest, typically the proteins between which the *in vivo* interactions are unknown. The fluorophores can be attached on either the N-terminal or the C-terminal of the proteins, depending on the locations of functional domains of the proteins. The vectors are transfected into the model cells, usually the cell kinds that are easy to transfect, or related to the cells where the protein functions and interactions are of interest. Vector sizes could be a factor that affects FRET, if vectors are not transfected efficiently [86, 87], making the signals too weak and noisy, or if the ratio of tranfected donor to acceptor is too high or too low.

To measure FRET, both steady-state and time-resolved data can be used. Since k_T is a decay rate in addition to already existent Γ and k for donor emission decay in the absence of acceptor, the lifetime is shortened and the steady-state intensity is lowered if FRET occurs. The degree of shortening / lowering is fixed if the D-A distance r is fixed, which is usually the case for labeled proteins, but in solution or membranes, where the donors and acceptors can diffuse freely, this may not be true, and the calculation of an averaged k_T from the D-A spatial distribution is required. Also, if considering a multi-exponential decay, which in fact happens frequently in biomolecules, an averaged τ value over all exponential curves is needed as well.

Pioneering studies on FRET were implemented with intensity-based methods [88], including sensitized emission of acceptor from donor quenching [89, 90], ratiometry of donor to acceptor intensities, donor dequenching with acceptor photobleaching, donor photoquenching with photoactivated acceptor [91], and stoichiometry FRET [92].

On the other hand, FRET-FLIM combines FRET and lifetime imaging, which can be highly favored over intensity-based FRET for several reasons [17, 93, 94]. For FRET with weak signals or low energy transfer efficiency, a minute intensity artifact can lead to very high impreciseness in FRET detection. For example, if detection of FRET with energy transfer efficiency of ~10% is desired, the variation in fluorescence emission intensity among and within cells might need to be controlled to be very low, and this may not be an easy task for low-signal experiments, for wide-field fluorescence microscopy, or for experiments with non-uniform transfection distribution. Using FLIM to detect FRET with E = ~10% allows intensity variation to be as high as 30%, and theoretically even higher, given molecular micro-environment and later data processing procedures not affected.

FRET-FLIM has already been widely used in many biological applications, especially in living cells [93, 95, 96]. For example, a two-photon FRET-FLIM system for protein localization was characterized [97], and plasma membrane organization in cowpea protoplasts was studied using FRET-FLIM with different GFP-fused proteins [98]. A FRET-FLIM-based detection of phosphorylated protein localization, performed in frequency domain, was conducted as well [99]. A review on FRET-FLIM has provided a table of commonly used FRET fluorophore pairs for FLIM studies [89].

3.2 Use of FRET to monitor RhoC interactions

RhoC (Ras Homology Protein C) has been found to be a transforming oncogene for mammary epithelial cells and has been identified as a specific marker of aggressive breast cancers. Its activation can lead to a highly invasive, angiogenic, and metastatic phenotype, extremely akin to inflammatory breast cancer, which has very poor prognosis from its inception. However, the detailed biophysical mechanisms for activation and inhibition of it are not completely understood [100]. Therefore, it is critical to characterize molecular interactions of oncogene RhoC in the living cells in order to understand its behaviors and how it performs its functions as an oncogene, which will provide us valuable information when developing novel treatments towards inflammatory breast cancer.

RhoC and its isoforms RhoA and RhoB belong to the Rho family within the Ras GTPase superfamily. In its active state, RhoC is associated with GTP and localizes to the membrane, where it is capable of binding to its effectors and participating in the focal adhesion complex (FAC), to which microtubules converge [100]. When RhoC is inactive, it is associated with GDP and is able to bind with RhoGDIγ (Rho Guanine nucleotide Dissociation Inhibitor gamma) in the cytoplasm.

In order to study the molecular interactions of Rho GTPases, many researchers utilized FRET [101-104], or designed and optimized the FRET probes specifically for this group of proteins [105, 106]. In particular, some research groups used FLIM-FRET to study the Rho family [95, 107-109].

In this section, we explore the molecular interactions of RhoC in living cells with FLIM-FRET experiments. We intend to detect the RhoC inactive-form interactions with RhoGDIγ by using CFP/YFP pair (Figure 3-1). The FRET donor (CFP, or Cyan Fluorescent Protein) was tagged onto RhoGDIγ while the accepter (YFP, or Yellow Fluorescent Protein) tagged onto RhoC. Both CFP's intensity and lifetime of fluorescence emission will be decreased as a result of FRET, if CFP is in proximity of YFP as RhoC interacts with RhoGDIγ. The enhanced versions of CFP we have used include ECFP and Cerulean, and the YFP versions include EYFP and Citrine.

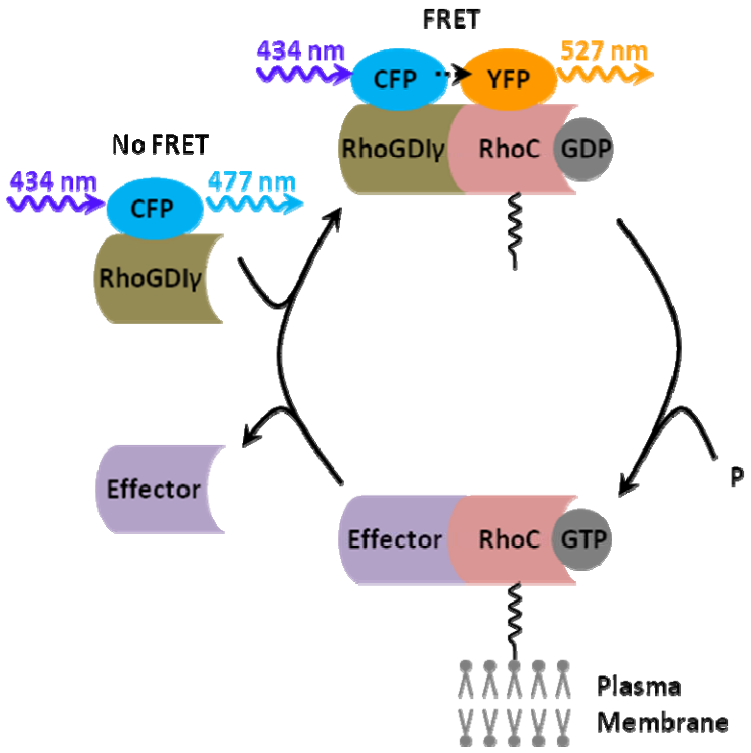

Figure 3-1 Schematic depiction of FRET studies on RhoC and RhoGDIγ. When active, RhoC is associated with GTP and localizes to the membrane, where it is capable of binding to its effectors. When inactive, it is associated with GDP and is able to bind with the inhibitor RhoGDIγ in the cytoplasm. Interactions between RhoGDIγ and RhoC causes FRET to occur from the donor (CFP) to the acceptor (YFP). Approximate excitation and emission maxima of CFP and YFP are labeled. The decrease of donor fluorescence lifetime is monitored to detect FRET.

Monkey kidney epithelial (CV-1) cells were used as our model cells. They were cultured to 60-75% confluency in MEM (CellGro, Mediatech Incorporated, Herndon, VA) supplemented with 10% FBS (Gibco, Invitrogen Corporation, Carlsbad, California) at 37^{o}C under 10% CO_2 before plasmid (a circular DNA used as a vector for gene transfer) transfection with GeneJammer transfection reagent (Stratagene, La Jolla, CA).

Cells were imaged with the FLIM system using a Zeiss Fluar 40X oil-immersion objective. ECFP and Cerulean fluorescence was excited at λ_{ex} = 436±10 nm using the laser dye Coumarin 440 and collected at λ_{em} = 480±20 nm.

Student's t-tests are used to compare the mean values of lifetimes or intensities of the FRET donors. Homoscedastic t-tests are used, assuming two-sample equal variance,

since the compared two groups are independent with randomly assigned subjects. Degree of freedom (df) is defined as the sum of numbers of subjects in the two groups minus two. Significance level is set to 0.1, although much smaller *p*-values are always acquired for stronger confirmation of statistical significance.

Figure 3-2 shows ECFP intensity (*left*) and lifetime (*right*) values of cells transfected with ECFP (*top*) and Cerulean (*bottom*) fusion plasmids. Group 1 (left box plot in (a) and (b)) consisted of 37 cells transfected with ECFP-RhoGDIγ and EYFP. This group was used as a negative control as no FRET between ECFP and EYFP would have occurred due to the interaction of RhoGDIγ and RhoC. Group 2 (right box plot in (a) and (b)) consisted of 60 cells transfected with ECFP-RhoGDIγ + EYFP-RhoC. Groups 3 and 4 (left and right box plots in both (c) and (d)) consisted of 30 cells transfected with Cerulean-RhoGDIγ + EYFP and 60 cells transfected with Cerulean-RhoGDIγ + EYFP-RhoC, respectively. The first quartile, the median, and the third quartile are shown within the boxes and the 10^{th}/90^{th} percentiles outside the boxes. All the plots are labeled with *p*-values of the Student's t-test, together with the mean intensity or lifetime value and standard deviation for each group of cells.

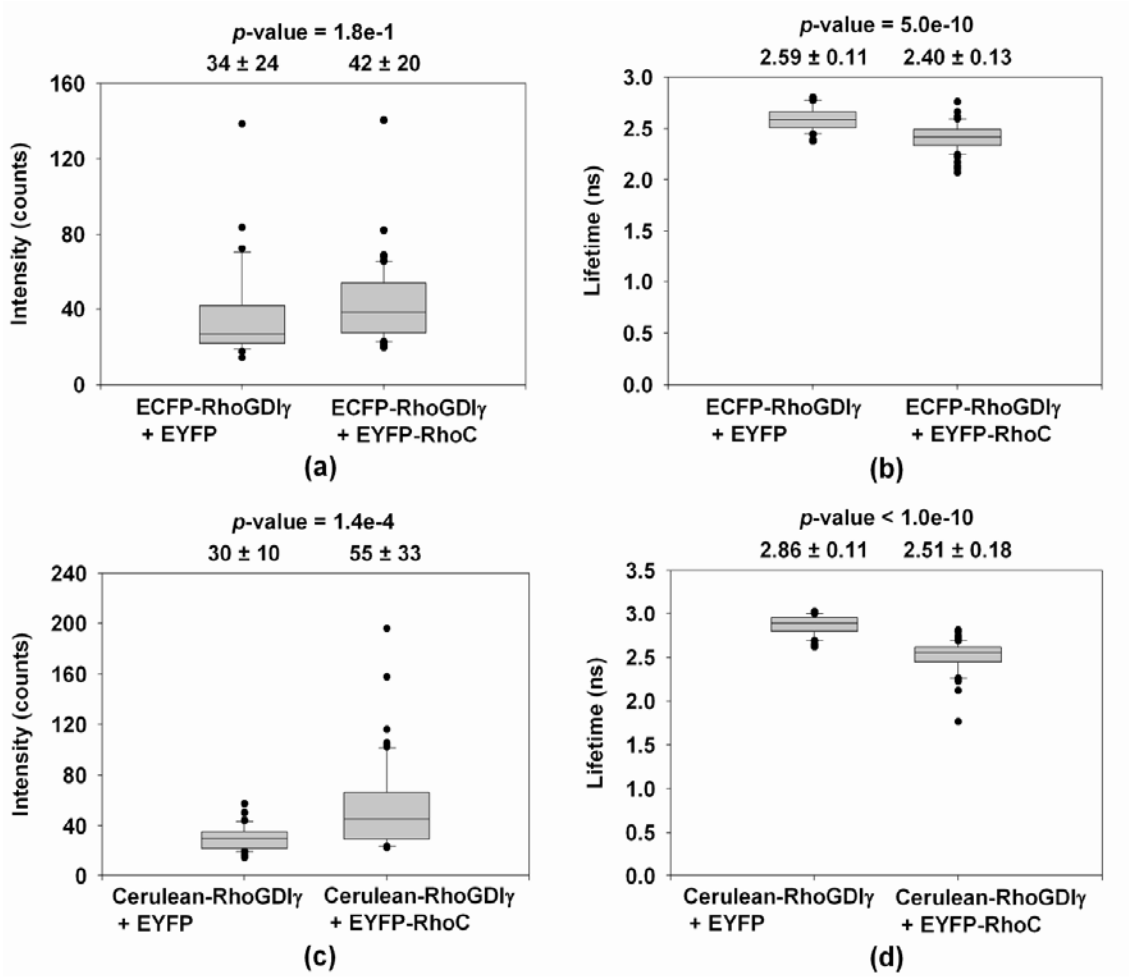

Figure 3-2 ECFP intensity (left) and lifetime (right) values of cells transfected with ECFP (top) and Cerulean (bottom) fusion plasmids. Group 1 (left box plot in (a) and (b)) consisted of 37 cells transfected with ECFP-RhoGDIγ and EYFP. Group 2 (right box plot in (a) and (b)) consisted of 60 cells transfected with ECFP-RhoGDIγ + EYFP-RhoC. Groups 3 and 4 (left and right box plots in both (c) and (d)) consisted of 30 cells transfected with Cerulean-RhoGDIγ + EYFP and 60 cells transfected with Cerulean-RhoGDIγ + EYFP-RhoC, respectively. The first quartile, the median, and the third quartile are shown within the boxes and the 10th/90th percentiles outside the boxes. All the plots are labeled with *p*-values of the Student's t-test, together with the mean intensity or lifetime value and standard deviation for each group of cells. (a) and (c) Fluorescence intensities suffered from high variation within the cell population and revealed no statistically significant difference between groups by the student's t-test. (b) and (d) The FRET-induced decreases in lifetime (group 2 vs. group 1; group 4 vs. group 3) were statistically significant (*p*-value < 0.05)), indicating RhoGDIr-RhoC molecular interaction. [32]

Our FLIM-FRET results confirmed the RhoC inactive-form interactions with RhoGDIγ in living cells. Figure 3-2 (a) and (c) show large variations of ECFP and Cerulean fluorescence intensity among cells within groups, making it difficult to interpret intensity-based measurement without lengthy calibration processes. In addition, the experimental

groups often show higher mean intensities than those of the negative controls, probably due to higher transfection efficiency of ECFP or Cerulean vectors with weaker competitors in the experiemental groups, since sizes of vectors can affect transfection efficiency [17]. However, interaction between RhoGDIγ and RhoC is evidenced by the decrease of ECFP fluorescence lifetime in the experimental groups (group 2 and group 4), as compared to the corresponding negative control groups (group 1 and group 3), as shown in (Figure 3-2 (b) and (d)). The difference in ECFP fluorescence lifetime is statistically significant, as confirmed by a Student's t-test with a *p*-value < 0.05. The interaction between RhoGDIγ and RhoC was subsequently confirmed using a biochemical assay [32].

As a summary, plasmids encoding ECFP-RhoGDIγ and EYFP-RhoC fusion proteins were transfected into CV1 cells for optical imaging in our laboratory. The results indicated that there was a statistically significant difference between the lifetime of ECFP in our experimental group (ECFP-RhoGDIγ + EYFP-RhoC double-transfected CV1 cells) and that in our only negative control (ECFP-RhoGDIγ + EYFP double-transfected CV1 cells) with *p*-value = 5.0e-10. In addition, we introduced Cerulean-RhoGDIγ in place of ECFP-RhoGDIγ and statistically more significant results were obtained (*p*-value < 1.0e-10) [32].

In the following sections of this chapter, we incorporate further analyses and improvements into this live-cell FLIM-FRET system.

1. We compare the consistency and reproducibility of results obtained with ECFP and Cerulean in our system, in order to explore in details the influence of using different fluorescent probes on our statistical analysis.
2. We include positive controls and one additional negative control (CFP-RhoGDIγ single-transfected cells), which are an essential part of any FRET experiment to

identify systematic errors and non-specific FRET. Both negative controls are required, because while comparison of CFP-RhoGDIγ and CFP-RhoGDIγ + YFP indicates possible non-specific FRET in the system, comparison of CFP-RhoGDIγ and the experimental group provides more information for quantitative FRET efficiency determination, although in this case a multi-exponential decay model may be needed for further analysis, depending on the fluorophores used.

3. In this section, our experiments were performed under room temperature without any control for dissolved CO_2 concentration in the media. Therefore, we could not rule out the possibility that the detected molecular interactions in living CV1 cells might not really happen under physiological conditions. In light of this, the following sections further investigate the influence of additional environmental factors, including pH (controlled by CO_2 concentration in equilibrium with media) and temperature, on our FLIM-based FRET measurements with living cells, such that we can remove any possible artifacts introduced by our experimental procedures. Incorporation of these environmental controls may affect fluorophore performance (since they are engineered fluorescent proteins and usually designed to have better translation, folding, and optical properties under physiological conditions), donor lifetime values, degree of molecular interactions reflected by FRET efficiency, and other cellular responses.

4. To confirm that there are no other unexpected systematic errors, each condition further includes duplicate groups, which should not exhibit any statistically significant difference when their mean values are compared.

3.3 Choice of fluorophores

Choice of a better fluorophore can improve the consistency of FLIM-FRET results. In our experiments, Cerulean offers more consistent results favoring RhoC / RhoGDIγ inactive interaction in live CV1 cells via detection of FRET to EYFP, compared to common ECFP / EYFP FRET pair.

The intensity images and lifetime maps of representative CV1 cells transfected with three vector conditions (including one additional negative control) are shown in Figure 3-3. In this case, Cerulean served as the FRET donor while EYFP was the acceptor. With the same pseudo-color scale, intensity images showed more variability both within and between different vector conditions, while lifetime maps were more uniform and independent of intensity variability. The lifetime values (mean ± standard deviation, in ns) were 2.51 ± 0.18 for cells transfected with Cerulean-RhoGDIγ + EYFP-RhoC, 2.86 ± 0.11 for cells transfected with Cerulean-RhoGDIγ + EYFP, and 2.88 ± 0.17 for cells transfected with Cerulean-RhoGDIγ. This result indicated that there were molecular interactions between RhoC and RhoGDIγ, with a *p*-value < 1.0e-10.

The lifetime maps shown in Figure 3-3 also reveal the need of improving the precision of lifetime determination, since, even if we can clearly see the lifetime values are lower in the lifetime map of Cerulean-RhoGDIγ + EYFP-RhoC, all the three lifetime maps are still very noisy and prevent us from discovering any sub-cellular patterns and features. In Figure 3-3, most of the cells have total photon counts of only 500 or lower. Improvements of precision in our FLIM system will be covered in Chapter 4, Chapter 5, and Chapter 6. For demonstrations of precision improvements, see Figure 5-4 and Figure 6-1 for live CV1 cells and fluorescent beads, respectively.

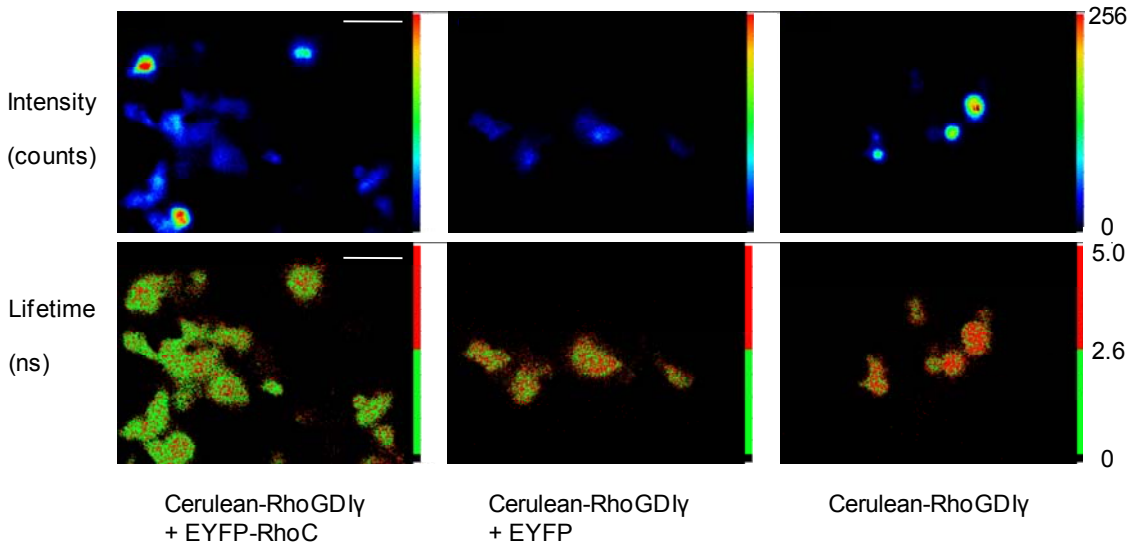

Figure 3-3 The intensity images and lifetime maps of the CV1 cells transfected with three different vector combinations. In the lifetime maps, the pixels with lifetime longer than 2.6 ns are shown in red; the others are in green. The experimental group exhibits a clearly lower lifetime compared to the two negative controls, and this result suggests the presence of interactions between RhoC and RhoGDIγ. The intensity images, on the other hand, do not clearly suggest such interaction, due to higher inter- and intra-cellular variations. Scale bar = 70 μm.

The above RhoC / RhoGDIγ interaction was more consistently observed with Cerulean in live CV1 cells (such as the results shown in Figure 3-3) via detection of FRET to EYFP, compared to the common ECFP / EYFP FRET pair. This consistency was observed in three repeated experiments conducted with independently cultured and transfected sets of cells, in which FRET was detected by comparing the lifetimes of Cerulean. However, when the same experiments were performed with ECFP instead of Cerulean, they did not always provide significant *p*-values for a lower lifetime of ECFP in the ECFP-RhoGDIγ + EYFP-RhoC group versus its negative control (ECFP-RhoGDIγ + EYFP). This result was especially noticeable when the signal-to-noise ratio was low or the number of samples was not high enough.

Cells transfected with only Cerulean-RhoGDIγ do not provide for any random collision of donor and acceptor. Therefore, comparison of this negative control with the one that includes an acceptor provides knowledge of not only possible random collisions

but also any unexpected binding of acceptor to donor or to donor-bound protein (RhoGDIγ in this case). Comparisons of the two negative controls, Cerulean-RhoGDIγ and Cerulean-RhoGDIγ + EYFP, did not reveal any statistically significant *p*-values, meaning that they were both appropriate negative controls, and that, given our experimental conditions, random EYFP molecules in the cytoplasm did not cause any significant occurrence of non-specific FRET. However, when using ECFP instead of Cerulean in this comparison, some significant *p*-values were obtained against the corresponding null hypotheses, indicating that unwanted interactions or random binding events might have taken place when ECFP served as the donor.

To further compare Cerulean with ECFP, the intensity and lifetime of ECFP and Cerulean in donor-only CV1 cells (ECFP-RhoGDIγ-transfected cells vs. Cerulean-RhoGDIγ-transfected cells) were compared with Student's t-tests.

The fluorescence intensity was first compared and we found that Cerulean has higher fluorescence intensity compared to ECFP in living CV1 cells when fused to RhoGDIγ in the absence of RhoC and FRET accepter EYFP. Three repeated experiments were conducted for intensity comparisons of Cerulean and ECFP. In our third experiment with highest degree of freedom (the results shown in Figure 3-3), the comparison of fluorescence intensity of ECFP in ECFP-RhoGDIγ (40.8 ± 25.4 counts, n = 34) with that of Cerulean in Cerulean-RhoGDIγ (58.1 ± 45.4 counts, n = 26) indicated there is a statistically significant difference (*p*-value = 0.033) favoring higher Cerulean intensity than ECFP intensity, despite of the large standard deviations. Although this difference in the mean intensities is not very obvious, higher intensity of Cerulean is consistent with the literature. However, the ratio of the mean intensity values is smaller in our results (1.42) compared to the literature (2.5) [110].

Cerulean has longer fluorescence lifetime compared to ECFP in living CV1 cells when fused to RhoGDIγ in the absence of RhoC and FRET accepter EYFP. We constantly obtained statistically significant *p*-values (< 0.006) suggesting that the lifetime of Cerulean is greater than that of ECFP in our constructs in live cells. The ratios of Cerulean lifetime to ECFP lifetime were 1.10, 1.08, and 1.04, respectively. The ratio of the lifetimes in the literature [110], obtained via single exponential decay, is 1.10.

The differences in the ratios of the lifetimes and the intensities between our results and the literature may be due to the different environments of the fluorophores (fluorophores fused with other proteins in live cells vs. purified fluorophores) and the different detection systems.

3.4 Temperature control

In our FLIM system, temperature control is achieved by using Delta T dishes along with a plate heater and an objective heater (Bioptechs, Inc., Butler, Pennsylvania). The temperature of the plate heater is set to 35 ^{o}C, and the objective heater 35.2 ^{o}C. They are set lower than 37 ^{o}C to compensate for the thermal characteristics of the devices. Stable temperature at 37 ^{o}C is then maintained.

Temperature can affect donor lifetime and the resulting FRET efficiency calculation. To explore the effect of temperature on FRET donor lifetime, we conducted an experiment with one of our negative controls, CV1 cells double-transfected with Cerulean-RhoGDIγ and EYFP. In our results (Figure 3-4) we observed a shorter lifetime of Cerulean when the temperature was controlled at 37 ^{o}C, as compared to room temperature, with a statistically significant *p*-value (< 1.0e-10). Furthermore, the lifetime difference due to temperature change was also confirmed with CV1 cells transfected with Cerulean-RhoGDIγ only (*p*-value < 1.0e-10). On the other hand, the differences in

intensity exhibited large variances and were therefore not statistically significant enough to draw any conclusions.

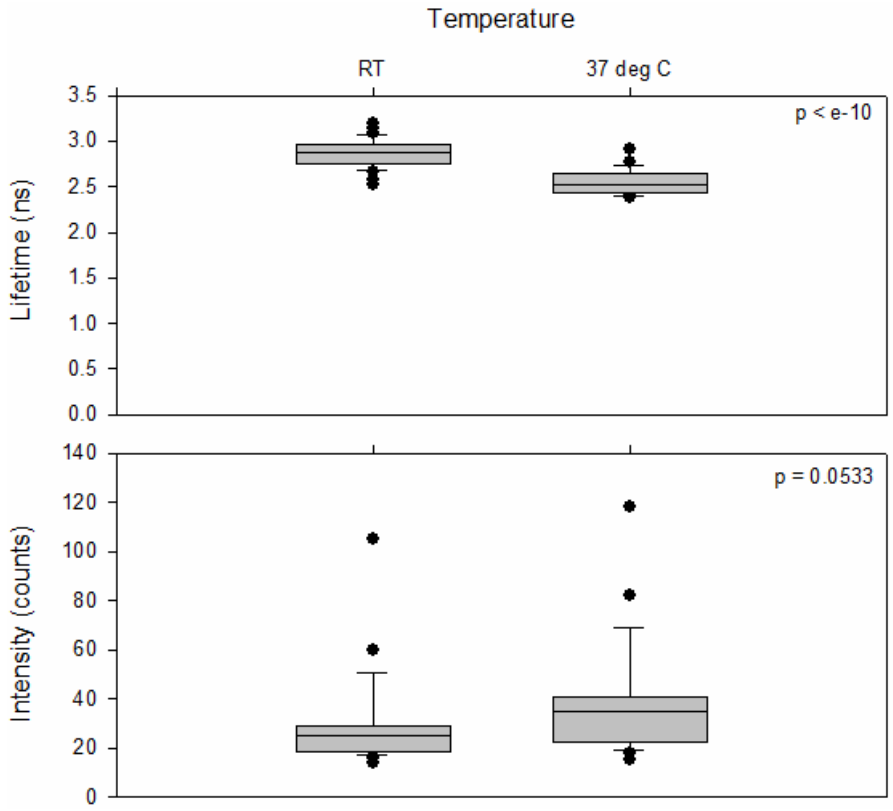

Figure 3-4 Lifetime and intensity of FRET donor (Cerulean in this case) versus temperature. While the lifetime change due to temperature difference can be clearly observed with a small *p*-value, the differences in intensity exhibited large variances and were therefore not statistically significant enough to draw any conclusions. This lifetime change can therefore be included in later FRET-FLIM measurements. RT = room temperature.

3.5 CO_2 control

The CO_2 control was simply done by using a heated lid (Bioptechs, Inc.) to enclose the delta T dishes with CO_2 flowing into it. A peristaltic pump (Model P720, Instech) with adjustable flow rate 0 – 110 (corresponding rate with 1/16" inner diameter tubing is 0 – 80 ml/hr, linearly). For the pH vs. time experiments (Figure 3-5), at the indicated time points the chamber was temporarily opened for the pH measurements, each of which was taken within one minute.

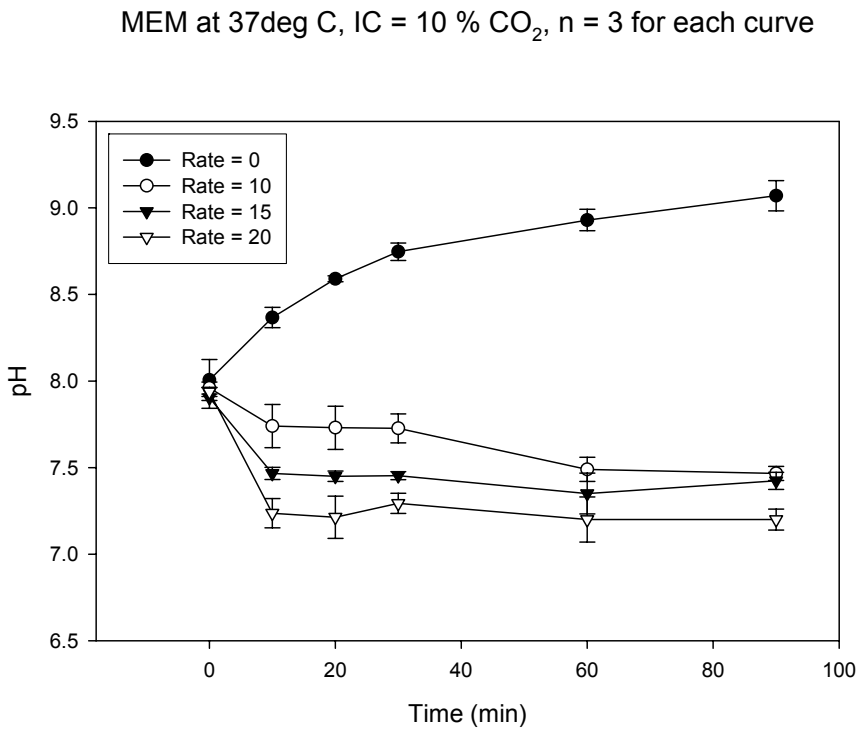

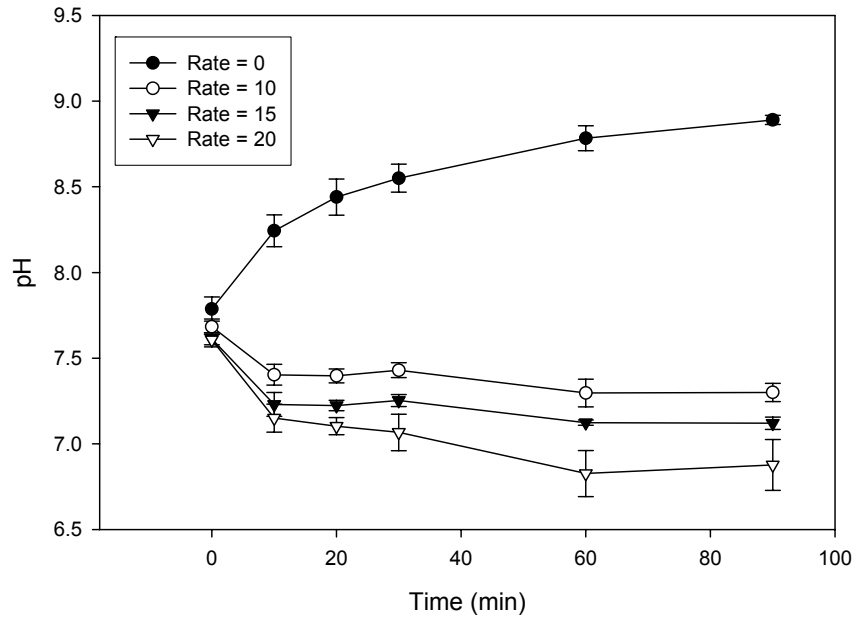

Figure 3-5 The results of pH values detected with different CO_2 flow rates at time points 0, 10, 20, 30, 60 and 90 minutes. Time point zero is defined as the time right after the medium in Delta T dish was transported from incubator at equilibrium with 10% CO_2 (as the initial condition, IC) to the plate heater on the FLIM system. Temperature was controlled at 37 ^{o}C. F-12 medium is included in this experiment for future experiments where inflammatory breast cancer (IBC) cell line SUM149 will be used as model cells.

Figure 3-5 shows the pH dependence on the CO_2 flow rates through time on our FLIM system. In the experiments involved in Figure 3-2 and Figure 3-3, each condition (or each plate of cells) usually takes less than 20 minutes to measure the lifetime. However, as shown in Figure 3-5, the pH deviation from the physiological values occurs in only less than 10 minutes and it continues even at 90 minutes after the transportation from the incubator to the microscope. The transportation is also a source of pH deviations, since at equilibrium in the incubator the pH values were measured as 7.49 ± 0.009 and 7.19 ± 0.009 (both with n = 3) for MEM and F-12, respectively. With constant CO_2 flow rates, the pH values, within only 10 min, reached a level that was very close to the stable values, which could be controlled by varying the CO_2 flow rate. Rate = 15 was then determined to be appropriate for both the media to achieve and maintain the pH values close to those at equilibrium in the incubator.

3.6 Incorporation of both environmental controls

In this section, we incorporate both environmental controls along with further improvements. Duplicates were included in all conditions and were pooled due to statistically insignificant *p*-values in comparisons of all corresponding duplicates. The temperature was fixed at 37 ^{o}C and Citrine was used as the FRET acceptor for its relative insensitivity to physiological pH values. Two positive controls were included: Cerulean-Citrine and Cerulean-Citron + Citrine-RhoC. Citron is an effector of RhoC that binds to active RhoC to perform its function as an oncogene such as changing the motility of the inflammatory breast cancer (IBC) cells [111]. Cerulean-Citrine serves as a positive control for FRET while Cerulean-Citron + Citrine-RhoC can serve as a positive control for molecular interaction of RhoC.

With both environmental controls, again, only with the smaller variability in the lifetime values can the FRET of the experimental group be observed clearly. This is illustrated in Figure 3-6, which shows the results with CV1 cells from one of our experiments where both controls were incorporated. Although not shown in the figure, the two positive controls were included, and they, as expected, exhibited shorter lifetimes. In the upper part of Figure 3-6 (the images), we can clearly see that the lifetime values of experimental group (the left column) are smaller (redder in the images) while the other two negative controls show larger lifetime (greener). This distinction, however, cannot be observed in the intensity images with much more inter- and intra-cellular variation, obscuring any possible FRET occurring. In the lower part of Figure 3-6 (the box plots), this difference in variability can be seen again: The intensity values have much larger variability.

Only lifetime measurements with CO_2 control leads to statistically significant results without any non-specific FRET. This is demonstrated in Table 3-1, a summary of the *p*-values from the comparisons of the cells with different transfection methods. In the lifetime comparisons with CO_2 control (second column, upper half in Table 3-1), the experimental group vs. either negative control (the first and second values) has very small *p*-values (suggesting molecular interactions), while the comparison of two negative controls (the third value) gives a large *p*-value (suggesting no non-specific FRET). On the other hand, the intensity comparison, still with CO_2 control (second column, lower half), shows no statistically significant differences between the experimental group and either negative control. The third column of Table 3-1 shows the results without CO_2 control. In this case, the major problem was that non-specific FRET occurs, manifested by the statistically significant *p*-values from the comparisons of the negative controls.

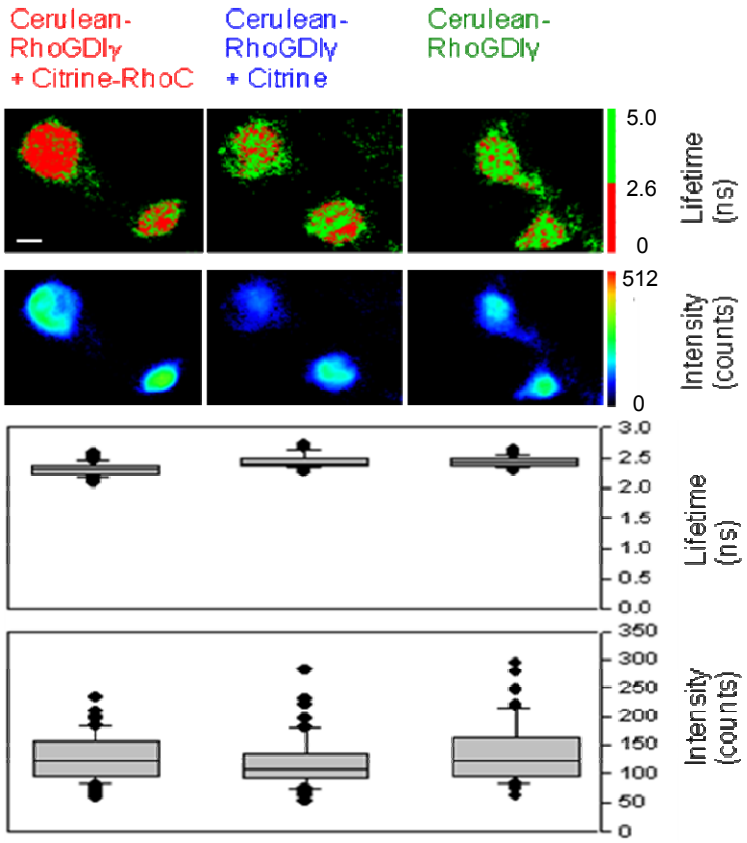

Figure 3-6 The lifetime and intensity comparisons of cells with different transfection methods. Both temperature control and CO_2 controls were incorporated. In the upper part (the images), the lifetime values of experimental group (the left column) are smaller (redder in the images) while the other two negative controls show larger lifetime (greener). This distinction, however, cannot be observed in the intensity images. In the lower part (the box plots), this difference in variability is observed again. Scale bar = 15 μm.

Table 3-1 The *p*-values from two-tailed t-tests. The temperature was fixed at 37 ^{o}C. Only lifetime measurements with CO_2 control leads to statistically significant results without any non-specific FRET. Other conditions or comparisons exhibit either non-specific FRET or statistically non-significant differences between the experimental and the control groups.

Groups in comparison	***p*-value (with CO_2)**	***p*-value (without CO_2)**
Fluorescence Lifetime		
Cerulean-RhoGDIγ + Citrine-RhoC vs. Cerulean-RhoGDIγ + Citrine	4.00E-10	3.07E-05
Cerulean-RhoGDIγ + Citrine-RhoC vs. Cerulean-RhoGDIγ	< 1.00E-10	< 1.00E-10
Cerulean-RhoGDIγ + Citrine vs. Cerulean-RhoGDIγ	0.9252	9.43E-05
Fluorescence Intensity		
Cerulean-RhoGDIγ + Citrine-RhoC vs. Cerulean-RhoGDIγ + Citrine	0.4369	8.85E-04
Cerulean-RhoGDIγ + Citrine-RhoC vs. Cerulean-RhoGDIγ	0.1894	0.8925
Cerulean-RhoGDIγ + Citrine vs. Cerulean-RhoGDIγ	5.67E-02	4.50E-03

3.7 Discussion

To evaluate the accuracy of FRET, the best index is FRET efficiency since it is the best one to characterize the degree of donor-acceptor interactions [21]. Other indices, such as sensitized emission or intensity ratios, may only work well qualitatively but not quantitatively [21]. Therefore, using donor lifetime to evaluate the accuracy of FRET is very appropriate, because donor lifetime follows a linear relationship with FRET efficiency.

In our results, fluorescence intensity data did not imply any FRET occurring between donors and acceptors [32]. In theory, FRET can be detected by either lifetime approaches or intensity approaches. However, in intensity-based FRET detection, sophisticated calibration and correction procedures are usually required to cope with intensity variation, spectral bleed-through, back-bleed-through [90], and even for photobleaching [21]. Since our intensity-based data were not acquired and processed with these procedures, the comparisons of the results of the intensity and lifetime measurements should not be regarded as comparisons of intensity-based FRET detection and lifetime-based FRET detection. Rather, the key point is that lifetime-based FRET detection is relatively simple to implement and complete, without complicated corrections, while still offering statistically significant evidence for FRET.

Our results suggested that in our system Cerulean, compared to ECFP, had greater power to statistically reveal the difference in donor lifetimes, providing stronger evidence for FRET from donors to accepters. Rizzo et al. [110] have shown that in their measurements Cerulean has higher intensity and longer lifetime than ECFP. Although the better performance of Cerulean may result from both these attributes, in our results it is more likely due to the longer lifetime, since this longer lifetime can be constantly detected in all of our measurements.

We introduced one additional negative control, Cerulean-RhoGDIγ. By comparing the donor lifetime in this additional negative control with that in the previously existing negative control (Cerulean-RhoGDIγ + EYFP), the degree of non-specific FRET can be revealed. If there is a statistically significant lifetime difference, the lifetime value in group Cerulean-RhoGDIγ will be a reference donor lifetime value for further verification to determine whether it is in a reasonable range in accord with the values in literature. This will help remove systematic errors and improve accuracy. In Section 3.3, we observed statistically insignificant difference in Cerulean fluorescence lifetimes in group Cerulean-RhoGDIγ and group Cerulean-RhoGDIγ + EYFP, when there were no environmental controls. However, as shown in Table 3-1, if temperature control was applied without CO_2 control, we observed a statistically significant difference in the donor lifetimes in these two negative controls with the acceptor Citrine instead of EYFP, and this difference was removed if both the environmental controls were applied. This implies that, in our system, incomplete environmental controls could result in unexpected systematic errors.

A possible reason for the non-specific FRET observed without the CO_2 control is the unexpected donor-acceptor association at a higher pH value. However, a closer look at our results (data not shown) indicates that the lifetime of Cerulean in Cerulean-RhoGDIγ + Citrine does not increase due to the absence of FRET when the CO_2 control is added to the system. Rather, the Cerulean lifetimes of almost all other conditions decrease due to the lowered pH values. Therefore, the possible explanation is that the Cerulean lifetimes decrease for all the conditions, while the decrease of the Cerulean lifetime in Cerulean-RhoGDIγ + Citrine is compensated for by the removal of the unexpected FRET with the CO_2 control. However, additional carefully-designed experiments must be conducted to confirm this hypothesis or provide further plausible explanations, since the

differences in Cerulean lifetimes due to pH values are relatively difficult to interpret statistically.

Furthermore, in these two negative controls, the different gene constructs used in the cell transfection may cause different transfection efficiencies and hence different intensities of FRET donors [17, 32]. As an example, in our experiment demonstrated in Figure 3-3, the intensity of Cerulean was 29.8 $\pm$ 9.7 counts in Cerulean-RhoGDIγ + EYFP but was 58.1 $\pm$ 45.4 counts in Cerulean-RhoGDIγ, and this difference is unlikely to be attributed to non-specific FRET, since the lifetime data consistently indicate no statistically significant *p*-values in the lifetime comparisons between these two groups. This demonstrates a simpler approach to determining any possible existence of non-specific FRET with fluorescence lifetimes compared to intensities.

Temperature control at 37 ^{o}C optimizes not only the transcription / translation efficiency, but also the functions and folding of fluorophores. According to our observations with Cerulean, although the enhancement of fluorescence intensity was not obvious, a higher temperature did confer Cerulean an obviously shorter lifetime, with both of our two different negative controls (both *p*-values < 1.0e-10, against null hypothesis of equal lifetimes), compared to the same conditions without any temperature controls, with culture dishes at around 25 ^{o}C, the room temperature. Lower lifetime may not be a good system parameter for accurate detection of lifetime difference, since in theory the lifetime of donor with FRET decreases proportionally to the intrinsic lifetime of donor without FRET, making the amount of decrease in lifetime smaller. However, constant environment at 37 ^{o}C should provide more consistent results.

Gas phase CO_2 concentration mainly influences the pH value of cell culture media when it is in equilibrium with ambient gas. pH value indeed has an effect on fluorescence lifetime. However, the trends, behaviors, and sensitivities of lifetime vs. pH differ with

fluorophores [112-114]. This could be presumably attributed to different relative stabilities of protonated and unprotonated excited states for different fluorophores [112]. In our system, constant flow of CO_2 into a chamber enclosing our temperature-controlled plate is achieved using a peristaltic pump with a constant flow rate. The pH value is confirmed to be stable and close to the equilibrium values in 10 minutes.

Positive controls with confirmed FRET can help verify both qualitatively and quantitatively the degree of FRET occurring in the experimental group. In our previous studies, no positive controls were used. Later, two positive controls are included along with our experimental group and the two negative controls. One of them is a linked donor-acceptor construct: Cerulean-Citrine. The other is Cerulean-Citron + Citrine-RhoC. Even shorter lifetimes of Cerulean in the positive controls, compared to those in the experimental groups, can be detected with our FLIM system, ensuring our system's capability of distinguishing different FRET efficiencies and making possible more accurate quantification of the distance between the two interacting proteins. Two positive controls also have statistically significantly different lifetime values as well (both with and without CO_2 controls), suggesting the distance between FRET donor and acceptor in cells transfected with Cerulean-Citron + Citrine-RhoC is shorter than that in cells transfected with Cerulean-Citrine. A proposed mechanism of the interaction between Citron and RhoC is required for an explanation of this phenomenon.

Temporal deconvolution (the deconvolution of signals and instrument response functions) of the fluorescence decay curves detected by our FLIM system has not been implemented and will later be incorporated in our data processing procedure for future studies. Although this definitely changes the absolute values of calculated lifetimes, it would not affect our conclusion of the detected protein-protein interactions inferred by the relative comparisons of the lifetime values.

An inspection of the stoichiometry of donors and acceptors was done with plots of the lifetime of Cerulean vs. the ratio of EYFP intensity to Cerulean intensity in Cerulean-RhoGDIγ + EYFP-RhoC double-transfected cells (data not shown). Indeed, the ratios have various values for individual cells under the same condition, probably due to non-uniformity of CFP and YFP transfection, transcription, and translation among different cells. However, no correlations have been observed in these plots so far to conclude that the donor lifetime depends on this intensity ratio. Most likely, with our experimental settings, the molar concentration of active EYFP-RhoC was always sufficient for all potentially interacting Cerulean-RhoGDIγ molecules to pair with.

Interestingly, in our fluorescence intensity comparisons, the FRET experimental groups often show higher mean values than those of the negative control CFP-RhoGDIγ + YFP, with sometimes significant *p*-values if the significance level is set to 0.1 (data not shown), contrary to what would be expected with FRET occurring from donors to acceptors. This may be due to the higher transfection efficiency of the ECFP or Cerulean vectors with weaker competitors (YFP-RhoC) in the experimental groups [32]. However, this would not affect lifetime measurements, given sufficient stoichiometry for FRET to occur, as mentioned above. In any cases, these intensity measurement results may not suggest anything relevant to FRET and are very likely due to some artificial factors that only affect intensity, since no calibrations and corrections required for intensity-based FRET detection were implemented in our approaches. Still, our simple lifetime comparison, without any complicated corrections, was able to confirm the protein-protein interactions with statistically significant *p*-values.

Chapter 4 Temporal approach – Optimal gating and curve fitting to improve the precision of FLIM

To improve the precision of the time-gated FLIM, one of the approaches we can use involves the acquisition and the fitting of the data points on fluorescence decay curves. These data points correspond to the time points through which the fluorescence decays. Therefore, we refer to this approach as a temporal approach.

The goal of this approach is to offer the first demonstration of the best gating parameters and lifetime determination methods for various needs. The results in this chapter can greatly improve the precision (relative standard deviation from 52.57% to 18.93% in one example) of time-gated FLIM for all kinds of uses such as molecular interactions, oxygen detection, and pH measurements in living cells.

4.1 Simulation results

The details of the simulation procedures can be found in Section 2.3 and the results are provided in this section.

4.1.1 RSD = f(g/τ_1, τ_2/τ_1) contour plot analysis

The significance of this section is that we confirm the consistency of our results with literature, demonstrating that our simulations are valid. We also demonstrate that MLE

and WNLLS are more precise but also more sensitive to the initial conditions of τ_1 and τ_2, when compared with NLLS.

4.1.1.1 Comparisons of RLD, MLE, NLLS, and WNLLS

We analyze the MLE, NLLS and WNLLS results in terms of RSD as a function of g/τ_1 and τ_2/τ_1 (both are set from 1 to 10 with increments of 0.5) with TC = 10^6, α_1/α_2 = 5, mc = 100, gating overlap = 50% (g/dt = 2), and n = 4, 10, and 20.

With this analysis, we can have four kinds of comparisons of the RSD values:

1. All three methods vs. RLD
2. MLE vs. NLLS
3. WNLLS vs. NLLS
4. MLE vs. WNLLS

These four comparisons are described in the following four paragraphs respectively.

All vs. RLD: First of all, our results at n (number of gates) = 4 are almost the same as the RLD results [63]. This confirms the consistency of our results with literature, since at n = 4, RLD should be able to lead to the exact results with fitting residuals = 0 (there are four unknowns only), which means as long as we are using the same fitting curve (i.e. the double-exponential decay curve), all parameter estimation algorithms should give the same, perfect match of the data to the model. In this case RSDs only reflect the errors due to different gating schemes, not errors due to different fitting methods. As the number of gates increases, generally the RSDs decrease, as we can expect. One thing worth noting is that when n increases, not only the labeled values, but also the shapes of contours change. This in turn shifts the location of minimal RSD in each graph.

MLE vs. NLLS: MLE results in smaller RSD values when comparing with NLLS. However, at n = 20, since the initial conditions (ICs) of the nonlinear optimization algorithm are not appropriate in some region, it results in errors (also see below for more details). Hence, MLE is relatively sensitive to initial conditions compared to NLLS. In our simulations, the initial conditions (τ_1, τ_2) = (0.5, 20) are used for the entire g/τ_1 and τ_2/τ_1 ranges for MLE and (15, 15) for NLLS. These conditions are determined from some preliminary trials.

WNLLS vs. NLLS: WNLLS and NLLS have similar behaviors in terms of RSD contours, with WNLLS having smaller minimal RSD (minRSD) in the entire range of interest. However, the results of WNLLS have a much stronger dependence on the input ICs of τ_1 and τ_2, which means that, if the ICs are too far away from the correct τ values, the estimated τ values from the nonlinear optimization algorithms may still stay close to their ICs, resulting in errors in those locations. Fortunately, single fixed ICs with $\tau_1 = \tau_2$ (both at 15 in our WNLLS and NLLS simulations) are sufficient to produce all minRSDs in WNLLS with various g/τ_1 and τ_2/τ_1, and very 'tolerable' (insensitive to ICs) RSD maps in NLLS with no IC errors in the range of evaluation. In the non-error regions of WNLLS RSD, the contours have the same shapes as those of NLLS RSD but the minRSDs are smaller.

MLE vs. WNLLS: Despite the IC errors of MLE and WNLLS, the comparison of MLE and WNLLS is still possible, since the region surrounding the minRSDs does not include errors. The minRSD values of these two methods are very close. This is true for the current setting. As we can see later, the distinction will appear to be significant with different α_1/α_2 and τ_2/τ_1, shown in the graphs of minRSD = f(α_1/α_2, τ_2/τ_1).

4.1.1.2 Effects of total counts (TC) on RSD values

The effects of total counts (TC) on RSD values have been investigated previously. For single-exponential decay, RSD is proved to be proportional to $1/(TC)^{1/2}$ [77], by approaches of error propagation. In cases of double-exponential decay with RLD, RSD_{f1} is still proportional to $1/(TC)^{1/2}$ [63], shown in a practical range of α_1/α_2 with Monte Carlo simulations.

Our results are consistent with the literature. All settings are the same as in the previous section except TC = 10^4 and n = 10 only. The results show that the contours previously labeled as 1 of all three approaches are roughly replaced by contours of 10 with similar shapes. This is true for all contours of less than about 20 with TC = 10^4. In these regions RSD proportional to $1/(TC)^{1/2}$ is confirmed as least for our current settings. Outside these regions, deviations occur. This is reasonable, since the behavior of RSD proportional to $1/(TC)^{1/2}$ is theoretically based on error propagation and hence depends on local linearity and infinitesimal elements. Therefore, it cannot handle large errors very precisely.

4.1.2 minRSD = f(α_1/α_2, τ_2/τ_1) analysis

4.1.2.1 Parameter ranges and color-scale vector plots

With optimal location search, we are able to find the best achievable RSDs and the gating schemes to achieve them. For all WNLLS, NLLS, and MLE approaches, the range and the increments of the parameter space adopted for searching minRSD are the same for easier comparisons. The following conditions are used since they cover most of the situations encountered with commonly used fluorophores: $\log(\alpha_1/\alpha_2)$ = -1 to 2 with increment = 0.1, τ_2/τ_1 = 1 to 20 with increment = 1, $\log(g/dt)$ = 0.1 to 1 with increment 0.1,

log(g/τ_1) = -1 to 1.4 with increment = 0.2, and n = 5, 10, 15, 20. In other words, minRSD is searched under a 10x13x4 system-parameter-space grid for each point on a 31x20 sample-parameter-space grid. With RLD, the only differences are that log(g/dt) = -1 to 1 with increment 0.2 and n is fixed at 4. This larger log(g/dt) range can perform well only in RLD since this range otherwise causes IC errors in other approaches.

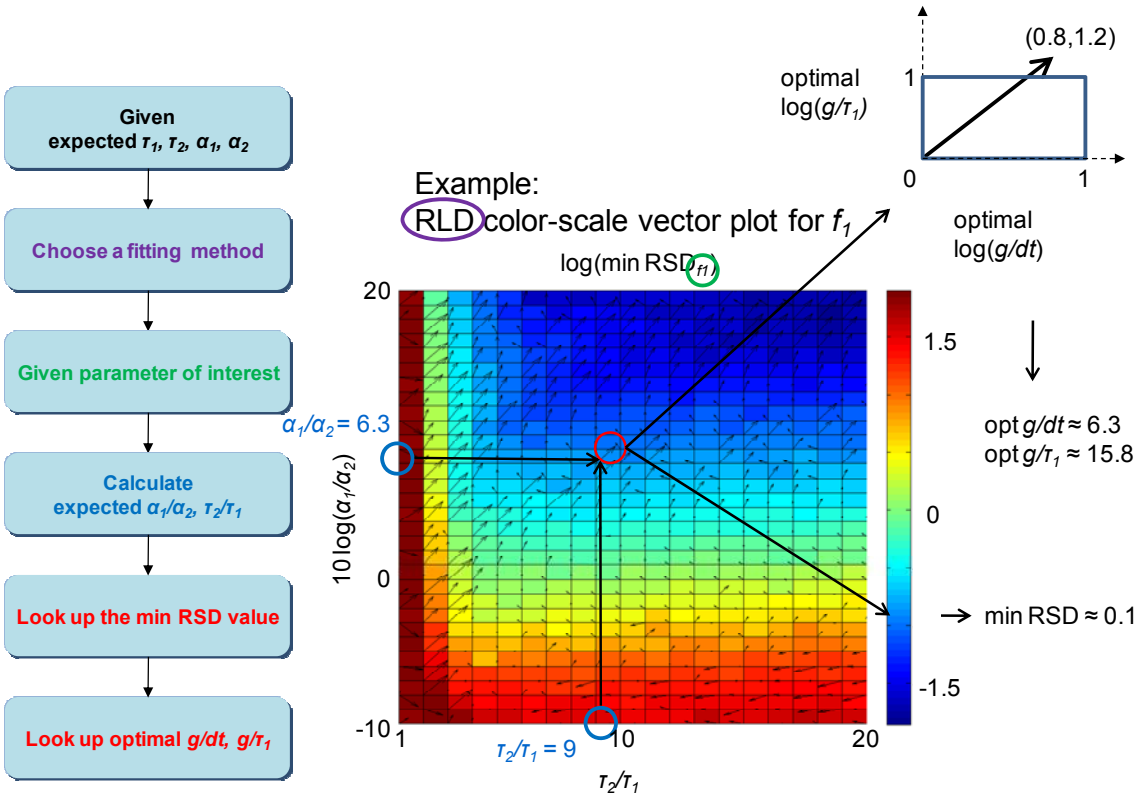

Figure 4-1 Demonstration of the procedure for using a color-scale vector plot

The data are presented as color-scale vector plots, where minimally achievable RSDs are represented by a color scale and the g and dt needed to achieve these RSDs are represented by vectors. Although the data are computationally heavy, they are easy to interpret in these plots.

Figure 4-1 demonstrates how to use the color-scale vector plots. As the first step, the expected α_1, α_2, τ_1, and τ_2 are given. These values may be obtained either from preliminary experiments or simply from previous knowledge of the sample. Then, choose

a fitting (more precisely, lifetime determination) method to use. This step can be omitted if implementing this procedure for all the methods to select the best one. Then, the parameter of interest is selected, depending on the purpose of the experiment, and the expected α_1/α_2 and τ_2/τ_1 are calculated. Figure 4-1 shows an example with α_1/α_2 = 6.3 and τ_2/τ_1 = 9. While the RLD value is looked up with the color scale, the optimal $\log(g/\tau_1)$ and $\log(g/dt)$ (hence g and dt) are indicated with rectangles scaled to one by one.

4.1.2.2 Optimal locations in the parameter space

WNLLS: Figure 4-2 shows the results of search for the optimal location (the location of minRSD) in the parameter space with WNLLS. It clearly shows that the minRSD values (the color scales) of τ_1 and f_1 have higher dependence on α_1/α_2 than the other two parameters of interest. Although at high α_1/α_2 the minRSDs of f_1 are the smallest among all the four parameters, at low α_1/α_2 they are relatively high. τ_1 has similar trend as f_1, while the minRSDs of the other two parameters have low dependence on α_1/α_2, with relatively low values through out the parameter space we searched. In addition, all four parameters show low dependence of minRSD on τ_2/τ_1. An observation of the system parameter values that confer minRSDs (the vectors) suggests that changing the system parameters according to the sample parameters indeed is required to obtain minRSDs. However, sometimes parameters, for example, optimal $\log(g/dt)_{\tau 1}$ (the x-components of the vectors), do not show clear dependence on α_1/α_2 and τ_2/τ_1. Indeed, if larger mc is used, the dependence could be resolved (described below in the part “RLD” in this section). However, the non-resolvability with lower mc can be preferred since it directly indicates weak dependence on α_1/α_2 and τ_2/τ_1, hence a higher tolerance of a fixed $\log(g/dt)_{\tau 1}$ value for various α_1/α_2 and τ_2/τ_1 values, a valuable information when choosing system parameters especially when little is known about the sample parameters. As for n (the number of gates), WNLLS requires mainly highest n (20 in our simulations) to

achieve minRSD, which is not surprising. Therefore, only n = 20 is shown in Figure 4-2, although n = 5, 10, 15 were simulated as well. The effects of n on the RSD values will be discussed later in Section 4.1.3.

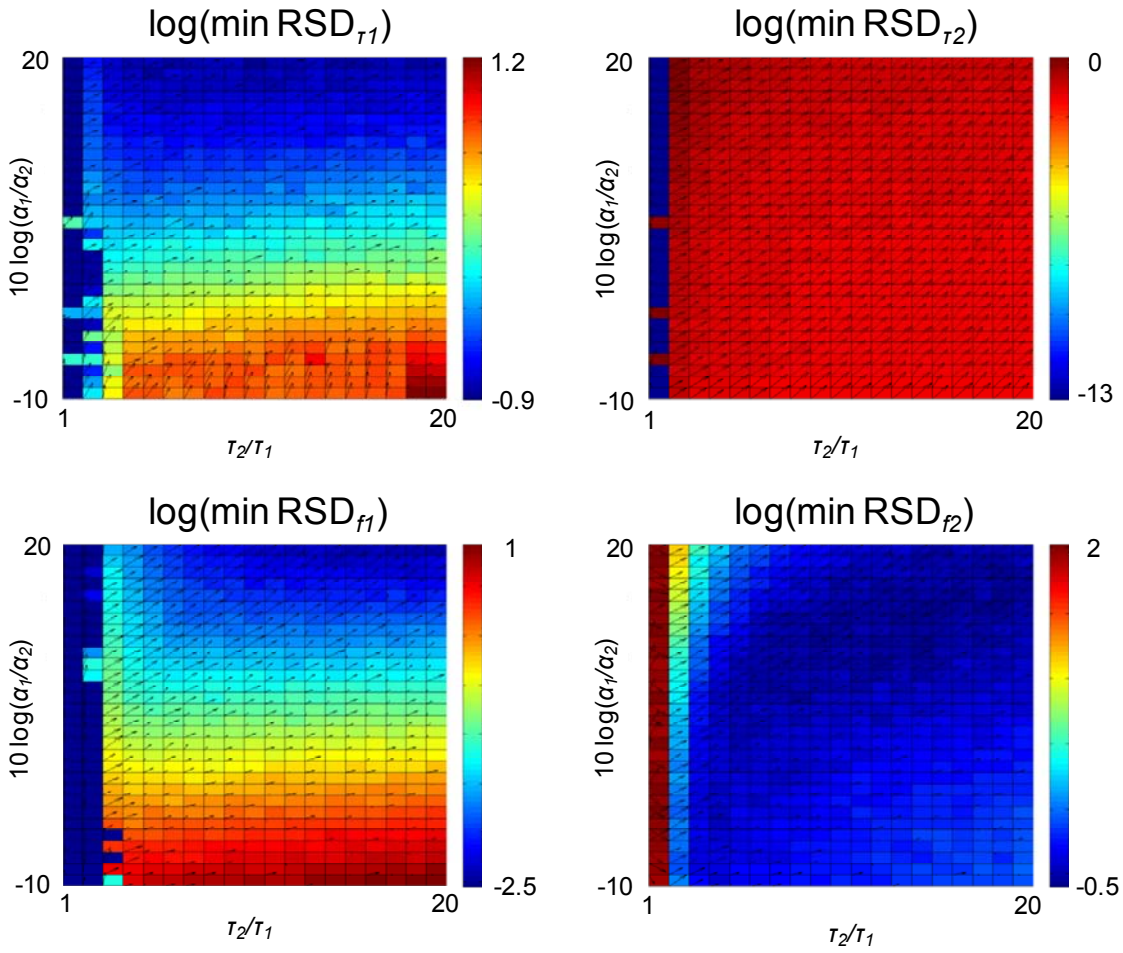

Figure 4-2 WNLLS optimal conditions represented by color-scale vector plots. Upper left: evaluated for τ_1; upper right: evaluated for τ_2; lower left: evaluated for f_1; lower right: evaluated for f_2. mc = 50; log(α_1/α_2) = -1 to 2 with increment = 0.1; τ_2/τ_1 = 1 to 20 with increment = 1; log(g/dt) = 0.1 to 1 with increment = 0.1; log(g/τ_1) = -1 to 1.4 with increment = 0.2; n = 20; TC = 10^6

NLLS: NLLS produces similar results (data not shown) to those of WNLLS but has larger minRSDs, which indicates that the IC error regions of WNLLS described previously do not affect minRSD search, and one single fixed set of IC is sufficient for all minRSDs to be achieved with WNLLS in the parameter space we adopted. Larger minRSDs with NLLS takes place mainly in the upper part of minRSD$_{\tau 1}$ and entire

$\text{minRSD}_{\tau 2}$, which is consistent with our previous RSD = f(g/τ_1, τ_2/τ_1) results. In the following analyses, we therefore will only take WNLLS into consideration when comparing with MLE and RLD.

MLE: Figure 4-3 shows the results of MLE optimal location search. Compared to the results of WNLLS, the most manifest differences are smaller minRSD_{f1} throughout the entire sample parameter range and smaller $\text{minRSD}_{\tau 1}$ in the lower left part. These improvements in minRSDs directly make the lower part of $\text{minRSD}_{\text{all}}$ (data not shown, calculated from the average of the RSDs of all the four parameters of interest) much smaller compared to that of WNLLS. Furthermore, in the same regions with smaller minRSD, we observed lower dependence of n on α_1/α_2 and τ_2/τ_1. This will be further discussed in the following section. As for log(g/dt) and log(g/τ_1), the dependencies seem to be relatively irregular, for reasons still under exploration. One possible reason could be the IC error regions covering minRSD and producing discontinuity in the corresponding optimal system parameter space, and this may imply that minRSD can be further improved by changing IC according to better initial gausses of τ_1 and τ_2.

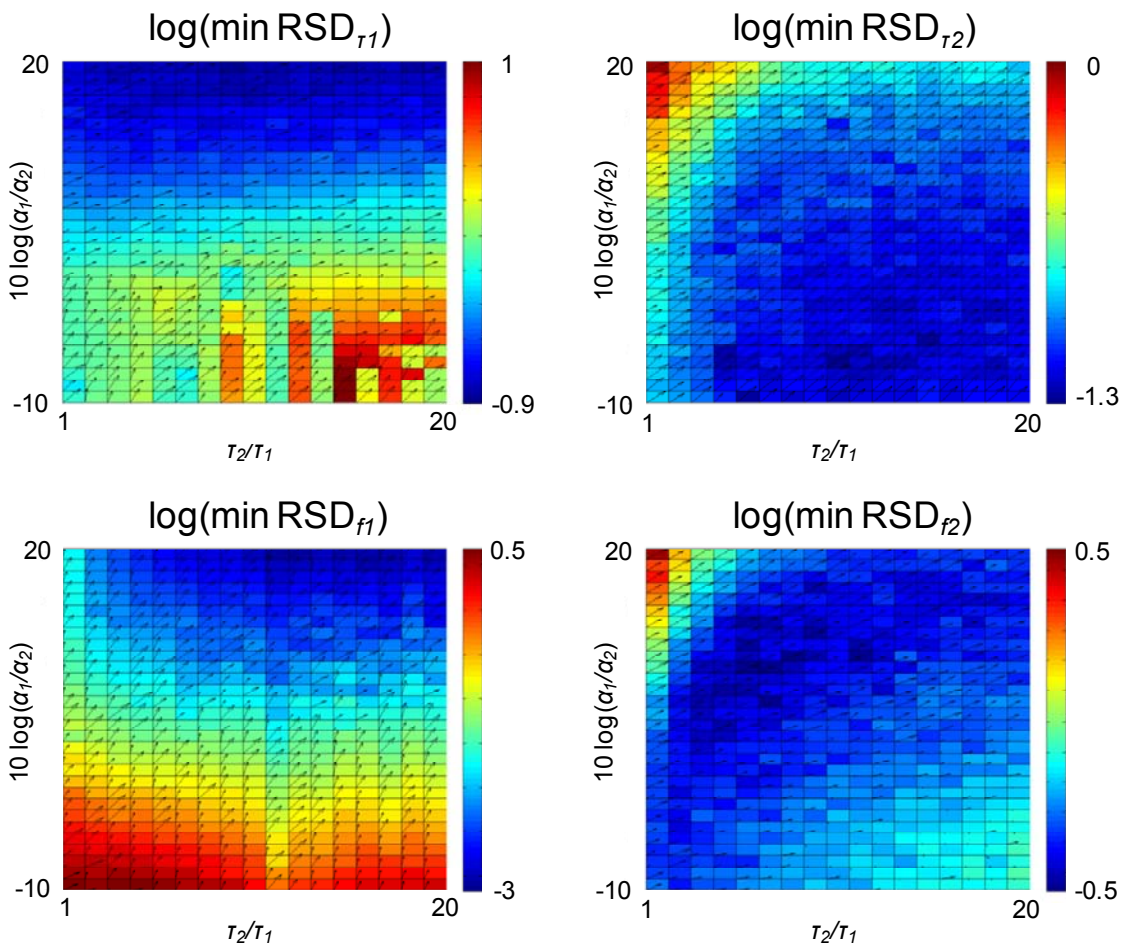

Figure 4-3 MLE optimal conditions represented by color-scale vector plots. Upper left: evaluated for τ_1; upper right: evaluated for τ_2; lower left: evaluated for f_1; lower right: evaluated for f_2. All other settings are the same as described in the caption of Figure 4-2 except τ_2/τ_1 = 3 to 20 with increment = 1 for better color scaling.

RLD (Figure 4-4): When compared to MLE, RLD has larger RSDs in all parameters, and the values can be as large as > 10 fold of the values with MLE, depending on the values of the sample parameters. However, in some cases the RSD values can already be satisfying if higher precision is not needed. In this case, RLD indeed is a preferred method due to its extremely higher speed. With higher mc (3000), the optimal *g/dt* and g/τ_1 can be highly resolved (data not shown), although this may not be preferred for the reasons described previously.

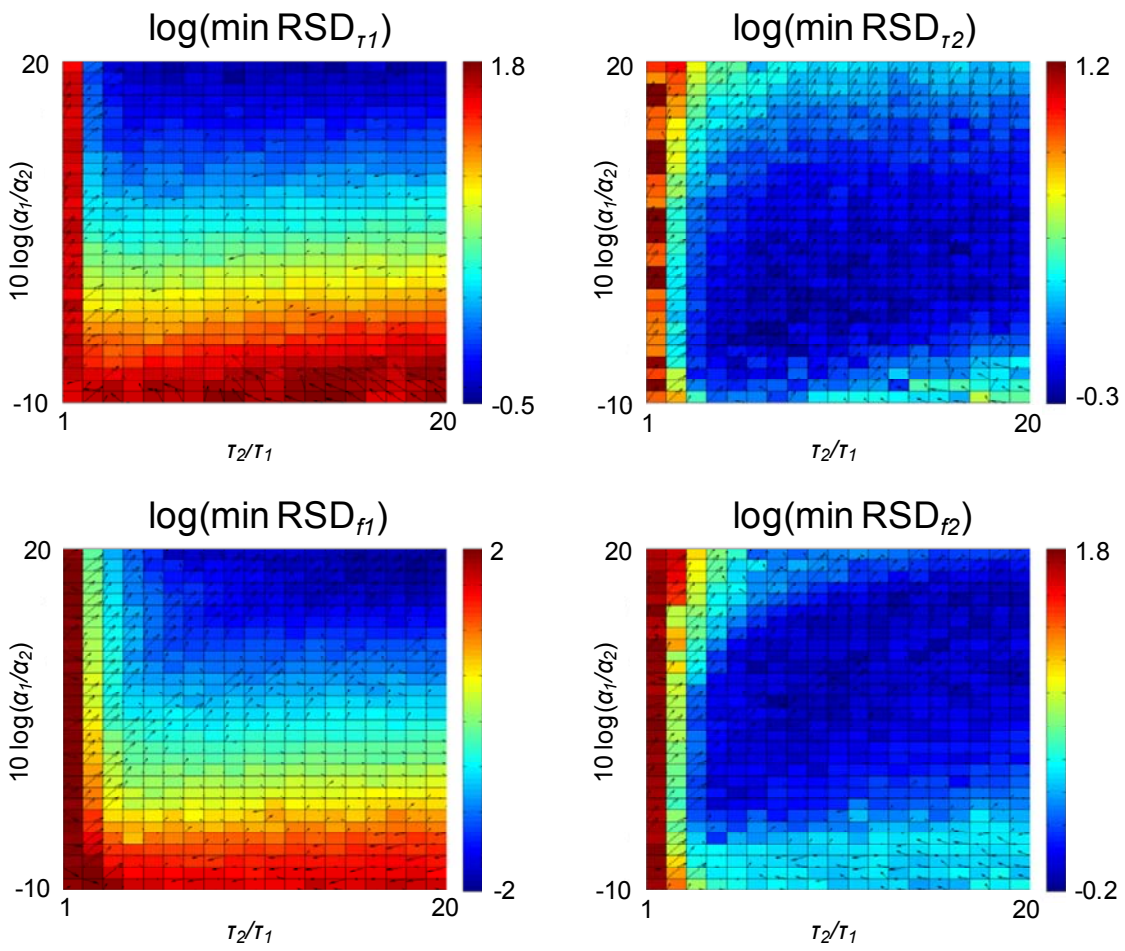

Figure 4-4 RLD optimal conditions represented by color-scale vector plots. Upper left: evaluated for τ_1; upper right: evaluated for τ_2; lower left: evaluated for f_1; lower right: evaluated for f_2. log(g/dt) = -1 to 1 with increment = 0.2; n fixed at 4. All other settings are the same as described in the caption of Figure 4-2.

In Figure 4-4, one interesting phenomenon that we can observe is the stripes in optimal g/dt and g/τ_1 (the vectors) for f_1 and f_2. A closer inspection to these stripes suggested that the "waves" of g/dt and g/τ_1 are in perfect match, which indicates that only g is changing relative to all other parameters except α_1/α_2, in the vertical direction. When α_1/α_2 increases, g needs to increase while τ_2/τ_1, TC, and dt are fixed in order to stay in the optimal conditions, which means only gate overlapping increases. Since we are assuming that τ_2 is larger than τ_1, increasing the ratio α_1/α_2 indeed needs longer gate coverage for the entire fluorescence decay range because the dimmer longer-life

component needs larger gating to be recorded relative to the more intensive shorter-life component to distinguish f_2 from f_1 and make both of these parameters determined more precisely. On the other hand, shifting in horizontal direction, for example, decreasing τ_2/τ_1 while keeping α_1/α_2 unchanged, also results in similar behavior. In this case, the signals, or the decay curve, from the longer-life component become more and more overlapped with those from the shorter-life component, again making the long-life tail more crucial for distinction. As shown in the graphs, this effect becomes critical only when τ_2/τ_1 is small enough.

To discuss the "waves" of g/dt and g/τ_1 in more details, at the base of a certain wave, g is one increment shorter than dt (or, $\log(g/dt)$ is one increment lower than 0). In our graphs, after g/dt reaches a certain value (around 10; overlapping is 90%), the wave collapses and it restarts with a larger dt and also a larger g, compared to the base of the previous wave. In fact, at this new base, g is still one increment shorter than dt, but this time g takes place of the previous dt. In other words, both g and dt increase by one increment. Now, the new gating scheme also covers the entire decay range and produces a better RSD. The collapse, in our simulations, is not due to reaching the upper bound of our g/dt or g/τ_1 values, because escalating our upper bound does not eliminate this phenomenon (data not shown). Therefore, this is an intrinsic property as long as the discretization of g/dt and g/τ_1 is fixed. If using smaller increments, the stripes will appear more frequently (data not shown) because the next available (and better) level with both increased g and dt is closer, and this in fact suggests that dt has more important role than g does in determination of optimal gating (described below). If the increments are infinitely short intervals, we actually can expect "collapse" to occur every time α_1/α_2 increases slightly, which in turn suggests that the dt, and the g that is only slightly smaller than the dt, will both need to increase slightly to meet the optimal gating

scheme. As for the effect of TC on this phenomenon, when TC is larger or smaller, we observe similar patterns (data not shown), but with smaller TC, longer gating is required to achieve minimal RSDs, which is reasonable.

4.1.3 Effects of the number of gates, *n*, on RSD values

The effects of the number of gates, *n*, are somehow related to those of the number of channels, denoted as n_0, in TCSPC (Time-Correlated Single Photon Counting) data. For single-exponential decay recorded with TCSPC, according to the error propagation analysis, it can be proved that RSD is proportional to $1/(n_0)^{1/2}$ with n_0 large enough. If double-exponential decay is the case, from our simulations (data not shown), we still approximately have RSD proportional to $1/(n_0)^{1/2}$, at least within the range of $\log(\alpha_1/\alpha_2)$ = -1 ~ 2, τ_2/τ_1 = 1 ~ 20, and n_0 = 500 ~ 4000. Now, we are interested in the effects of number of gates, *n*, on RSD. This is involved in the case when doing summations of TCSPC data to form the "gates" [63], or simply using gated integration devices such as the one in our FLIM system.

To show the effects of the number of gates on the RSDs of the four parameters of interest, τ_1, τ_2, f_1, f_2, and the average of all of them, we ran simulations with *mc* = 50, and recorded the behaviors of minRSD vs. n from MLE and WNLLS at four locations on our minRSD = f(α_1/α_2, τ_2/τ_1) graphs: ($\log(\alpha_1/\alpha_2)$, τ_2/τ_1) = (0,5), (0,10), (1,5), (1,10).

As we can expect, in most cases in our results, the RSD decreases with *n*, sometimes significantly. However, they are not proportional to $1/(n)^{1/2}$, and in some cases RSD even remains at the same level at different *n*'s. This can be partially understood by the fact, as mentioned previously, that the shape of the contours changes with increasing *n*. This in turn means that, at different locations in the RSD = f(g/τ_1, τ_2/τ_1) graphs, RSDs follow different dependences on *n*, hence not as simply as $1/(n)^{1/2}$. In

addition, here, by searching minRSD, optimal g/dt and g/τ_1 can change with increasing n at fixed locations of α_1/α_2 and τ_2/τ_1, which makes a general prediction of minRSD's dependence on n even more difficult. This is, however, of particular interest, since we wish to know the smallest n that gives acceptable RSDs, which is not necessarily the largest n available, and furthermore, the value of this n changes with different parameters of interest and different locations on minRSD = f(α_1/α_2, τ_2/τ_1) graphs.

From our results, we conclude that MLE at n = 10 is recommended in most cases. As an example, the results of MLE with the average of all parameters are shown in Figure 4-5. As we can see in the figure, the red squares and the blue diamonds (they represent different α_1/α_2, τ_2/τ_1 values) have low dependence of RSD on n. In this case, n = 5 is sufficient. On the other hand, even for the α_1/α_2, τ_2/τ_1 values that have higher dependence of RSD on n, such as the green triangles and the purple crosses in the figure, n = 10 is already good enough to produce RSD fairly close to that from higher n values.

To interpret the above results for their physical meaning, we first note that in Figure 4-5 the green triangles and the purple crosses represent the samples with a greater α_1/α_2 value, 10. Therefore, in this case, if the samples to be tested have a larger difference in the relative abundances of the two fluorescent components, the precision depends more on the number of gates, n. Furthermore, as we can also see in Figure 4-5, the purple crosses have the greatest dependence of the precision on n, representing the location in the sample parameter space with a larger difference in the relative lifetime values (τ_2/τ_1 = 10) of the two fluorescent components. All the above appears to be reasonable, since greater α_1/α_2 or τ_2/τ_1 values make one of the two components more difficult to detect, or make it appear predominantly only in the beginning or at the end of

the decay curves. Therefore, this situation requires a higher number of gates for better precision in the determination of the lifetime values and the relative amounts.

The results for individual parameters of interest (f_1, f_2, τ_1, and τ_2) are as follows (data not shown). If f_1 is our target parameter, MLE with n = 5 will be our choice, because of the insensitivity of RSD_{f1} to n with MLE, and the smaller RSDs from MLE at all locations and numbers of gates than those from WNLLS. In the case of f_2 with MLE, we can observe a huge dependence on n only before n = 10. Therefore, MLE at n = 10 could be our choice. As for τ_1 and τ_2, generally, in MLE, the RSD has weak dependence after n = 10 for most cases, and in WNLLS, the RSD is usually greater than or similar to that from MLE although the dependence appears to be stronger. Therefore, MLE at n = 10 is still good.

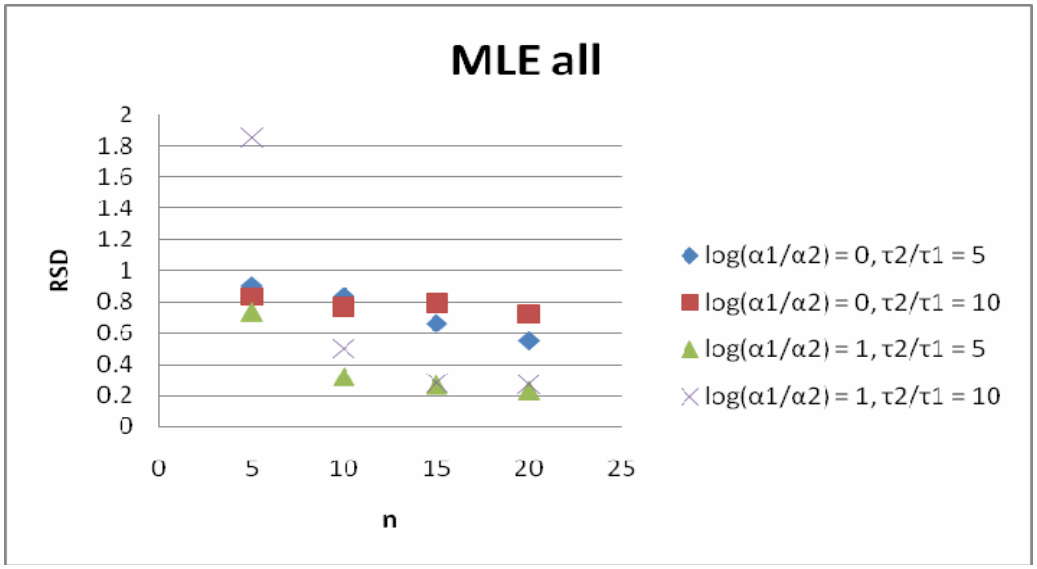

Figure 4-5 minRSD vs. n plots for MLE (under optimal conditions) with n = 5, 10, 15, and 20. Four locations on the minRSD = f(α_1/α_2, τ_2/τ_1) graphs are taken for this analysis: (log(α_1/α_2), τ_2/τ_1) = (0,5), (0,10), (1,5), (1,10). Refer to the caption of Figure 4-2 for other setting.

4.1.4 *dt* has higher impact on RSD than *g*

As mentioned in the later portion of Seciton 4.1.2.2, our results suggest that dt usually has greater effect on RSD than g (hence the gate overlapping) does. This

discovery is novel. In single-exponential-decay cases, to our best knowledge, this phenomenon has not been reported explicitly, although it might be implied in previously reported RSD plots [67, 70, 76, 77]. Even so, it is very likely that this effect is especially important for double-exponential-decay cases, since a distorted exponential decay curve consisting of two components with very different lifetimes should rely more on capturing an entire curve with a suitable *dt* than with the gate width *g* for better lifetime determination. The phenomenon described here has not been reported previously for double-exponential decay, to the best of our knowledge.

Figure 4-6 and Figure 4-7 reveal this phenomenon. As examples, we looked up the f_2 optimal schemes for $\alpha_1/\alpha_2 = 5$ and $\tau_2/\tau_1 = 7.5$, for RLD and MLE ($n = 10$) with $mc = 100$. WNLLS shows very similar trends to those of MLE. Under the above settings, we have optimal schemes: $g = 4.0\tau_1$ and $dt = 1.3\tau_1$ for MLE; $g = 6.3\tau_1$ and $dt = 2.5\tau_1$ for RLD. Here, we selected a fixed gating scheme for both methods that is close to, but not exactly equal to, the optimal schemes for the two methods, such that comparisons between them are easier. The selected scheme is $g = 6.0\tau_1$ and $dt = 2.0\tau_1$, and in the figure this scheme is the reference scheme, indicated as 100%*g* and 100%*dt*. The blue curves show the RSD_{f2} values changing with *dt* as the percentage of the reference $dt = 2.0\tau_1$, while the red curves show the RSD_{f2} values changing with g as the percentage of the reference $g = 6.0\tau_1$. Clearly, relative change of *dt* has a much greater effect on RSD_{f2}. Therefore, the choice of *dt* is particularly important. Also, it can be observed in the figure that although our fixed scheme $g = 6.0\tau_1$ and $dt = 2.0\tau_1$ is closer to the optimal RLD gating scheme than to the optimal MLE gating scheme, the RSD_{f2} of RLD at this reference point appears to be obviously larger than that at *dt* = 150% reference *dt* (optimal *dt* should be around 125% reference *dt*, as can be calculated from above). This is not observed in MLE. In addition, changing of RSD_{f2} with varying *dt* is more dramatic

compared to MLE, especially with smaller *dt*. These phenomena can be understood by realizing that only four gates are used in RLD, making the RSD much more sensitive to *dt*.

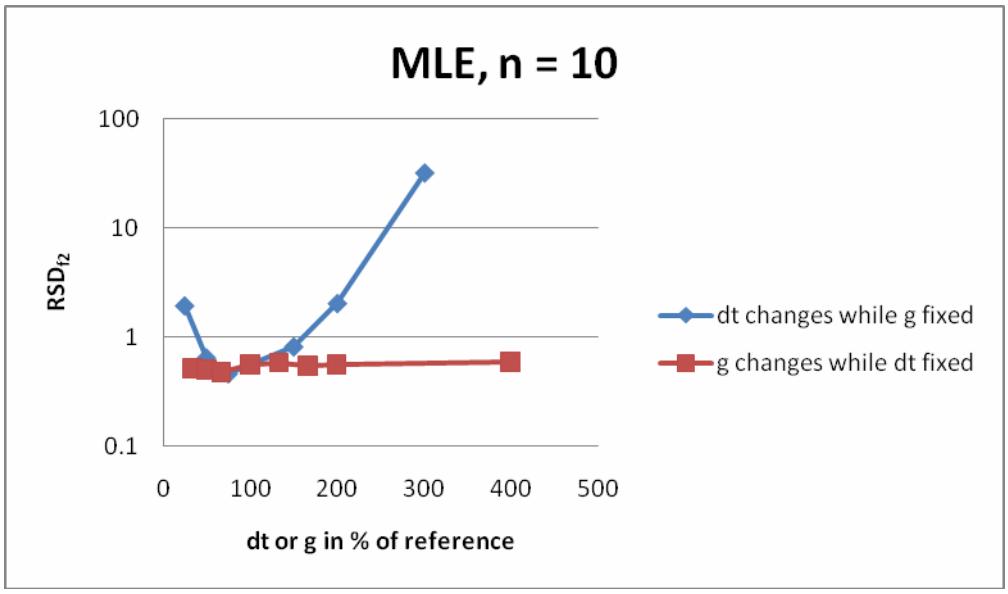

Figure 4-6 RSD_{f2} vs. *dt* and *g* in percentage of reference values ($dt = 2.0\tau_1$ and $g = 6.0\tau_1$), showing effects of changing *dt* and *g* on RSD, for MLE (*n*=10). $\alpha_1/\alpha_2 = 5$; $\tau_2/\tau_1 = 7.5$; *mc* = 100; TC = 10^6.

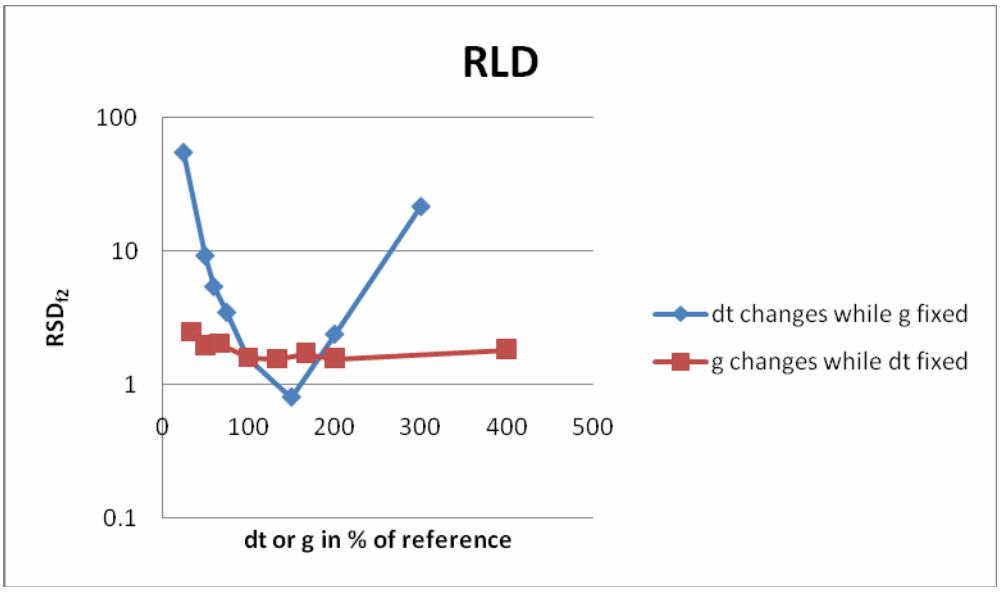

Figure 4-7 RSD_{f2} vs. *dt* and *g* in percentage of reference values ($dt = 2.0\tau_1$ and $g = 6.0\tau_1$), showing effects of changing *dt* and *g* on RSD, for RLD. $\alpha_1/\alpha_2 = 5$; $\tau_2/\tau_1 = 7.5$; *mc* = 100; TC = 10^6.

4.1.5 Analysis of relative mean errors (RMEs)

In all situations mentioned above, the relative mean errors (RMEs) of all the parameters of interest are inspected to ensure that the mean values in our simulations are close to the corresponding values we used to generate the noise-free decay curves (the "correct" values). RME is defined as [(the mean value over all simulations - the correct value) / the correct values] x 100%. In some regions of our RSD = f(g/τ_1, τ_2/τ_1) graphs, RMEs do have large values. This happens in all approaches, including RLD. Yet almost all large RMEs take place in regions where τ_1 is very close to τ_2, indicating that single-exponential decay should be used instead. This also explains the discontinuous edges at low τ_2/τ_1 in the color-scale vector plots shown in Section 4.1.2.2. For WNLLS, in the corners where the IC error occurs, we also observe large RMEs, as expected. Nevertheless, the deviation of mean values never takes place in the regions close to our optimal locations of the parameter space, where minRSD occurs, unless τ_2/τ_1 is close to one.

4.1.6 A guideline for the practical use of the temporal approach

In this section, we provide a step-by-step procedure for the practical use of the temporal approach. First, we need to choose a lifetime determination method and a region of the parameter space to use. This can be done by answering the questions in the following five steps:

- Are approximate values of τ_1, τ_2, α_1, α_2 known?
  - No: Use RLD first (with arbitrary gating) to obtain approximate values of τ_1, τ_2, α_1, α_2 and then any of the lifetime determination methods can be used
  - Yes: All the lifetime determination methods can be used

- Is real-time imaging needed?
  - No: All the lifetime determination methods can be used
  - Yes: Use RLD unless nonlinear fitting can be performed fast enough
- Is determination of more than one of the four parameters τ_1, τ_2, α_1, α_2 needed?
  - No: Use the graphs of RSD for the parameter of interest
  - Yes: Check each of the following and find the best one for the sample
    - Check all the lifetime determination methods to see if similar "vectors" can be used for all parameters of interest
    - Check all the lifetime determination methods to see if changes of "*g*" can form similar "vectors" to use for all parameters of interest
    - Perform one lifetime determination procedure at a time with optimal gating for each of the parameters of interest, and then do it multiple times for all of them
- Are there multiple distributions of τ_1, τ_2, α_1, α_2 in the sample?
  - No: Use the point (τ_2/τ_1, α_1/α_2)
  - Yes: Find regions with similar "vectors" or change "*g*" to include the possible values of τ_1, τ_2, α_1, α_2

Once the potentially applicable lifetime determination methods and regions of the parameter space are determined, the following should be done:

- Check all suitable methods / regions and choose the one with the best precision
  - Look up the optimal gating and use it
- If WNLLS or MLE is chosen, use the smallest *n* (number of gates) needed

Alternatively, if applicable, MLE with n = 10 can be a recommended method in most cases:

- If all methods are suitable, MLE with n = 10 is suggested
  - In most cases, MLE has the best precision among all the lifetime determination methods, and MLE with n = 10 is usually as good as MLE with higher n

4.2 Experimental validation

4.2.1 Double-exponential-decay lifetime standards

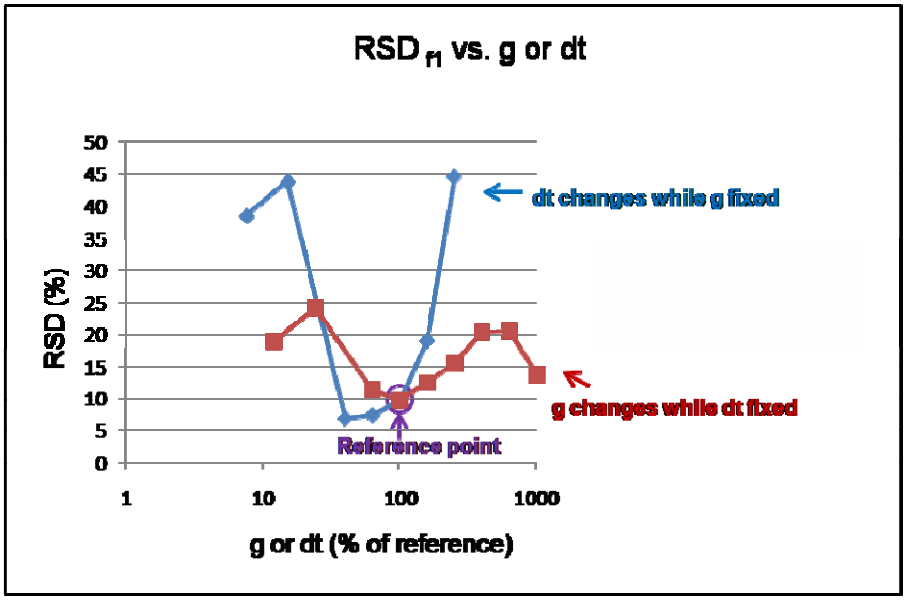

Figure 4-8 Experimental validation of RSD_{f1} vs. dt and g in percentage of the reference values (dt = 6.57 ns; g = 4.14 ns), showing effects of changing dt and g on RSD, for RLD. α_1/α_2 = 5; τ_2/τ_1 = 6.66; TC = 10^3.

Figure 4-8 demonstrates, as an example, an experimental validation of the effects of changing dt and g on the RSD values of RLD. This experiment was conducted with two single-exponential lifetime standards PPO (2,5-diphenyloxazole) and 9-cyanoanthracene dissolved in methanol [115]. The lifetimes and intensities of both standards were

carefully measured to calculate the relative α values with our optical system. The lifetime value of PPO was measured as 1.66 ns while that of 9-cyanoanthracene was measured as 11.06 ns. The lifetime value of 9-cyanoanthracene is lower than the value in the literature probably due to the lack of degassing. PPO then serves as the component 1 (shorter-life component) while 9-cyanoanthracene serves as the component 2 (longer-life component) in a mixture of both. A mixture with $\alpha_1/\alpha_2 = 5$ and TC = 1000 was made, with fixed $\tau_2/\tau_1 = 6.66$. Since the RLD optimal gating was searched under increments of $\tau_2/\tau_1 = 1$, the optimal gating scheme for $\alpha_1/\alpha_2 = 5$ and $\tau_2/\tau_1 = 7$ was then used: optimal g = 4.14 ns and optimal dt = 6.57 ns. Direct comparisons of Figure 4-7 (the RLD part) and Figure 4-8 may not be appropriate due to the differences in their parameters. However the overall trend is similar, confirming the concept that dt has greater impact on RSD, even with different parameters. Also note that the minimal RSD values are around 100% of the reference g and dt, which is expected, although smaller g appears to work better perhaps due to the actually smaller τ_2/τ_1 value than 7.

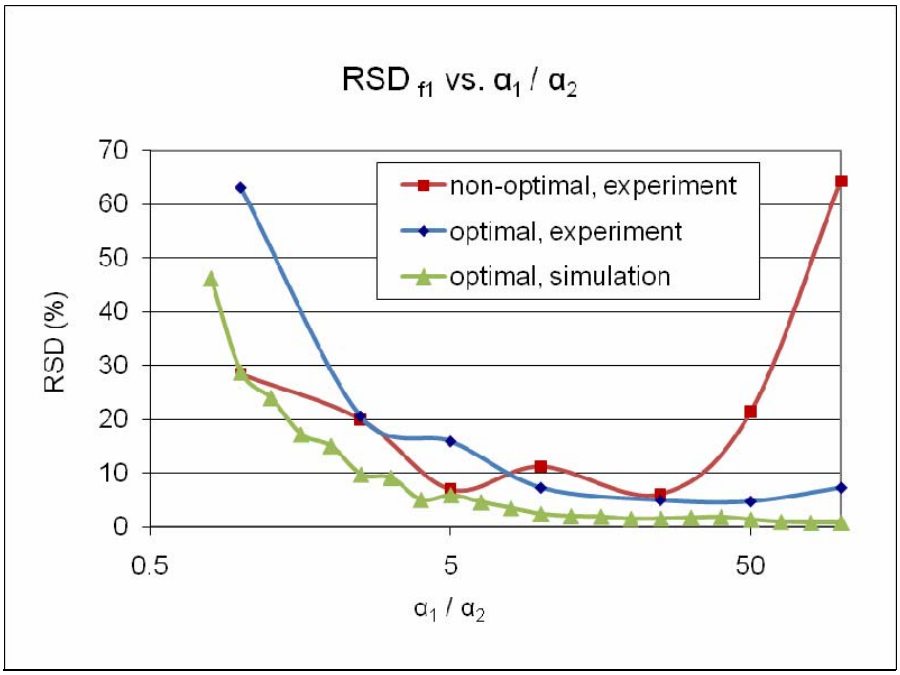

Figure 4-9 Experimental validation. RSD_{f1} vs. α_1/α_2, for RLD. The optimal gating schemes for τ_2/τ_1 = 7 were used in experiments for a mixture with τ_2/τ_1 = 6.66 (the blue curve). The non-optimal condition is $g = dt$ = 2.615 ns in experiments for the same mixture (the red curve). The simulation results with optimal gating for τ_2/τ_1 = 7 are also shown (the green curve). TC = 10^3 in all cases. The matching trends of the blue and green curves confirmed that our simulation is valid. The right end of the non-optimal red curve has dramatically increased RSD compared to the optimal cases, and the left end of it is lower than the experimental optimal curve, due to inaccurate mean f_1 values obtained with this non-optimal gating.

We validated one vertical line in the RLD color-scale vector plot for f_1 (as in Figure 4-1 and Figure 4-4) with various α_1/α_2 values, with the same lifetime standards mentioned above and the fixed τ_2/τ_1 value. Figure 4-9 demonstrates the results of this experimental validation. Still, the optimal gating schemes for τ_2/τ_1 = 7 are used, while the sample τ_2/τ_1 = 6.66. Clearly, the curve from the experimental results (the blue curve) has the same trend as the curve obtained from our simulations (the green curve), and it is reasonable to have higher values of RSD with the experimental curve since it inevitably includes other forms of noise and variation that are not included in the simulations, which only take Poisson noise into account. The matching trends of these two curves confirmed that our simulation is valid. In addition, the differences between these two curves help us evaluate and quantify the effects of other variations unexplained by

Poisson noise on the RSD. The red curve in Figure 4-9 was obtained with a non-optimal gating scheme but the same lifetime standard mixture. The right end of this curve has dramatically increased RSD compared to the optimal cases. However, the left end of it is lower than the experimental optimal curve, and this is in fact due to inaccurate mean f_1 values obtained with this non-optimal gating. This happens when the signal falls out of the detector linear dynamic range. Therefore, with this non-optimal gating, the mean f_1 values are much larger than the expected and correct values, causing RSD to drop.

4.2.2 Single-exponential-decay fluorescent beads

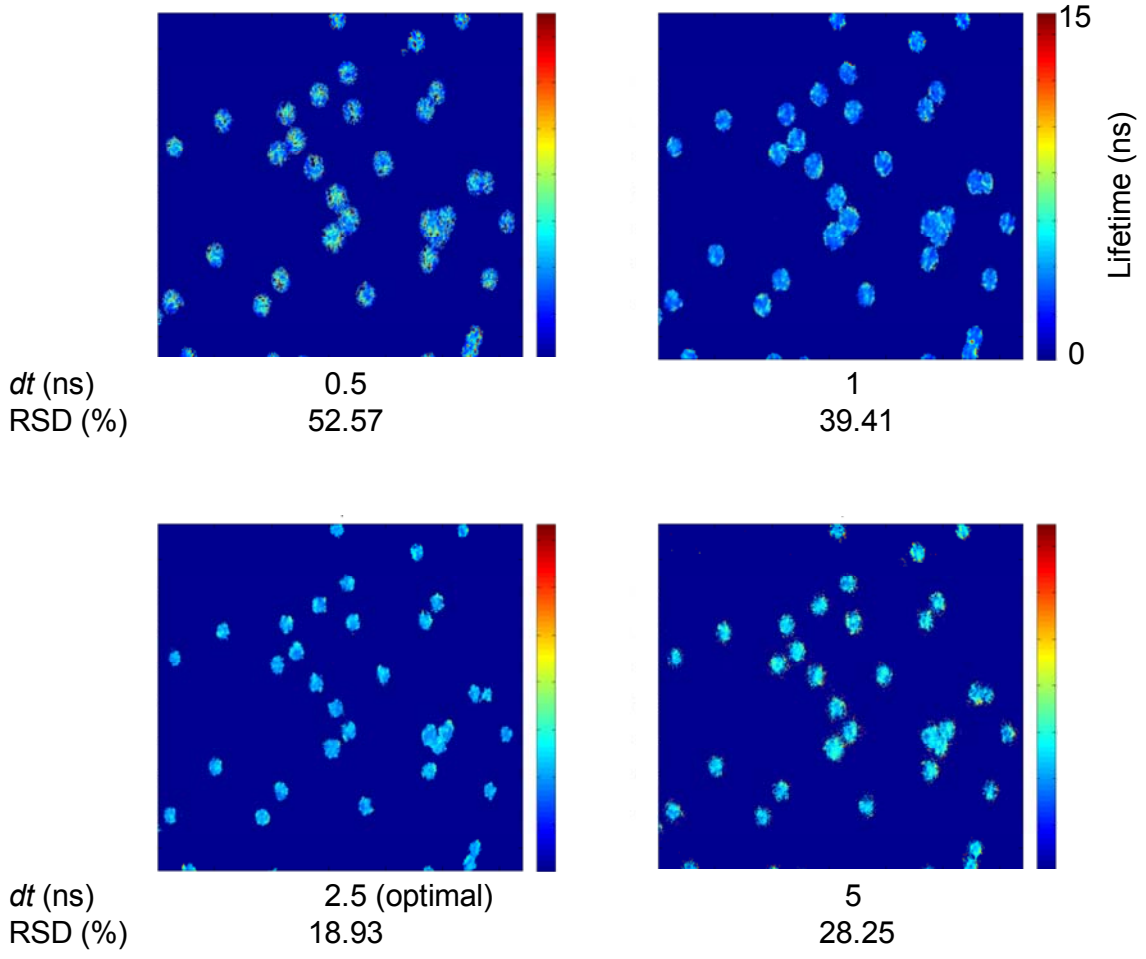

Figure 4-10 Images illustrating RSD dependence on *dt*, with *g* fixed at 10 ns. The RSD values are calculated from all non-zero pixels in the images. The total photon counts (TC) is around 100.

To experimentally validate the temporal method in FLIM images, single-exponential-decay fluorescent beads with diameters of 10 μm (Fluoresbrite® YG Microspheres 10.0μm, Polysciences, Warrington, PA) are used due to their similar sizes to those of living cells and their appropriate optical properties. They were suspended in distilled water to produce a solution with a final concentration of $1.5x10^6$ beads/mL. Before imaging, 200 μL of the solution was placed on a delta T dish (Bioptechs, Butler, PA), and imaging was begun after the beads had settled to the bottom of the dish. All beads had excitation/emission maxima of 441/486 nm, as specified by the manufacturer. A 40 x objective was used in the FLIM system.

The analysis of optimal gating with single-exponential decay can be easily performed with the same concepts as mentioned previously but with much simpler procedures. The four-gate protocol is used. In this case, according to our calculations (data not shown), minimal RSD could be achieved around *dt* = 2.5 ns and *g* = 10 ns.

Our experimental results agree with the simulation results. Figure 4-10 illustrates these results of the fluorescent beads. Note that this is an extremely low-light case with total photon counts only around 100. The lifetime of the fluorescent beads is ≈ 4.75 ns. As can be observed in the figure, the variability of lifetime values in the images, and the corresponding RSD value, is indeed smaller when the gating is optimal, while both the variability and the RSD value become larger with either increasing or decreasing *dt* from the optimal value. The variability of lifetime values at the optimal gating can be further reduced with our spatial (image denoising) approach, as will be demonstrated in later chapters.

We also validated the rule of RSD $\propto 1/(TC)^{1/2}$ in this experiment with a higher excitation intensity. Still with optimal gating (*dt* = 2.5 ns, *g* = 10 ns) but with a TC value around 600, the RSD value = 7.58 was obtained. Hence this rule roughly holds.

4.3 Summary and conclusion

Several approaches to double-exponential fluorescence / luminescence lifetime determination have been investigated with Poisson-distributed noise assumed to be the source of data disturbance. The relative standard deviation, serving as an indicator of the precision, has been acquired via Monte Carlo simulations.

The RSD = f(g/τ_1, τ_2/τ_1) analysis suggest that NLLS, while appearing to be the most tolerable (insensitive to the initial conditions, ICs, of τ_1 and τ_2) in the parameter range of interest, does not produce the best precision. On the other hand, while WNLLS and MLE have intolerable areas with a single set of fixed ICs, they produce smaller minRSD. This suggests that WNLLS and MLE are needed for higher precision, while NLLS and RLD are better used when little is known about the sample parameters. Also, all the three nonlinear fitting methods have their n = 4 results consistent with the RLD results. In addition, our RSD = f(g/τ_1, τ_2/τ_1) results also reveal the dependence of RSD on total photon counts (TC), mainly RSD $\propto$ $1/(TC)^{1/2}$, at least for relatively low RSD values, and lower TC makes IC errors occur more often (the estimated τ values stay close to their ICs, resulting in errors in those locations).

With our optimal condition search (minRSD = f(α_1/α_2, τ_2/τ_1) analysis) with WNLLS, MLE, and RLD, in our searched parameter regions, minRSDs of τ_1 and f_1 have higher dependency on α_1/α_2, while minRSDs of all the four parameters of interest have relatively low dependence on τ_2/τ_1. For WNLLS, the IC error regions do not affect our minRSD search. Among all the methods, MLE has the best precision, and with MLE in some parameter regions, low dependence of optimal n on α_1/α_2 and τ_2/τ_1 is observed.

Our minRSD vs. n graphs, evaluated with n = 5, 10, 15, and 20 at ($\log(\alpha_1/\alpha_2)$, τ_2/τ_1) = (0,5), (0,10), (1,5), (1,10), suggest that MLE at n = 10 in most cases (except for f_1, for

which n = 5 could be used) appears to be a good choice to achieve minRSD values that are quite close to that from MLE with n = 20 and are smaller than that from WNLLS.

The analysis on RSD_{f2} vs. dt and g in percentage of the reference values, showing effects of changing dt and g on RSD, clearly indicates that relative change of dt has a much greater impact on RSD_{f2} than g does, and this effect is strongest in RLD.

The RME analysis shows that in some regions of our RSD = f(g/τ_1, τ_2/τ_1) graphs, the deviation of the mean values does occur, mainly in the regions where τ_1 is very close to τ_2, or in the corners where IC error occurs. However, it rarely takes place in the regions close to our optimal locations of the parameter space, therefore providing proofs of accuracy of our optimal gating schemes.

Chapter 5 Spatial approach – Total variation (TV) models for FLIM image denoising

In addition to the temporal method mentioned in Chapter 4, another way to improve the precision of FLIM takes advantages of the fact that the time-gated FLIM, as a microscopy technique, produces images for each gating. Therefore, to reduce the perturbation to live cells while enhancing the precision, the spatial information in gated images can be used to remove the noise in lifetime determinations in low-light FLIM.

The goal in this chapter is to develop, for the first time, accurate image processing algorithms that can enhance the precision of time-gated FLIM, and to demonstrate a novel technique to simultaneously remove various kinds of noise in a real imaging system including Poisson noise, readout noise, and extra noise. The results in this chapter can, like the temporal approach, improve the precision of time-gated FLIM in all kinds of quantitative applications in living cells. As an example, notable improvements can be achieved in the mean R^2 (from 0.8960 to 0.9508) and χ^2 (from 0.8956 to 0.3559) values, and hence, in the precision associated with local lifetime determination. In addition, the noise characterization technique may be applied to imaging systems other than FLIM and may further improve deconvolution techniques for better image resolution.

5.1 Results of the artificial images, the first version

The purpose of this section is to identify suitable total variation denoising models for time-gated FLIM, by evaluating their precision and accuracy using relative standard deviation (RSD) and relative mean error (RME), respectively, with the predetermined parameters of the artificial images.

The details of the analytical procedures can be found in Section 2.4.

5.1.1 Undenoised images

The MC results using the undenoised images indicate the RSD and RME values that will serve as a basis for later comparisons with those values after denoising.

After running 100 MC simulations, RMEs are centered about zero because of random nature. However, the satellite has much higher RSD values. This is due to the "total count (TC) effect" [63, 77], which can be easily derived by error propagation from the integrated intensity to the calculated lifetime [67, 71, 77]. This effect can be summarized as: "If the nonlinearity of RSD is sufficiently low, RSD is approximately inversely proportional to the square root of total count, given that other conditions stay unchanged." Total count can be calculated as $\alpha_1\tau_1$, which is exactly the total area under the (single) exponential decay curve. In our images, we have TC = 10000 in the inner circle, 9000 in the ring, and 1000 in the satellite.

Let us take a look at Table 5-1, which shows the average RSD and RME in the three locations. The data are obtained from duplicates. Clearly, the RSD of the satellite is much larger than that of inner circle and the ring, and indeed it is about square-root-of-ten-fold of the other two. The reason why RSD of the ring is lower than that of the inner circle is actually another issue. Briefly, the gating scheme used here is actually closer to

the optimal scheme for τ = 9 rather than τ = 10. In fact every τ has an optimal gating scheme and the gating scheme used here, according to some previous calculations, is quite close to the optimal scheme for τ = 3 ~ 13. RMEs, on the other hand, are fairly random as shown in Table 5-1. This becomes even clearer if more MC simulations are run (data not shown).

Table 5-1 The average RSD and RME in the undenoised images (duplicates)

	RSD	RME	RSD	RME
The inner circle	1.8193	0.0278	1.8238	0.0220
The ring	1.7744	0.0123	1.7979	0.0063
The satellite	5.8502	0.0352	5.7603	-0.0342

Our goal of this chapter is fairly simple. We wish to lower RSD, by using denoising procedures, while still keeping RME as close to zero as possible, at least in a reasonable range around zero, or comparable to the values of undenoised case.

5.1.2 Rudin-Osher-Fatemi (ROF) model

As introduced in Section 2.4, the ROF model is a very commonly used TV denoising model. A modified version of the ROF model - the constrained ROF model, is used in this section so that the discrepancy rule [84] can be evaluated automatically in the denoising process. Of course, in this case, discrepancy rule is evaluated under L^2 norms (see Equation (2-8)), which may not be suitable for images with Poisson noise.

The results of ROF denoising are shown in the following table. The conditions used are: *nt* = 1500 (the number of time steps), *delt* = 1/*m'n'* (the time interval used in denoising) and *mc* = 100 (the number of Monte Carlo simulations).

ROF denoising preserves the objects and the edges in the images. Under the given setting, the ring and the satellite (and their edges) still remain in the denoised images without being eliminated and treated as noise.

However, ROF denoising makes lifetime determination inaccurate. Table 5-2 shows the average values of RSD and RME in all locations after *mc* = 100 simulations. As we expected, ROF model, removing noise by decreasing total variation, does make RSDs smaller, especially for the inner circle and the satellite, compared to those values from undenoised simulations. However, obviously this approach makes lifetime determination inaccurate, since we now have mainly negative RMEs and RME_{sate} (RME of satellite) is as low as -6.24.

Table 5-2 The average RSD and RME in the ROF-denoised images

	RSD	RME
The inner circle	0.9329	-0.4638
The ring	1.6961	-0.4509
The satellite	3.3470	-6.2445

The inaccuracy of ROF denoising arises from the non-proportionality of the intensity and the intensity decrease due to denoising. If we take a look at the denoised images separately, we find that all the gates mainly have lowered intensity values compared to their true intensity values. Although earlier gates, which have greater intensities, do have greater decrease, these decreases are not in proportion to their intensities.

5.1.3 Poisson-adapted TV (PoissTV) model

5.1.3.1 Energy, gradient descent, and J(*u*)

A TV model developed by Le, Chartrand, and Asaki was designed to deal with images corrupted by Poisson-distributed noise [84]. This model is denoted as "PoissTV" here. Before this model was developed, there were also other models designed to address the issue of non-uniformly distributed (or spatially variant) magnitude of noise over the image. However, the model provided by Le, Chartrand, and Asaki is relatively intuitive and has the ability to adapt to the magnitude of noise automatically without any pre-determination of model parameters before denoising. The energy of this TV model is

$$E = \int |\nabla u| + \lambda \int (u - f \log u) dx \tag{5-1}$$

The energy of this Poisson-adapted model is defined such that the *u* that leads to minimal *E* has maximal probability with Poisson distribution around the value of *f*. This is similar conceptually to the principle of the MLE described in the temporal method.

The gradient descent can be derived as

$$u_t = \nabla \cdot \left(\frac{\nabla u}{|\nabla u|} \right) + \lambda \frac{f - u}{u} \tag{5-2}$$

To implement this model is fairly simple since the only difference between the PoissTV model and the ROF model is the *u* in the denominator in the fidelity part of the gradient descent here (see Equation (2-9), where 2*λ* can be regarded as a single coefficient).

To apply the discrepancy rule, J(*u*) is defined as [84]

$$J(u) = \int u - f \log(u)$$

(5-3)

where *f* is the given image and *u* here can be replaced by any image such as *f* and *o* (the original image without noise). J(*u*) is used to find the *λ* value (or the *fid* value) to use according to the discrepancy rule, which, in this model, requires J(*o*) = J(*u*) where *o* is the original image without noise and *u* is the denoised image.

In practical use, some modifications of the model are required. Since the artificial images contain some pixels with zero intensity, a variable called "*pme*" is included in the code to be added to the entire image set. At first, *pme* was kept small, as 0.00001, since the original purpose to include *pme* is to avoid division by zero. However, it turns out that if *pme* is too small, it cannot prevent the intensities of the background pixels from becoming negative. PoissTV cannot properly handle negative intensities. Specifically, in the denoising process, if *f* has small and positive values and *u* at the same location has slightly larger value (which arises from the divergence term in the gradient descent), then, after the next time step (if *fid* is sufficiently large) the fidelity part of the gradient descent (*f*-*u*)/*u* will make u negative. Once *u* becomes negative, it becomes more and more negative due to (*f*-*u*)/*u*. This causes serious problems. Therefore, the variable "*pme*" was later kept at a higher value, 5.

5.1.3.2 Results

The discrepancy rule requires that J(*o*) = J(*u*). If original images without noise are used, fids for different gates can be determined. In fact, J(*f*), the lower bound of J(), is actually very close to J(*o*). For example, if *nt* = 3000, delt = 5/*m'n'*, and *pme* = 5 are used, the first gate will give J(*o*) = -1.3697794 x 10^4, while J(*f*) = -1.3697903 x 10^4. Nevertheless, *fid*s still can be determined very precisely. For our images, *fid*s can be

determined according to the discrepancy rule as 3000, 2800, 2200, and 1800, for gate 1, 2, 3, and 4, respectively, which lead to the following results (Table 5-3, *mc* = 100).

Table 5-3 The average RSD and RME in the PoissTV-denoised images

	RSD	RME
The inner circle	0.1853	-0.0770
The ring	1.5889	-0.0374
The satellite	3.7043	-0.2698

The results are actually very good compared to the ROF case. The RSDs are as good as ROF with *nt* = 15000 while RMEs are still close to zero. Compared to the undenoised case, absolute values of RMEs are larger. This might be due to some intrinsic properties of PoissTV (or large pme), since repeated *mc* = 10 simulations show similar magnitudes of absolute values of RMEs. However, RMEs are not necessarily negative, as confirmed by these repeated *mc* = 10 simulations.

The reason why the fid values are smaller for later gates could be that the "relative distance" between J(*f*) and J(*o*), or [J(*o*)-J(*f*)]/J(*f*) is larger for later gates so that smaller fid is needed for J(*u*) to achieve J(*o*). For example, suppose Equation (5-4) represents the fourth gate and Equation (5-5) represents the first gate:

$$\frac{[110-100\log(110)]-[100-100\log(100)]}{100-100\log(100)}=\frac{0.4690}{-360.5170}=-0.0013 \tag{5-4}$$

$$\frac{[10100-10000\log(10100)]-[10000-10000\log(10000)]}{10000-10000\log(10000)}=\frac{0.4960}{-8.21\times10^{4}}=-6.0496\times10^{-6} \tag{5-5}$$

Here, standard deviation = square root of the intensity of *f*, is added to *f* to approximate *o*, according to Poisson distribution. As we can see, J(*o*)-J(*f*) itself does not make much difference, which can be confirmed by calculating J(*o*)-J(*f*) for gate 4 image: 0.118, 0.116, 0.110, and 0.109 versus J(*o*)-J(*f*) for gate 1 image: 0.101, 0.115, 0.104, and 0.113 (4 replicates). Therefore, a larger (less negative) J(*f*) (which is the case for later gates) has more difficulties moving up towards J(*o*) during iterations, even if J(*o*) is the same distance away from it, and this in turn requires a smaller fid to help. This may be quantitatively indicated by the signal-to-noise ratio (SNR), which is lower for later gates hence requesting *fid* also to be smaller to reach J(*o*), although detailed exploration on this has not been studied.

5.1.4 *f*-weighted TV (FWTV) model

5.1.4.1 Energy, gradient descent, and F(*u*)

The idea of *f*-weighted TV model (FWTV or *f*-weighted least squares TV), which is developed here in this study, is inspired from weighted least squares curve fitting, whose details can be found in the temporal approach chapter. Briefly, in both multiple and single exponential curve fitting for data with Poisson noise, since different variances are expected at different mean intensities, a weighting is used for each data point to account for different variance, such that a point intrinsically with larger variance (i.e. a point with larger intensity) has a smaller effect on the sum of squares. When Poisson noise is present, the weighting is equal to the intensity (or, 1/intensity when multiplying to the squares), which is equal to the variance. Upon fitting, the curve will reflect the best guess about what the intensities of the data points without noise should be. Therefore, usually the “expected value” rather than the “observed value” is used for weighting. This is the case of *u*-weighted least squares TV described below. However, the “observed

value" can also be used [18] and it has some advantages such as that it is simpler to compute and easier to handle, since the values of the data points (i.e. *f*, the given image) are constant through iterations.

The energy is defined as

$$E = \int |\nabla u| + \lambda \int \frac{(f-u)^2}{f} dx \tag{5-6}$$

To minimize this energy, we use the gradient descent

$$u_t = \nabla \cdot \left(\frac{\nabla u}{|\nabla u|} \right) + 2\lambda \frac{f-u}{f} \tag{5-7}$$

This form is very similar to the gradient descent of PoissTV. When encoded, 2*λ* can be regarded as a single coefficient.

We can define F(*u*) as

$$F(u) = \left(\int \frac{(f-u)^2}{f} dx \right)^{\frac{1}{2}} \tag{5-8}$$

which is used in the discrepancy rule for FWTV.

To implement FWTV, we also assign a variable *fme* = 5 to avoid the same problems such as zero denominator and negative intensities that may be generated through iterations (see Section 5.1.3.1). With *nt* = 3000 and *delt* = 5/*m'n'*, *fid* can go as high as 7000 (≈$10^{3.845}$), with which energy goes up first and then goes down, finally to a stable value. A lower *fme* should be acceptable, since in the gradient descent of FWTV, now

we have (*f*-*u*)/*f*. Once *u* gets negative, this term should be able to get *u* back to positive, since this time *u* is not present in the denominator as it was in PoissTV. Still, if *fme* is too small, there may still be some stability problems arising from the background pixels, probably due to the large *delt* we are using. Therefore, *fme* is still kept 5, not only for this reason, but also for comparisons with PoissTV.

5.1.4.2 Results

Again, we need to use the discrepancy rule to find the *fid*s to use. The same parameters used above lead to *fid*s = 2900, 2600, 2300, and 1800, for gate 1, 2, 3, and 4, respectively. With these fids we get the following results (Table 5-4, *mc* = 100).

When these results are compared with PoissTV, we find that the values are close. However, at this point FWTV has an advantage that it runs faster. For example, if *mc* = 10, FWTV takes 222 sec while PoissTV needs 295 sec to complete the same task on the same machine. More advantages of FWTV will be discussed later.

Table 5-4 The average RSD and RME in the FWTV-denoised images

	RSD	RME
The inner circle	0.1789	-0.0902
The ring	1.5857	-0.0439
The satellite	3.6098	-0.3511

5.1.5 *u*-weighted TV (UWTV) model

5.1.5.1 Energy, gradient descent, and U(*u*)

As mentioned in *f*-weighted least squares TV section, if the “expected value”, or the value of fitting model, *u*, is used for weighting, the fidelity term in the energy becomes regular weighted least squares for data with Poisson noise. This leads to

$$E = \int |\nabla u| + \lambda \int \frac{(f-u)^2}{u} dx$$

(5-9)

and the gradient descent to minimize this energy can be derived as

$$u_t = \nabla \cdot \left(\frac{\nabla u}{|\nabla u|} \right) + \lambda \left[\left(\frac{f}{u} \right)^2 - 1 \right]$$

(5-10)

Similarly, we can define U(*u*) as

$$U(u) = \left(\int \frac{(f-u)^2}{u} dx \right)^{\frac{1}{2}}$$

(5-11)

such that the discrepancy rule can be applied.

As before, a variable *ume* = 5 is assigned as *fme* in FWTV and *pme* in PoissTV to avoid some problems mentioned above.

5.1.5.2 Results

The discrepancy rule of UWTV (U(*u*) = U(*o*)) leads to (with the same parameters used above) *fid*s = 1400, 1400, 1000, and 850, for gate 1, 2, 3, and 4, respectively. The reason why *fid*s need to distribute in this way could probably be explained in the same approach as described in Section 5.1.3.2. Using these *fid*s with *mc* = 100 we get the following results (Table 5-5).

Table 5-5 The average RSD and RME in the UWTV-denoised images

	RSD	RME
The inner circle	0.1791	-0.0768
The ring	1.6044	-0.0647
The satellite	3.9295	-0.5477

Comparing these results with PoissTV and FWTV, the values are quite close. As for the running time, UWTV in fact runs even faster. For *mc* = 10, UWTV only takes 180 sec while FWTV needs 222 sec and PoissTV needs 295 sec as mentioned above.

Another issue we noticed is that by comparing the fids from the discrepancy rule (see Table 5-6), we roughly have UWTV ≈ 1/2 PoissTV ≈ 1/2 FWTV, which means that the *fid*s of PoissTV are probably equally effective as the fids of FWTV. The *fid*s of UWTV are half of them probably just due to the shift mentioned above.

Table 5-6 The fidelity coefficients from the discrepancy rule for the three TV models

	PoissTV	FWTV	UWTV
gate 1	3000	2900	1400
gate 2	2800	2600	1400
gate 3	2200	2300	1000
gate 4	1800	1800	850

5.2 Results of the artificial images, the second version

In order to draw a more general conclusion, we create the 2nd version of the artificial images with more strict conditions. The geometry is not changed. The dimension is changed to 128 × 128. Most importantly, the τ_1 value of the ring is changed from 9 to 5 and the α_1 value is made even smaller, changed from 100 to 50. In implementation of

denoising, the number of iterations is kept sufficiently high so that the energy is ensured to reach a stable value in the first half of the denoising process. The final values of J(u), F(u), and U(u) are also in the plateau regions where their changes through iterations are small. After some tests, nt and delt are fixed as 5000 and 10/*m'n'*, respectively, with *mc* = 20, and the following fids are used according to the discrepancy rule.

Table 5-7 The fidelity coefficients used in the denoising of the second version of the artificial images

	PoissTV	FWTV	UWTV
gate 1	11000	11000	5500
gate 2	6500	6500	3250
gate 3	4500	4500	2250
gate 4	3500	3500	1750

In fact, here we use the approximated rule of UWTV = ½ FWTV = ½ PoissTV after the fids of PoissTV have been determined, but each value is individually confirmed to be valid. Constrained ROF (denoted as conROF) is also used for a comparison.

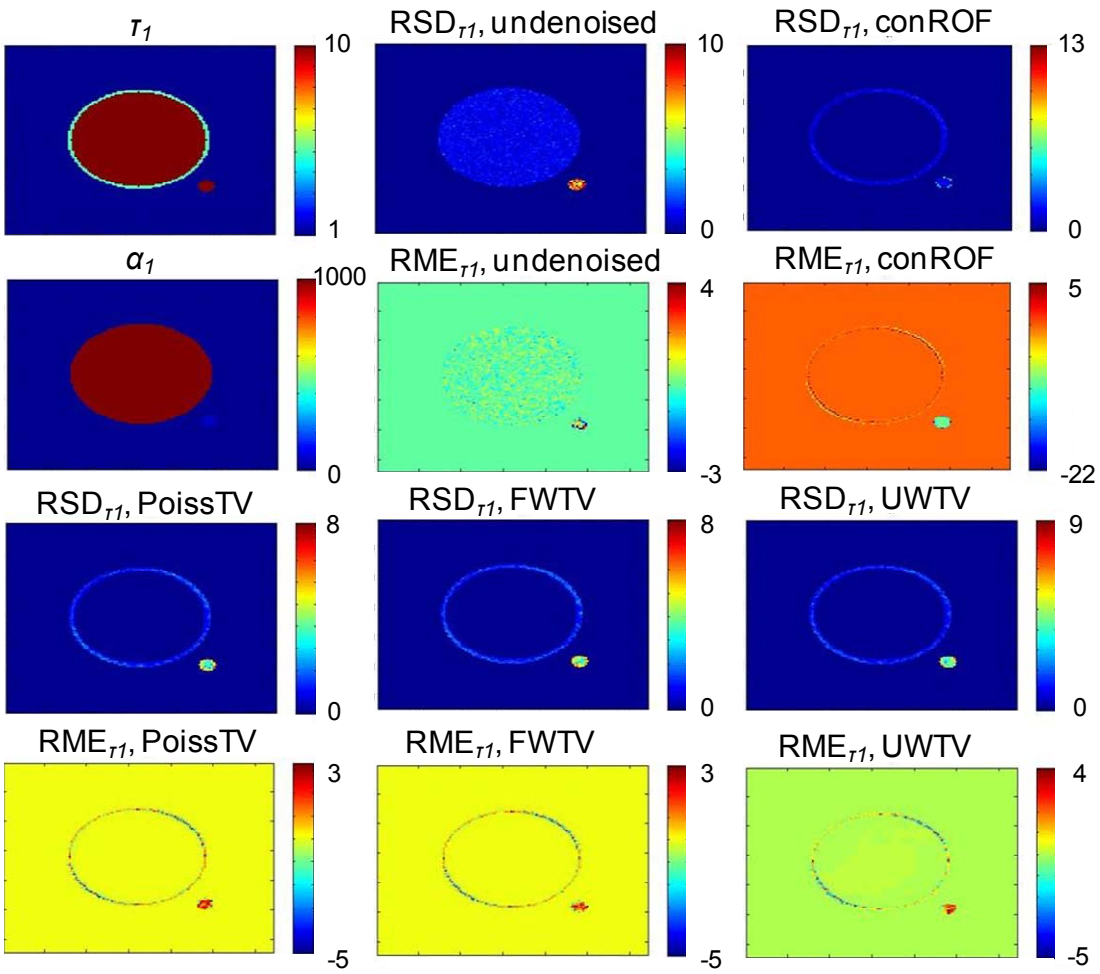

Figure 5-1 The MC simulation results of the second-version artificial images. All RSD and RME maps in all locations are provided as well as the τ_1 and α_1 setting. The average values are provided in Table 5-8.

Table 5-8 The average RSD and RME in the second-version artificial images Compared to the other three denoising models, the ROF model produces lower RSD in the ring and the satellite, but not the inner circle. The major problem of the ROF model is that it makes RME_{sate} extremely negative. The PoissTV, FWTV, and UWTV models produce similar results, while FWTV produces slightly better results than the other two in terms of RSD_{sate} and RME_{sate}.

	Undenoised		conROF		PoissTV		FWTV		UWTV	
	RSD	RME	RSD	RME	RSD	RME	RSD	RME	RSD	RME
The inner circle	1.8035	0.0350	0.1705	-0.0504	0.1304	-0.0409	0.1354	-0.0547	0.1358	-0.0122
The ring	1.9121	-0.0195	1.3291	-0.0981	1.4602	0.4169	1.4322	0.3185	1.4678	0.4422
The satellite	7.9012	0.0310	2.3643	-10.4076	4.8064	1.0790	4.7566	0.6787	4.9690	1.3683

The above shows a summary of the results. All RSD and RME maps and average values in all locations are provided as well as the τ_1 and α_1 setting. In the undenoised case, as we expect, the RSD_{sate} becomes higher comparing to the first version due to the "TC effect". Now RSD_{ring} becomes higher than RSD_{inner} because the gating scheme now is less close to the optimal scheme for τ = 5. On the other hand, RMEs still look random.

Compared to the other three models, the ROF model produces lower RSD in the ring and the satellite, but not the inner circle. Still, the major problem of the ROF model is that it makes RME_{sate} extremely negative.

The other three models give us similar results. If we look closer, FWTV produces better results in terms of RSD_{sate} and RME_{sate}. This, of course, depends on the conditions used in each model, but at least, FWTV is better in this one-time trial.

Also seen in the figure is the asymmetry in RMEs and possibly also in RSDs. This is not surprising because of the asymmetric discretization used in the Matlab code.

As for the running time, in this case we have conROF: 37.3 min, PoissTV: 51.6 min, FWTV: 34.1 min, and UWTV: 42.7 min. Again, UWTV and FWTV are faster than PoissTV. The reason why this time FWTV is faster than UWTV is unclear.

5.3 Improvement of FWTV and UWTV – incorporation of *G(N)* curves

5.3.1 Acquisition of *G(N)* curves

5.3.1.1 *G* and *G(N)*

The purpose of this section is to provide a method for the prediction of the variance of intensity counts in images such that the degree of image denoising in the TV models (this is possible only for FWTV and UWTV models) is appropriate. This is required since

in the unmodified UWTV and FWTV the counts in the images are assumed to be Poisson distributed. However, this is not true as long as there is a non-unity gain value in the conversion from photon counts to counts, or there are other forms of noise present in the images. We need an approach to incorporation of these factors into the UWTV and FWTV such that the evaluation of the variance of counts is correct.

To predict the variance of intensity counts in images, we take into account the gain effect, which is the overall conversion from the "photon counts" that are received by an intensifier to the "counts" in images shown, for example, on a computer screen. Generally, this gain effect will take into account other forms of noise and make variance predictable at different mean intensity counts.

To derive how the gain effect is used, some terminology is defined here. Let *N* = local mean intensity counts (from pixels with the same mean source photon counts), *G* = gain (1 photon count = *G* counts), and PC = photon counts.

The gain curve, *G(N)*, described as a function of local mean intensity "counts", has composite effects both from the real gain behavior of the instruments and from other forms of noise. More precisely, this is only a variance/*N* curve, to serve as an approach to estimation of variance from local *N*, as described below.

Theoretically, if only Poisson noise is present, we should have

$$N = \overline{G \cdot PC}$$

Assuming *G* is "at least locally" constant,

$N = G \cdot \overline{PC}$, and $\overline{PC} = N / G$

Also, since theoretically photon counts follow Poisson statistics

$std(PC) = \sqrt{\overline{PC}}$, and

$$std(counts) = G \cdot std(PC) = G \cdot \sqrt{\overline{PC}} = G\sqrt{N/G} = \sqrt{GN}$$

Therefore, $G = std(counts)^2 / N = \mathrm{var}(counts) / N$

Practically, *G* depends on counts, not only due to non-perfect electronic behaviors (instrumental gain), but also due to other forms of noise rather than Poisson noise present in the system. Therefore, more precisely, *G* is not the system gain in general anymore, as mentioned above.

When *G* is used as a function of *N*, *G(N)* will only be used locally, which means that *G(N)* will be used either pixel-by-pixel or as a local estimate of mean count value in the TV model gradient descent, '*o*' estimation, and fidelity term calculation. Therefore, *G(N)* is used interchangeably with *G*(counts). In addition, since *N* is local, in the above derivation *G* can always be assumed constant (as long as other factors such as pixel defects are negligible).

The following terms are also used in the following sections:

1. Ideal gain: The constant gain value if the electronics work ideally when there is only Poisson noise.
2. Instrumental gain: The non-constant gain if the electronics have *N*-dependent gain value when there is only Poison noise.
3. *G(N)*: The non-constant gain, or more precisely, variance/*N*, if the electronics have *N*-dependent gain value when there are Poison noise and other forms of noise.

5.3.1.2 TV models and estimation of '*o*': When *G* is constant

First, assume *G* is constant. Then, in FWTV, using *G* to evaluate the variance leads to a denominator of *Gf* in the integral of the fidelity term, namely

$$E = \int |\nabla u| + \lambda \int \frac{(f-u)^2}{Gf} dx$$

which directly leads to the gradient descent

$$u_t = \nabla \cdot \left(\frac{\nabla u}{|\nabla u|} \right) + 2\lambda \frac{f-u}{Gf}$$

Similarly, for UWTV we have

$$E = \int |\nabla u| + \lambda \int \frac{(f-u)^2}{Gu} dx \text{ , and}$$

$$u_t = \nabla \cdot \left(\frac{\nabla u}{|\nabla u|} \right) + \frac{\lambda}{G} \left[\left(\frac{f}{u} \right)^2 - 1 \right]$$

From gradient descent derivations, as shown above, *G* appears to be a constant combined with *λ*, as *λ/G*. Therefore, in the codes, incorporation of *G* into gradient descent is meaningless: To meet the discrepancy rule, the same constant, *G*, must be multiplied to *λ*, so that we finally will obtain *λ'* = *λG* that makes *λ'/G* = *λG/G* = *λ*, the original fidelity constant.

What is really affected by a constant gain is the evaluation of '*o*', the original uncorrupted image:

1. Previously, the estimate of *o* = *f** = poissrnd(*f*), and we (locally) have the noise-introduced variance as

$$\mathrm{var}(o) = \mathrm{std}(o)^2 = \frac{\sum (f^* - f)^2}{n-1} = f$$

2. Now, we need a new estimate

   $o = \sqrt{G}(f^* - f) + f$, such that we will have

$$\mathrm{var}(o) = \mathrm{std}(o)^2 = \frac{\sum (\sqrt{G}(f^* - f) + f - f)^2}{n-1} = Gf$$

5.3.1.3 TV models and estimation of '*o*': When *G = G(N)*

In this case, in FWTV we simply have

$$u_t = \nabla \cdot \left(\frac{\nabla u}{|\nabla u|} \right) + 2\lambda \frac{f - u}{G(f) f}$$

Since f is constant with respect to time.

For UWTV, the gradient descent has to be derived again.

$$E = \int |\nabla u| + \lambda \int \frac{(f - u)^2}{G(u)u} dx$$

$$\frac{dE}{dt} = -\int \nabla \cdot \left(\frac{\nabla u}{|\nabla u|} \right) u_t + \lambda \int \frac{-2(f - u)u_t G(u)u - (f - u)^2 \left[G(u)' u_t u + G(u) u_t \right]}{\left[G(u)u \right]^2} dx$$

Therefore,

$$u_t = \nabla \cdot \left(\frac{\nabla u}{|\nabla u|} \right) + \frac{\lambda}{\left[G(u)u \right]^2} \left\{ 2(f - u)G(u)u + (f - u)^2 \left[G(u)' u + G(u) \right] \right\}$$

In the estimation of '*o*', now we should locally have *G(f)* instead of *G*, such that

$$o = \sqrt{G(f)}(f^* - f) + f$$

Alternatively, we can also use

$$o = \sqrt{G(f)}randn(f) + f$$

where randn() generates random noise following normal distribution. We note that

1. In the first case, (*f*-f*) has standard deviation = $f^{1/2}$. Therefore the whole term has Poisson noise with standard deviation = $(G(f)f)^{1/2}$.
2. In the second case, the whole term has normal noise with standard deviation = $(G(f)f)^{1/2}$.

Both can used because when *G* = *G(N)*, the noise distribution actually includes both Poisson and normal noises, and, as long as the local standard deviation is correct ($(G(f)f)^{1/2}$), the evaluation is valid. In this study, the first is used.

5.3.1.4 Acquisition of *G(N)* curves: Temporal acquisition vs. spatial acquisition

The acquisition of *G(N)* curves involves calculations of standard deviation and *N* at different *N* for a large amount of pixel counts. These pixel counts can be obtained from a single pixel with multiple readouts (referred to as temporal standard deviation acquisition) or from different pixels within one single image readout (referred to as spatial standard deviation acquisition).

Temporal standard deviation acquisition: The light source can be either a lamp or a laser, but a lamp is always used for its higher stability. A fixed pixel is used, assuming that pixel is representative. *N* can be adjusted with the microscope aperture, and alternatively, with ND (neutral density) filters (if laser is used), or with different delays along the fluorescence decay (less controllable but faster, especially when multiple images are needed for each *N*). About 100 frames are acquired.

Spatial standard deviation acquisition: The light source can be either a lamp or a laser, but a laser is always used for its higher power. An ROI is used, where the pixels (usually more than 1000 pixels are included) are used to calculate standard deviation and *N*. The *N* can be adjusted in the same ways as in the temporal standard deviation acquisition: different delays are usually used, and an additional method is to take ROIs with different *N* in one single image. Only one frame is needed for each *N*.

Some comparisons of the performances of the two acquisition methods can be made. With spatial standard deviation acquisition, n_{pix} (the number of pixel used for standard deviation and *N* calculation) can be larger (at least several thousand), but any defects and difference in the pixels, as well as non-uniform distribution of the sample fluorescence will increase the standard deviation and hence *G(N)* values. On the other hand, if the light source is stable (such as a stable lamp) and the selected pixel is representative, temporal standard deviation acquisition should give the correct *G(N)* curve. However, if using pulsed laser as the light source, the instability of laser may become the main source of *G(N)* deviation in temporal standard deviation acquisition, but this will not be a problem for spatial standard deviation acquisition since frame-to-frame variation will not contribute to *G(N)*.

5.3.1.5 Acquisition of *G(N)* curves under CFP channel

The *G(N)* curves under CFP channel were acquired and analyzed in the following procedures:

1. If the spatial standard deviation acquisition is used, since the pixels in the images will be used to calculate the standard deviation under specified *N* values, the sample needs to be uniform. Therefore, in this case, a purified CFP solution can

be used. (other fluorophores with CFP emission wavelength range will work as well, and it does not need to decay single-exponentially)

2. If the temporal standard deviation acquisition is used, non-uniform sample such as cells transfected with CFP may be used. Ideally, temporal standard deviation acquisition with a lamp and the 'comb' mode (as in real live-cell experiments) is the best method to use.

3. However, since when using the usual setting in real experiments (g = 200 ps and dt = 1ns), the 'comb' mode with lamp will produce very weak signals, the spatial standard deviation acquisition is then used with a purified CFP solution, assuming uniform sample in the central part.

4. Other settings used are: 10x objective or 100x objective, MCP = 800, ECL 50, delay range = 45.977, trigger gate width = 10 ns, delay = 28 to 45 ns with increments of 1 ns. Both '1 avg' and '10 avg' are done; '10 avg' means each point comes from average of 10 images (or, n_{avg} = 10), which is the setting of real cell experiments.

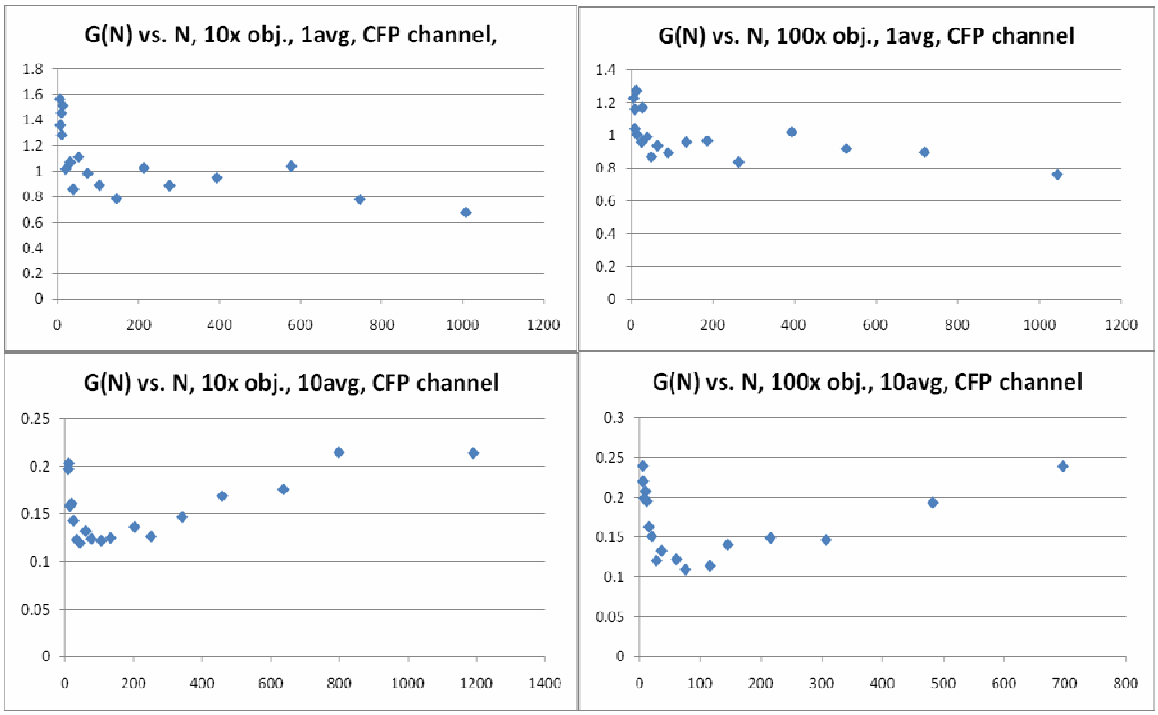

Figure 5-2 The *G(N)* vs. *N* curves under CFP channel. obj. = the objective used; avg = the number of images used for averaging

5. The results are shown in Figure 5-2. For each point, the pixels within the central part of the image are used to calculate *N* and the standard deviation, and the *G* is calculated as std.^{2}/*N* as a function of *N* (or the *N* decay, since each gate delay gives a different *N* value, which decreases as the gate delay increases). The number of pixels (n_{pix}) = 5151 for 10x objective, one average; 4131 for 100x objective, one average; 5751 for 10x objective, ten average; 3621 for 100x objective, ten average.

6. As expected and shown in the figure, 10x and 100 x objectives do not make significant differences.

7. Since $G(N) \propto$ std.^{2}, and std. $\propto 1/n_{avg}^{1/2}$, we have $G(N) \propto 1/n_{avg}$. Dividing the values of *G*(low *N*) at n_{avg} = 10 by *G*(low *N*) at n_{avg} = 1, the ratio value of ~0.125 is

obtained, which is reasonable. However, the tail of *G(N)* curve at n_{avg} = 10 curves up for unknown reason, which makes the ratio at higher *N* as high as ~0.3.

5.3.1.6 Analysis of *G(N)* curves

To model these curves, we assume there are three kinds of noise that make individual signal levels away from the mean value, *N*.

Signal = $noise_1$ + $noise_2$ + $noise_3$ + *N*

where $noise_1$ = background noise with std($noise_1$) = $\sigma_1 = C_1$ = $constant_1$

$noise_2$ = Poisson noise with $\sigma_2^2/N = C_2$ or $\sigma_2 = (C_2 N)^{1/2}$

$noise_3$ = extra noise (from laser variation or other factors) with $\sigma_3/N = C_3$ or $\sigma_3 = C_3 N$

Therefore, $\sigma_{signal}^2 = \sigma^2 = C_1^2 + C_2 N + C_3^2 N^2$ and $\sigma^2/N = G(N) = C_1^2/N + C_2 + C_3^2 N$

with C_1 = the standard deviation of the background noise

C_2 = the ideal gain

C_3 = the RSD of the extra noise

In fact, the third kind of noise turns out to be an instrumental behavior such that $C_2 + C_3^2 N$ become the instrumental gain.

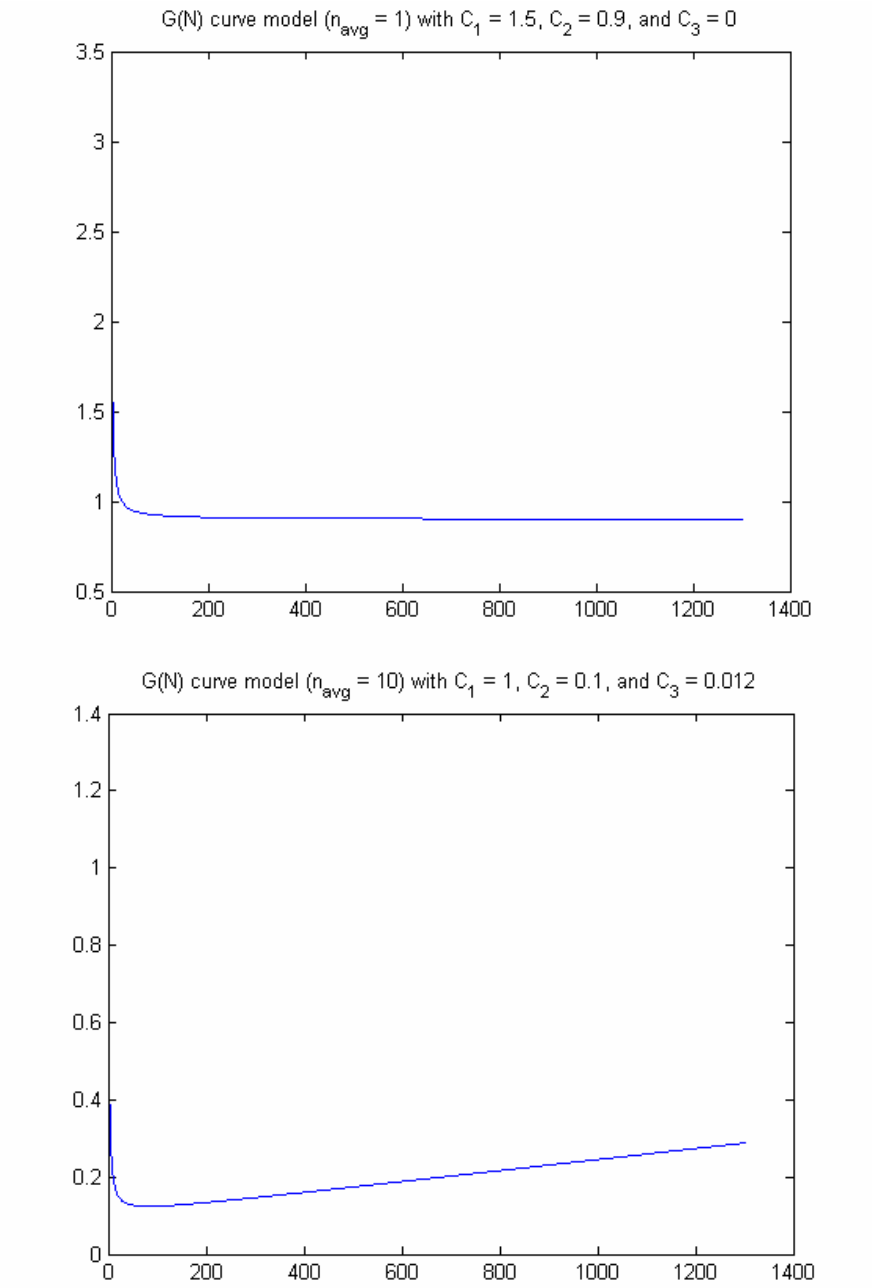

Figure 5-3 The modeled *G(N)* vs. *N* curves for n_{avg} = 1 and n_{avg} = 10. Note that C_1 = 1.5 at n_{avg} = 1, which is close to the manufacturer-specified value of 2 for the standard deviation of the background (readout) noise as mentioned earlier in Section 2.2.4. In addition, the third term characterized by C_3 arises possibly from the spatial laser variations, which become more significant when other forms of noise are averaged out and when the intensity increases (Section 2.2.4).

Using different values for the constants C_1, C_2 and C_3, the *G(N)* curves can be modeled for both n_{avg} = 1 and n_{avg} = 10 as shown in Figure 5-3. Note that C_1 = 1.5 at n_{avg}

= 1. This is quite consistent with the manufacturer-specified value of 2 for the standard deviation of the background (readout) noise as mentioned earlier in Section 2.2.4 about the system variations. In addition, it is very likely that the extra noise arises from the spatial laser variations since they should have fixed RSD and become more significant when other forms of noise are averaged out and when the intensity increases (see Section 2.2.4).

5.3.2 Effect of *G* and *G(N)* curves – results of live-cell images

With a constant *G* and the modeled *G(N)* curve used in '*o*' estimation, UWTV, and FWTV models, we re-evaluate these two TV models with the setting described below. The denoising models are applied to images with CV1 (monkey kidney epithelial) cells transfected with Cerulean (an enhanced version of CFP). These images are acquired with our FLIM system. Cerulean fluorescence was excited at λ_{ex} = 436±10 nm using the laser dye Coumarin 440 and collected at λ_{em} = 480±20 nm. This set of images can serve as a good low-light example since the intensities are low and so are the signal-to-noise ratios. The four-gate protocol is used with *dt* = 1.0 ns and *g* = 0.2 ns. Ten images were taken for each gate (n_{avg} = 10). We use a new filter which only takes the $\tau > 0$ region under the undenoised case. This helps us remove the extra zero pixels in the evaluation of the average τ, α, R^2, and χ^2 values. A constant *G* = 0.466474 is also used, as evaluated with a series of data taken with the Cerulean-transfected cells, a 100x objective, n_{avg} = 10, and the spatial standard deviation acquisition method (Section 5.3.1.4). This *G* value is higher than the values in the *G(N)* curve for n_{avg} = 10 (Figure 5-3) due to the intrinsic non-uniformity of the live cells.

Significant improvement of FWTV and UWTV can be achieved with the *G(N)* curve (n_{avg} = 10): With live-cell images, they can improve the precision of local lifetime

determination without significantly altering the global mean lifetime values. This result is demonstrated in Table 5-9 (the numbers in red, blue, and green). Taking FWTV with *G(N)* (the numbers in blue) as an example, the results indicate that, after FWTV w/*G(N)* denoising, there is a notable improvement in the mean R^2 (from 0.8960 to 0.9508) and χ^2 (from 0.8956 to 0.3559) values, and hence, the precision associated with local lifetime determination. In addition, the mean lifetime and pre-exponential terms are not significantly affected by the denoising algorithm. UWTV w/*G(N)* shows similar results as well. Again, these favorable results are attributed to the flexibility of the FWTV and UWTV weightings to incorporate the *G(N)* curve, which can take into account additional ICCD errors that only exist in real images.

Table 5-9 The average τ, α, R^2, and χ^2 values in the real live-cell images before and after denoising with various TV models (under the filter 'undenoised $\tau > 0$'). FWTV and UWTV with the *G(N)* curve (n_{avg} = 10) can improve precision of local lifetime determination without significantly altering the global mean lifetime values (the numbers in red, blue, and green). Without incorporation of the *G(N)* curve, the average lifetime values always deviate from the undenoised lifetime value. The constant *G* value = 0.466474.

	Undenoised	**PoissTV**	**FWTV**	**FWTV w/*G(N)***	**UWTV**	**UWTV w/*G***	**UWTV w/*G(N)***
τ	2.8362	3.5952	2.2739	2.8412	3.6331	3.6522	2.8717
α	142.2	159.272	125.455	144.87	158.9891	161.6655	145.5
R^2	0.896	0.9852	0.9827	0.9508	0.9858	0.9719	0.9509
χ^2	0.8956	0.0857	0.0885	0.3559	0.0824	0.1641	0.3502

Without incorporation of the *G(N)* curve, the average lifetime values always deviate from the undenoised lifetime value. In Table 5-9, the average lifetime values after the denoising of PoissTV (3.5952), unmodified FWTV (2.2739), and unmodified UWTV (3.6331) deviate from that of the undenoised case (2.8362). In addition, UWTV with the constant *G* = 0.466474 does not produce an appropriate lifetime value, either. Although this may be attributed to the fact that the constant *G* is larger than the values on the *G(N)* curve, this *G* is, however, obtained directly from the Cerulean-transfected cells. On the

other hand, the *G(N)* curve is obtained from another sample (a purified CFP solution). This demonstrates that the obtained *G(N)* curve can be used as a generic curve for any samples under the same setting.

The images, as shown in Figure 5-4, indicate that noise is removed from the images after FWTV w/*G(N)* and UWTV w/*G(N)* denoising with basically unchanged mean lifetime, which can be seen from the color scale. On the other hand, although PoissTV produces a much smoother image, the lifetime values deviate significantly from the expected values.

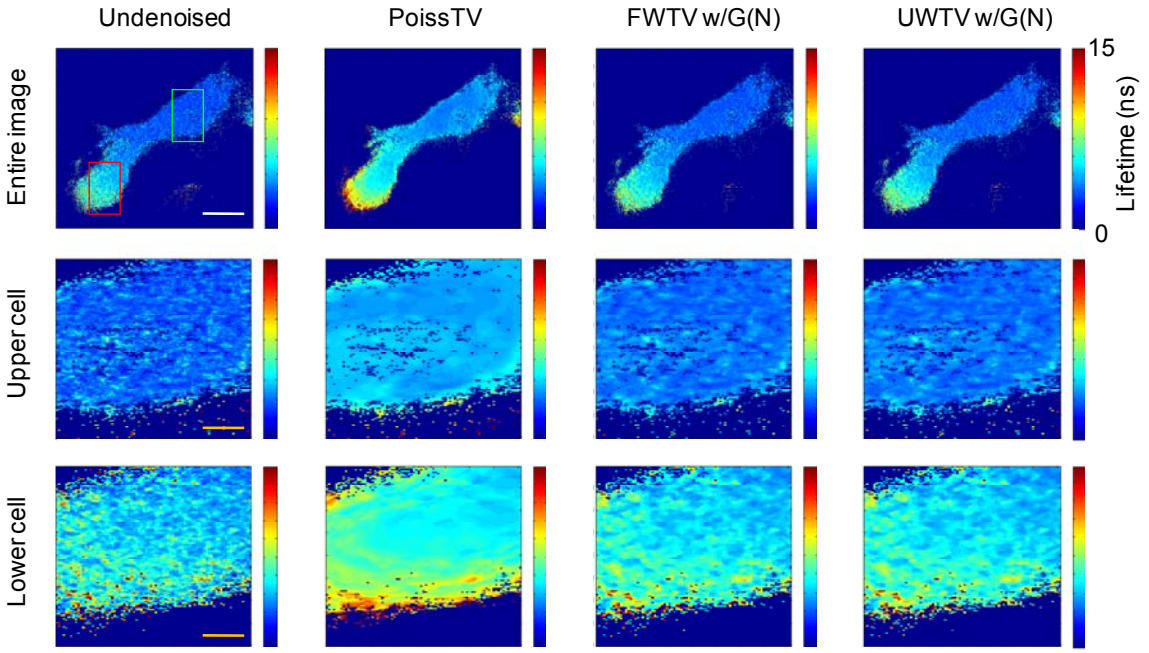

Figure 5-4 The lifetime maps of live CV1 cells transfected with Cerulean (see the text in Section 5.3.2 for the sample preparation details): undenoised or after denoising with various TV models. The second row and the third row illustrate the corresponding enlarged maps from the areas indicated by the green rectangle (the upper cell) and the red rectangle (the lower cell), respectively. White scale bar (for the first row): 30 μm; orange scale bar (for the second and the third rows): 3.5 μm

5.3.3 Factors affecting lifetime changes with the modified denoising

In this section we further investigate how the accuracy of the modified denoising models may be affected in areas with different local mean lifetime values in the real live-cell images.

FWTV w/*G(N)* and UWTV w/*G(N)* denoising gives acceptable percentage τ changes in the areas where the mean lifetime values are different (shown with the numbers in blue in Table 5-10). In our results in Table 5-10, τ change (%) after denoising relative to the corresponding undenoised case is indicated. This is done with both FWTV w/*G(N)* and UWTV w/*G(N)*, and with both the green rectangle area (the upper cell) and the red rectangle area (the lower cell) shown in Figure 5-4. In all these four cases, the percentage τ changes are below five percent.

Table 5-10 The average τ, α, R^2, and χ^2 values of the upper and the lower cells in the real live-cell images (the green rectangle and the red rectangle in Figure 5-4, respectively) before and after denoising with FWTV w/*G(N)* and UWTV w/*G(N)* (under the filter 'undenoised $\tau > 0$'). The lifetime change and lifetime change (%) relative to the corresponding undenoised case are also shown. In all cases, lifetime changes (%) are below five.

	Upper cell			**Lower cell**		
	Undenoised	**FWTV w/*G(N)***	**UWTV w/*G(N)***	**Undenoised**	**FWTV w/*G(N)***	**UWTV w/*G(N)***
τ	2.0684	2.1497	2.1664	3.6269	3.6877	3.702
α	156.5918	158.6783	159.4223	183.9866	187.3064	188.0226
R^2	0.936	0.973	0.973	0.8854	0.9445	0.945
χ^2	1.0092	0.3901	0.3859	0.8801	0.3575	0.3522
τ change	0	0.0813	0.098	0	0.0608	0.0751
τ change (%)	0	3.93	4.74	0	1.68	2.07

In this example shown in Table 5-10, the upper cell always has larger lifetime changes (%), and this may result from the following reasons. It may be attributed to the fact that the upper cell has lower mean lifetime. This speculation is reasonable, because lower mean lifetime indicates lower SNR in the later gates, when the SNRs in the first gate are similar. The modeled *G(N)* curve region at low SNR may have larger errors relative to the actual *G(N)* curve. Another possible reason for the larger lifetime changes in the upper cell is the different geometry in the two cell areas. The effect of geometry is more difficult to predict and explain and will need further investigation.

Finally, we notice that the FWTV w/*G(N)* and UWTV w/*G(N)* denoised cases always have slightly higher lifetime and pre-exponential term values compared to the undenoised case. This is also true for the entire image (Table 5-9). This may, again, arise from any tiny differences between the actual *G(N)* curve and the modeled *G(N)* curve, and can therefore be solved if the modeling parameters are further refined.

Chapter 6 Combination of temporal and spatial approaches for further precision improvement in FLIM

As mentioned in the previous chapters, two kinds of methods have been considered to improve the precision of time-gated FLIM systems – the temporal method and the spatial method. Since the temporal and spatial methods apply to different dimensions and different stages of the time-gated FLIM, we assume that they can work together to confer even better precision than any one of the two methods applied alone.

Our goal in this chapter, therefore, is to demonstrate that the novel combination of these two methods can achieve higher precision in low-light imaging than that in high-light cases (in our example, RSD = 12.76% at total photon counts, or TC, = 100 vs. RSD = 23.03% at TC = 400). This can avoid unnecessary high-intensity excitation of living cells (hence avoiding possible cell damaging and photobleaching) and allow meaningful detection of fluorescence when there is low fluorophore concentration - two major problems associated with live-cell fluorescence-based imaging.

6.1 Performance of the combined approach

We conducted an experiment to test the performance of the combined temporal and spatial approaches and the relevant details are as follows. The RSD (%) values before and after the application of optimal gating (the temporal method) and FWTV (with *G(N)*, see Section 5.3.2) denoising (the spatial method) are shown in Table 6-1. In this

experiment, *g* is fixed at 10 ns, and *dt* = 0.5 ns for non-optimal gating and 2.5 ns for optimal gating. The RSD values are calculated from all non-zero pixels in the images of the fluorescent beads. The sample preparation details are described in Section 4.2.2, and some of the values in Table 6-1 (TC ≈ 100, undenoised) and their corresponding images are shown in Figure 4-10. FWTV is used because it is believed to produce very similar results to those of UWTV but relatively easy to handle. As mentioned in Chapter 5, FWTV and UWTV are more flexible and can better take the system nonlinear behaviors into account and hence are used here. The four-gate protocol is used in this experiment.

With the optimizations, the precision of lifetime determination in low-light imaging can be comparable to or even better than that in high-light imaging. This is demonstrated with Table 6-1. Note that both TC ≈ 100 and TC ≈ 400 can be regarded as fairly low-light imaging, causing noisy lifetime maps from real experiments for live-cell imaging, such as the lifetime maps shown in Figure 3-3. In Table 6-1, we can first notice that when TC ≈ 100, after gating optimization, there is a significant reduction of RSD, resulting in a final RSD of 18.93 % (in red). This gating-optimized low-light RSD is lower than the RSD at a higher excitation, TC ≈ 400, without any optimizations (23.03%, in blue). In addition, 18.93% is close to the RSD at TC ≈ 400 with FWTV denoising (17.26%, in pink). When FWTV denoising is further applied to the optimal-gated low-light images, the further decreased RSD (12.76%, in green) is now lower than both the undenoised and denoised non-optimal high-light cases (the blue and the pink numbers). Further gating optimization can be applied to the high-light case to achieve even better precision and will be discussed later in the next section.

Our conclusion with Table 6-1 is that, with our optimization approaches, even low-light excitation can achieve precision that is better than that in high-light cases.

Therefore, high-intensity excitation can be avoided when it is unfavorable due to, for example, potential cell damage and fluorephore photobleaching.

Table 6-1 The RSD (%) values before and after the application of optimal gating (the temporal method) and FWTV (with *G(N)*) denoising (the spatial method). *g* is fixed at 10 ns. *dt* = 0.5 ns for non-optimal gating and 2.5 ns for optimal gating. The RSD values are calculated from all non-zero pixels in the images of the fluorescent beads (see Figure 4-10 and Section 4.2.2). TC = total photon counts. Note that both TC ≈ 100 and TC ≈ 400 can be regarded as fairly low-light imaging, causing noisy lifetime maps from real experiments for live-cell imaging, if not optimized.

	TC ≈ 100		TC ≈ 400	
gating	non-optimal	optimal	non-optimal	optimal
undenoised	52.57	18.93	23.03	7.58
FWTV-denoised	45.51	12.76	17.26	6.11

Figure 6-1 demonstrates that the noise reduction is, in fact, obviously very easy to observe, even without comparing the RSD values. Figure 6-1 also serves as an example of how the combined approach will have an impact on the images of low-light FLIM. In this figure, the noise distribution within the fluorescent beads is illustrated. Note that in this case, again TC ≈ 100, which is actually an extremely low-light case. The RSD values are calculated only with the beads shown in the figure, and hence are slightly different from those in Table 6-1. The holes inside the fluorescent beads (Figure 6-1 (a)) came from one of the lifetime calculation steps in which the lifetime values above a certain threshold were set to zero (see Section 2.2.3). Since this threshold was set to lifetime = 15 ns, random fluctuation within the low-light images caused some pixels to have lifetime values more than three times larger than the expected values if the gating scheme was not optimal. After denoising (Figure 6-1 (c)), the image became smoother and the RSD value dropped, but the extremely high lifetime values above the threshold still could not be removed. Optimal gating (Figure 6-1 (b)) removed these artifacts and further decreased the RSD value, as well as reducing the diameter of the beads so that

it became closer to the actual bead size of 10 μm. Further improvement was then achieved by denoising the optimally-gated image (Figure 6-1 (d)). A comparison of Figure 6-1 (b) and (d) shows that most of the remaining lifetime variations within the beads in the optimally-gated image could be removed by denoising. Here, the combination of the temporal and spatial techniques resulted in about a five-fold improvement in precision (or reduction in RSD).

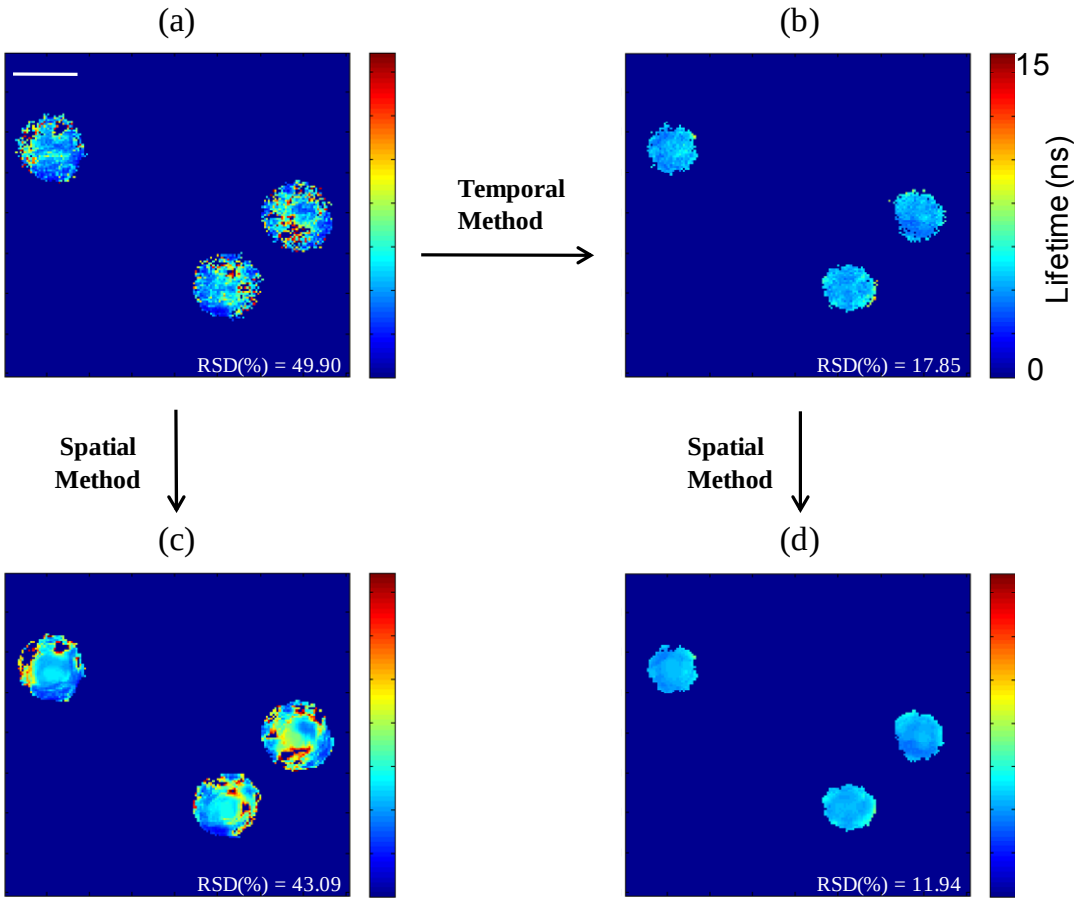

Figure 6-1 FLIM images of fluorescent beads (see Section 4.2.2 for the sample preparation details) acquired with a gate width of 10 ns and various values of the time interval *dt* between two gates: (a) *dt* = 0.5 ns, undenoised; (b) *dt* = 2.5 ns (optimal), undenoised; (c) *dt* = 0.5 ns, FWTV-denoised; (d) *dt* = 2.5 ns (optimal), FWTV-denoised. The improvements in precision from temporal method (~32% of RSD decrease) and spatial methods (~6% of RSD decrease) are additive and both easily observable in this extremely low-light case (total photon counts is around 100), which can be encountered in real experiments for live-cell imaging. The labeled RSD values were obtained from all non-zero pixels in the images. Scale bar: 15 μm.

With Figure 6-1, we conclude that the temporal and spatial methods can be employed either independently or in combination to improve the precision in low-light time-gated FLIM. When the two methods are combined, their notable five-fold (from 49.90% to 11.94%) improvements in precision can be easily observed in our extremely low-light example.

6.2 Linearity of the two approaches

In this section, we further discuss how the two approaches behave when used in combination. Figure 6-2 conceptually shows the RSD reduction resulting from the combination of the two approaches (with the RSD numbers shown in Table 6-1). We notice some facts as described in the following paragraphs.

The temporal method is linear in terms of its operation with respect to the TC effect. This is demonstrated by the fact that the optimal gating reduces the RSD values by about three-fold for both TC ≈ 100 and TC ≈ 400 cases as shown in Table 6-1 (from 52.57 to 18.93 and from 23.03 to 7.58). This phenomenon is also shown in Figure 6-2 with the green arrows. It is a reasonable result and is explained below. First, the TC effect on RSD (RSD $\propto$ $1/(TC)^{1/2}$) should roughly hold for any gating scheme. In other words, this effect should be applicable for every point on the RSD vs. gating scheme curves in both Figure 6-2 (a) and (b). Then, let us take a look at the TC effect on RSD in Table 6-1 for the non-optimal gating: $52.57/23.03 = 2.28 \approx (400/100)^{1/2} = 2$. The difference between 2.28 and 2 may result from the nonlinear behavior with the extremely low-light excitation. This TC effect is also illustrated by the less steep RSD vs. gating scheme curve in Figure 6-2 (b) (TC ≈ 400 case) compared to that in Figure 6-2 (a). For the optimal-gating case, this effect is roughly true as well (the ratio = 2.50). Since the proportional reduction in RSD is similar for the non-optimal and optimal gating schemes

(because they are still on the same curves), temporal optimization gives similar proportional reduction in RSD (three-fold) with different TC values (as long as the TC effect holds).

The spatial method, on the other hand, is not linear, but can be additive in RSD reduction. This is demonstrated by the fact that, taking TC ≈ 100 as an example (Table 6-1), the RSD reduction by the spatial method (denoising) is not proportional for the non-optimal and optimal gating schemes [(52.57-45.51)/52.57 ≠ (18.93-12.76)/18.93]. As we can see, in both cases, the RSD reduction tends to be a fixed value around 6 % and this is also true for the non-optimal gating under TC ≈ 400 (23.03-17.26 ≈ 6). However, for the optimal gating under TC ≈ 400, the RSD reduction becomes much smaller (<1.5%). In Figure 6-2, the reduction in RSD by the spatial method is denoted with blue arrows.

There are several possible factors that will affect the RSD reduction by the spatial denoising. First, of course, the RSD reduction cannot be simply additive if the RSD of the undenoised image is already low, since RSD cannot be negative. Also, we should not expect RSD values to be very close to zero, either, since that will require a perfectly uniformly-distributed fluorescent sample (at the non-zero pixels). Therefore, in the optimal-gated TC ≈ 400 case, RSD = 6.11 may be already close to the limiting RSD that reflects the intrinsic sample non-uniformity (i.e. the sample features that will not be removed by denoising). On the other hand, the reason why the RSD reduction resulting from the spatial denoising can be additive (when RSD values are high enough) may be that the denoising process is more dependent on the geometry of the objects and the relative locations of pixel information in the images.

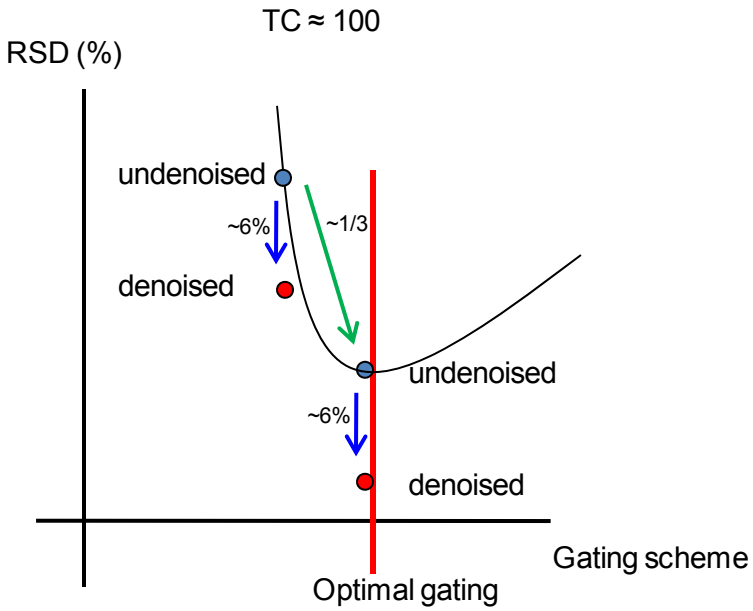

(a)

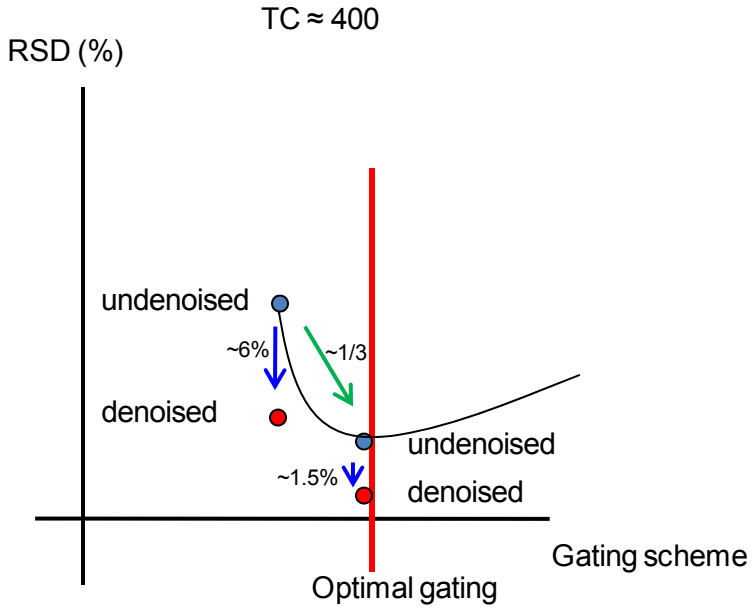

(b)

Figure 6-2 The RSD reduction shown on RSD (%) vs. gating scheme plots. Refer to Table 6-1 for the RSD values. (a) TC ≈ 100. (b) TC ≈ 400. The temporal method is linear in terms of its operation with respect to the TC effect (the green arrows) while the spatial method is not linear, but can be additive in RSD reduction (the blue arrows).The locations of the points are not drawn to scale. Note that both TC ≈ 100 and TC ≈ 400 can be regarded as fairly low-light imaging, causing noisy lifetime maps from real experiments for live-cell imaging, if not optimized.

Further studies can be conducted to confirm the above hypotheses. For example, artificial images could be used. However, to take into account any unexpected behaviors of the FLIM system, a uniformly-distributed sample may be used with the system. Yet, this sample should not be a uniform solution, since we also would like to illustrate any effect of denoising on the geometry of the objects in the images.

As a summary, the temporal method is linear in terms of its operation with respect to the TC effect, while the spatial method is not linear. The spatial method can work additively to the temporal method in RSD reduction, provided that the residual variation is not low. Finally, the effect of the spatial method depends on the residual variation to start with, the intrinsic sample non-uniformity, and the geometrical information.

Chapter 7 Conclusions and future work

7.1 Conclusions

In this study, we demonstrated that we can significantly improve accuracy and precision in fluorescence lifetime imaging microscopy (FLIM) applications, and, therefore, provide better quantification in determining cellular and molecular responses to environmental changes in living cells without perturbing them. The accuracy was improved (better statistics and less non-specific signals; for negative control comparisons, *p*-value = 0.93 (physiological) vs. 9.43E-05 (non-physiological)) by using a better fluorophore and the incorporation of environmental controls. The precision was improved (RSD from 49.90% to 11.94%) via our temporal and spatial approaches, developed in this study. With the combined approach, even low-light excitation can achieve precision better than that in high-light cases (RSD = 12.76% at TC = 100 vs. RSD = 23.03% at TC = 400). Therefore, high-intensity excitation can be avoided when unfavorable.

As for the accuracy problems specific for fluorescence resonance energy transfer (FRET) [19, 21, 34-37], including spectral cross-talk and bleed-through, random/unexpected association of FRET pairs (non-specific FRET), and possible disturbances in the fluorophores' environment (pH and temperature), we demonstrated that these problems can be solved with FLIM (no corrections are required for spectral

cross-talk and bleed-through) while others can be further solved or made negligible in well-controlled, comparative, FRET-FLIM experiments.

Further, the precision of FRET determination by FLIM is improved with our temporal (regarding data acquisition) and spatial (regarding image analysis) optimization methods. For the temporal method, in the example of FRET efficiency determination in Chapter 1 (total photon counts = 10^2; [DA] = ~90%([DA]+[D]); lifetime changes from 3 ns to 0.6 ns due to FRET; rapid lifetime determination (RLD) was used), there was more than 35% RSD in FRET efficiency determination. With maximum likelihood estimation (MLE) and 20 gates, the RSD can be reduced to 5.6%. As for the spatial method, we also demonstrated that the local precision of lifetime determination can be significantly improved (the average R^2 increased from 0.8960 to 0.9508 and the average χ^2 decreased from 0.8956 to 0.3559 for one of our novel models; see Table 5-9 and Figure 5-4). Therefore, lifetime-based FRET efficiency determination can be improved as well.

This study, therefore, overcomes the challenges in constructing useful quantitative models by enabling lifetime map construction for better quantification of molecular interactions and sub-cellular environmental changes in live cells. The proposed methods can remove intensity-based artifacts and provide better detection of the localization of molecular interactions. As explained in the introduction, this can be applied in quantitative pharmacokinetics and pharmacodynamics models for clinical use.

In **Chapter 2**, we describe the theories of fluorescence lifetime, the instrumentation of our wide-field time-gated FLIM system, and the detailed analytical procedures used in the temporal and spatial approaches. This provides further understanding of the techniques described in the chapters that follow. The discussions of the FLIM system variations also provide a basis for the detailed analyses regarding the system noise mentioned in Chapter 4 and Chapter 5.

In **Chapter 3**, we show that FLIM, the choice of a better fluorophore, and the inclusion of environmental controls indeed improve the quantitative fluorescence resonance energy transfer (FRET) results. We first demonstrate that the imaging of molecular interactions in living cells via FRET can be better detected with FLIM than with intensity, and the consistency of these results can be improved by the use of a better fluorophore, Cerulean. We also demonstrate that the effect of temperature can be well taken into account in FRET detection with FLIM, and further incorporation of CO_2 control provides better FRET statistics and less non-specific FRET.

In **Chapter 4**, several approaches to double-exponential fluorescence / luminescence lifetime determination in time-gated FLIM are investigated in search of optimal gating schemes and we conclude that WNLLS and MLE are needed for higher precision, while NLLS and RLD are better used when little is known about the sample parameters. Among all the methods, MLE has the best precision and MLE at number of gates = 10 is a good choice in most cases. In addition, relative change of *dt* (the time interval between the beginnings of two consecutive gates) has a much greater impact on RSD than *g* (the gate width) does, and this effect is strongest in RLD. The simulation results are validated with experiments.

In **Chapter 5**, we compare various TV denoising models to improve the precision of FLIM, and conclude that significant improvement of the two TV models developed in this study, FWTV (*f*-weighted TV) and UWTV (*u*-weighted TV), can be achieved with a *G(N)* curve, which takes into account a variety of noise that will be encountered in a real imaging system. With live-cell images, they can improve the precision of local lifetime determination without significantly altering the global mean lifetime values. Other TV models such as the commonly used ROF model and the Poisson-noise-adapted TV

model do not have the flexibility to include a *G(N)* curve. Therefore, they are not as practically useful as our FWTV and UWTV.

In **Chapter 6**, our conclusion is that, with our combined temporal and spatial optimization approaches, even low-light excitation can achieve precision that is better than that in high-light cases. Therefore, high-intensity excitation can be avoided when it is unfavorable due to, for example, potential cell damage and fluorophore photobleaching. In addition, the improvements in precision can be easily observed without calculations of relative standard deviations (RSDs).

The major contributions of this dissertation can be summarized as follows:

1. Demonstrated that the use of the fluorophore Cerulean, compared with ECFP, improves the consistency of FLIM-based FRET experiments. Only lifetime measurements can reveal this improvement.
2. Demonstrated that temperature and CO_2 controls for live cells can provide better FRET statistics and less non-specific FRET in FLIM-based FRET experiments but not in intensity-based measurements. This enables more accurate detection of molecular interactions in live cells.
3. Constructed maps of optimal gating schemes to achieve the best precision in practical sample parameter ranges for three different lifetime determination methods: rapid lifetime determination (RLD), maximum likelihood estimation (MLE), and weighted nonlinear Least-squares (WNLLS).
4. Demonstrated that high precision can be achieved with low number of gates in gated FLIM when using the nonlinear lifetime determination methods (MLE and WNLLS). This can significantly reduce light delivery in live-cell experiments.

5. Demonstrated that the time interval between two consecutive gates has larger impact on the precision of the time-gated FLIM than the gate width. This greatly helps determination of sub-optimal gating schemes for a single sample with various fluorophore distributions.

6. Developed two novel Total Variation (TV) denoising models, f-weighted TV and u-weighted TV models, and demonstrated that they help achieve significantly more accurate lifetime determination than a commonly used TV model, Rudin-Osher-Fatemi model, when used with time-gated FLIM.

7. Developed a novel approach for simultaneous characterization of various forms of noise (Poisson noise, readout noise, and other noise) in real imaging systems to be used in Total Variation denoising models.

8. Demonstrated for the first time, that the temporal and spatial methods can be combined to achieve precision in low-light imaging even better than that in high-light imaging. This can avoid unnecessary high-intensity excitation of living cells and prevent possible cell damaging and photobleaching.

The work in this dissertation has been presented and documented as cited below:

Chapter 2:

- Chang, C.W., D. Sud, and M.A. Mycek, “Fluorescence lifetime imaging microscopy”. Methods Cell Biol, 2007. 81: p. 495-524.

- Xu, Z., Raghavan, M., Hall, T. L., Chang, C. W., Mycek, M. A., Fowlkes, J. B., Cain, C. A., “High speed imaging of bubble clouds generated in pulsed ultrasound cavitational therapy-histotripsy”, *IEEE Trans. Ultrasonics Ferroelectrics Freq. Control*, 2007, 54 (10), 2091-2101

- Xu, Z., Raghavan, M., Hall, T. L., Chang, C. W., Mycek, M. A., Fowlkes, J. B., Cain, C. A., “High Speed Imaging of Bubble Clouds in Pulsed Cavitational Ultrasound Therapy-Histotripsy”, *Proc. IEEE International Ultrasonics Symposium, 1D-4,* Vancouver, Canada, October 3-6, 2006

Chapter 3

- Chang C.W., M. Wu, S.D. Merajver, and M.A. Mycek, “Environmentally controlled FLIM enables FRET detection in living cells”, manuscript in preparation for Journal of Biomedical Optics
- Chang C.W., M. Wu, S.D. Merajver, and M.A. Mycek, “Improving FRET Detection in Living Cells”. European Conferences on Biomedical Optics, Munich, Germany, June 14–18, 2009 (accepted)
- Chang, C. W., Rosenthal, D., Wu, M., Merajver, S., Mycek, M. A., “Detecting Molecular Interactions in Live Cells: Environmental Controls for FLIM-based FRET Detection”, BMES 2008 Annual Fall Meeting, October 2-4, 2008
- Zhong, W., M. Wu, C.W. Chang, K.A. Merrick, S.D. Merajver, and M.A. Mycek, “Picosecond-resolution fluorescence lifetime imaging microscopy: a useful tool for sensing molecular interactions in vivo via FRET”. Optics Express, 2007. 15(26): p. 18220-18235.
- Chang, C. W., Rhee, E., Wu M., Merajver S., Mycek M. A., “Imaging molecular interactions of oncogene RhoC in living cells using FLIM/FRET”, Optical Imaging 2006 Fifth Inter-Institute Workshop on Optical Diagnostic Imaging from Bench to Bedside at the National Institutes of Health, Bethesda, Maryland, September 25-27, 2006

Chapter 4

- Chang, C. W., Mycek, M. A., “Optimal Schemes for Retrieving Luminescence Lifetime from Double-Exponential Decay with Gated Integration”, manuscript in preparation
- Chang, C. W., Mycek, M. A., “Improving Precision in Fluorescence Lifetime Imaging Microscopy for Low-Light Live-Cell Imaging”, BMES 2008 Annual Fall Meeting, St. Louis, Missouri, October 2-4, 2008

Chapter 5

- Chang, C. W., Mycek, M. A., “Applying Total-Variation Denoising Models to Images Acquired from Time-Gated Fluorescence Lifetime Imaging Microscopy”, manuscript in preparation
- Chang, C. W., Mycek, M. A., “Improving Precision in Fluorescence Lifetime Imaging Microscopy for Low-Light Live-Cell Imaging”, BMES 2008 Annual Fall Meeting, St. Louis, Missouri, October 2-4, 2008

Chapter 6

- Chang C.W. and M.A. Mycek, “Improving Precision in Time-Gated FLIM for Low-Light Live-Cell Imaging”, European Conferences on Biomedical Optics, Munich, Germany, June 14–18, 2009 (accepted)

7.2 Future work

Future work for further improvements includes the following:

1. For the temporal approach
    a. Consider more than three fluorescent components present in a system. This situation also happens in biological samples and, therefore, its analyses will be useful in live-cell studies.

b. Consider background and other forms of noise. In analogy to the incorporation of the *G(N)* curve in FWTV and UWTV, the background noise and other forms of noise can be included in a curve combined with the weighting of WNLLS such that WNLLS can produce better results than MLE due to the flexibility.

c. Use unfixed values of *g* and *dt* in WNLLS, MLE, and even RLD. This should give a very high chance to further improve the precision, although much more computational work and computer memories may be needed to complete this task.

2. For the spatial approach

   a. Further refine the parameters in *G(N)* curve modeling to obtain even better results for FWTV w/*G(N)* and UWTV w/*G(N)*.

   b. Increase the speed and efficiency of FWTV and UWTV by developing their constrained models for automatic estimation of fidelity coefficients.

   c. Use global denoising algorithms. The global denoising algorithms are also commonly used. For example, some of them involve using various filters for noise removal in the Fourier domain of images, while some others may involve collecting all pixel information and applying weightings to them for determination of the intensity of a specific pixel. The application of global denoising to gated FLIM images has potential and is also worth studying. It may provide a good chance of finding a even more accurate noise removal algorithm for better precision. Using local algorithms such as TV models is just the first step. Still, the procedures provided in this study for the analysis of the accuracy and precision of the lifetime determination of FLIM after

denoising may serve as a standard for future analysis on global algorithms and provide ways to compare them with local algorithms.

3. For the combined approach

    a. Conduct carefully designed experiments to confirm the hypothesis that the additive RSD reduction by the combined approach is due to the fact that the spatial denoising is more dependent on the geometry of the objects and the relative locations of pixel information in the images. This information will help us determine what types of images are most suitable for the use of the denoising in combination with the temporal optimization, such that we can combine the two approaches more effectively.

4. Others

    a. Include the temporal deconvolution (the deconvolution of signals and instrument response functions) of the fluorescence decay curves detected by our FLIM system. This can be incorporated into our data processing procedure. Although it does not affect conclusions of detected cellular and molecular responses inferred by relative comparisons of lifetime values, it will definitely change the absolute values of calculated lifetimes. Therefore, it improves the accuracy of lifetime determination in FLIM systems.

7.3 Potential applications

This work can be applied to the construction of quantitative models for potential clinical use. While some models are constructed at tissue levels, other fundamental models for predicting the dynamics of treatments are based on intra-cellular and molecular responses in living cells [22]. These responses may rely on, for example, kinetic parameters such as protein / messenger RNA production and decay rates, or

dimerization and cleavage rates such as those in cell apoptotic pathways [1, 23], since those parameters may trigger an imbalance between pro-cancer and anti-cancer factors. Such information may also be incorporated to more detailed genetic models such as those used in system biology and bioinformatics [24]. While a detailed model can help us predict the level of certain crucial molecules, a simplified model helps us to predict overall dynamics and the change of dynamics. In both of these cases, more accurate and precise quantification and localization of molecules in living cells is critical. Our improved FLIM can be applied for this purpose.

Analysis of fluorescence lifetimes and denoising of images acquired from tissues and cellular matrices may also be a potential application. Although time-gated FLIM provides high-speed snap shots of lifetime distributions, it may not provide deep penetration into thick tissues, because time-gated FLIM usually requires a wide-field system, where, if thick tissue is used, the fluorophores outside the focal plane are also excited by the light sources, and the emitted light from them is also received by the detector, blurring the resulting images. This problem is sometimes circumvented by using other microscopy techniques. For example, raster scanned confocal or multi-photon microscopy can be combined with a lifetime technique such as time-correlated single photon counting (TCSPC). In this case, better light penetration ability and higher resolution can be achieved at cost of higher focused light energy and longer dwell time for excitation as well as longer data processing times. TCSPC is a commercially available and very popular technique used for time-domain FLIM [17]. In TCSPC, single photons received by detectors are used to construct histograms with hundreds or thousands of channels to reveal the shapes of exponential decay curves. TCSPC data can be time-integrated (i.e. “virtually gated” for the data points corresponding to the histogram channels) for higher processing speed. Our temporal and spatial approaches can be applied here.

While optimal gating can improve the precision of virtual gating, the images formed under each virtual gate can be denoised with our novel TV models. This gives us a good chance to improve the precision of TCSPC, especially when low-light excitation is required. This, therefore, significantly broadens the potential applications of our approaches to commercially available TCSPC, confocal FLIM, and multi-photon FLIM, which can be used for imaging of tissue and cellular matrices.

Our novel TV denoising models can be easily applied to other biomedical imaging systems such as 3D confocal microscopy [78], computed tomography (CT) [79], and positron emission tomography (PET) [80].

Figure 7-1 demonstrates an example of quantitative parametric PET imaging of a human brain using ^{11}C-Raclopride [80]. The first three images (Hann, ramp, and Van Cittert) were reconstructed by Tohka et al. and the last one (ramp with FWTV) was produced with our FWTV model. The data were reconstructed with the filtered backprojection (FBP) with the Hanning filter (denoted as 'Hann' in Figure 7-1). For the comparison purposes, the images were also reconstructed with the FBP and the ramp filter (denoted as 'ramp' in Figure 7-1). These reconstruction filters represent the two extremes in terms of the resolution/noise tradeoff. Namely, the Hann filter produces images with a low noise level but with a poor resolution. The ramp filter produces noisy images with a good resolution. The reblurred Van Cittert iteration (denoted as 'Van Cittert' in Figure 7-1) included spatial deconvolution (the deconvolution of the signals and point spread functions, described further below) and assumed the noise process is Gaussian. The 'Van Cittert' method was considered by Tohka et al. to be the best method in their study. Indeed, 'Van Cittert' produces an image that has better resolution than 'Hann' and less noise than 'ramp'.

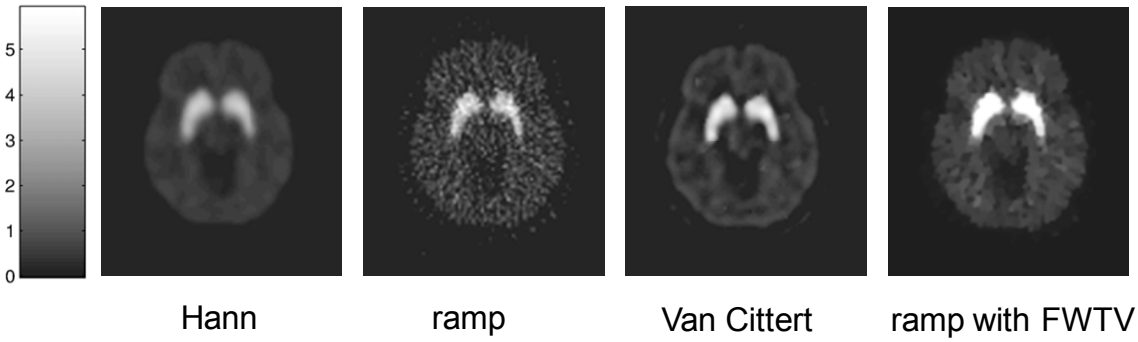

Figure 7-1 Quantitative parametric PET imaging of a human brain using ^{11}C-Raclopride. The data were reconstructed with the filtered backprojection (FBP) with the Hanning filter (denoted as 'Hann'). For the comparison purposes, the images were also reconstructed with the FBP and the ramp filter (denoted as 'ramp'). The reblurred Van Cittert iteration (denoted as 'Van Cittert') included spatial deconvolution and assumed the noise process is Gaussian. Our novel FWTV was applied to the 'ramp' image to produce the 'ramp with FWTV' image with a constant G(N) = 1.0. The images are properly scaled for better comparisons. [80]

After we applied our novel FWTV model to denoise the 'ramp' image, we found that we could actually produce an image with significantly reduced noise compared to 'ramp', and, surprisingly, also with enhanced resolution compared to 'Van Cittert'. The sharper image produced by FWTV should be attributed to the ability of our model to preserve edges. Although Tohka et al. also included a basic TV term in one of their methods, it failed to produce a desirable image probably due to the fact that Tohka et al. used a fixed fidelity term without considering the discrepancy rule. Another thing worth noting in Figure 7-1 is that the Van Cittert method has a very obvious 'ringing' artifact (the edge with brighter signals), which occurs very commonly during deconvolution possibly due to inappropriate denoising. This kind of artifact does not exist in our FWTV-denoised image.

For the 'ramp with FWTV' image in Figure 7-1, we assume a constant $G(N)$ = 1.0 in the FWTV denoising process, meaning that the intensity counts follow exactly the Poisson distribution. This also implies that if we can further obtain a better estimation of the PET system gain value, we indeed will have a greater chance to produce an even better image. As for a non-constant $G(N)$ curve, as we used in the previous chapters, it has been reported that noise distribution in PET can be characterized in a similar way

[116], and this further enhances our ability to better process PET images, although the shapes of *G(N)* curves may depend on individual PET systems. Theoretically, as long as the magnitude of intensity variation can be evaluated, FWTV and UWTV can accurately remove the variations. However, practically, the distribution of noise around the expected magnitude, the geometrical information, or any spatially-dependent noise magnitude, as well as other factors, may all play a role in the effectiveness of denoising. Further investigation of these issues will be of particular interest for generalized use of denoising models.

Finally, another potential application is that the TV denoising algorithms can be combined with spatial deconvolution. Spatial (or image) deconvolution is a computational technique that can improve the resolution of images. This technique was demonstrated to have the ability to improve our FLIM results [117]. Theoretically, deconvolution can be simply achieved with the inverse operation of convolution. However, the difficulties in the implementation of deconvolution in real-system images arise from the need to remove the noise in the images, such that the noise will not be amplified in the deconvolution process. Therefore, noise estimation and removal can be a huge issue and can greatly affect the results in image deconvolution. The characterization of various kinds of noise with *G(N)* curves, developed in this study, can be combined with the denoising algorithms along with deconvolution. This will greatly help the accuracy of deconvolution for better image resolution in images from not only our gated FLIM system, but also other imaging systems where point spread functions can be defined, such as the imaging systems mentioned above (confocal microscopy, CT, and PET).

Appendix

A.1 Estimates of J(*o*), F(*o*), and U(*o*)

In this section, we develop an approach to estimate J(*o*), F(*o*), and U(*o*). This is a practical issue, since original images without noise are always unavailable in practice.

We can estimate J(*o*), F(*o*), and U(*o*) by using J(*f**), F(*f**), and U(*f**), respectively, with *f** = poissrnd(*f*) (adding Poisson-distributed noise to *f*). First, a more detailed analysis regarding J(*f**) is as follows.

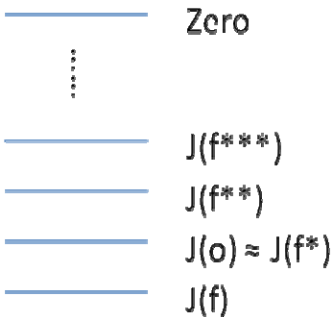

Figure A-1 The schematic illustration of the relative positions of J(*o*), J(*f*), J(*f**), J(*f***), J(*f****), and zero

The relations among J(*f*), J(*o*), and (*f**) are shown in Figure A-1. Also shown are J(*f***) and J(*f****), where, *f*** = poissrnd(*f**), *f**** = poissrnd(*f***) and so on. The "distance" in each step, or the difference of J() values between two consecutive images away from each other with only one Poisson random number generation, is quite fixed. For example, with the first gate image, we have

$J(f^{***}) = -1.3697577 \times 10^4$

$J(f^{**}) = -1.3697686 \times 10^4$, 0.109 from above

$J(f^{*}) = -1.3697789 \times 10^4$, 0.103 from above

$J(o) = -1.3697794 \times 10^4$, 0.005 from above

$J(f) = -1.3697903 \times 10^4$, 0.109 from above

In another example, with the second gate image, we have

$J(f^{*}) = -8.687436 \times 10^3$

$J(o) = -8.687436 \times 10^3$, <0.001 from above

$J(f) = -8.687551 \times 10^3$, 0.115 from above

Therefore, f^* indeed can be used to estimate $J(o)$.

To understand this phenomenon theoretically, let us consider

$J(f^{*}) \approx J(o)$

$\leftrightarrow -\log [(P(f|f^{*})] \approx -\log [(P(f|o)]$

$\leftrightarrow P_{f^{*}}(f) \approx P_o(f)$ (under Poisson probability density function)

Since $O \xrightarrow{Poissonrnd} f \xrightarrow{Poissonrnd} f^{*}$, it is clear that we have $P_f(f^{*}) \approx P_o(f)$. However, to get $P_{f^{*}}(f) \approx P_f(f^{*})$, the assumption is that the difference between f^* and f need to be relatively small compared to themselves, which usually holds for sufficiently large f. The reason is described below.

One property of Poisson distribution that may play a role here is that the mode of this distribution is λ and λ - 1, where λ here is the expected value or the input value for poissrnd(), and the probability of getting a value lower than λ is higher than getting a value higher than λ (although the mean value is still λ). Of course, this effect becomes

obvious only when f is small. For example, with poisspdf(x, λ) (the probability of getting x from poissrnd(λ)),

poisspdf(90,100) = 0.0250

poisspdf(100,90) = 0.0233

poisspdf(9900,10000) = 0.002427806706562

poisspdf(10000,9900) = 0.002411574108733

This in turn means that it is more probable that the values of f^* are smaller than those of f, and we will have $P_{f^*}(f) < P_f(f^*)$. Still, when using $J(f^*)$ to estimate $J(o)$, even if f has low intensities, summation of large number of pixels still gives good approximation since the mean value does not have any bias.

As for using $F(f^*)$ and $U(f^*)$ to estimate $F(o)$ and $U(o)$, this probably can be understood by realizing that the distances between f^* and f and between o and f are similar under certain norms. One test shows that when $F(o) = 0.4536$, $F(f^*) = 0.4596$, 0.4477, and 0.4575 (three trials with the same f). Another test shows that when $U(o) = 0.4771$, $U(f^*) = 0.4573$, 0.4750, and 0.4629 (three trials with the same f) while $U(f^{**}) = 0.6459$ and $U(f^{***}) = 0.8022$. It is possible that $F(f^*)$ can predict $F(o)$ better than $U(f^*)$ predicts $U(o)$, since the difference between f^* and o (relative to f) only affects the numerator in F() but both numerator and denominator in U().

References

1. Rehm, M., H. Dussmann, R.U. Janicke, J.M. Tavare, D. Kogel, and J.H.M. Prehn, *Single-cell fluorescence resonance energy transfer analysis demonstrates that caspase activation during apoptosis is a rapid process - Role of caspase-3.* Journal of Biological Chemistry, 2002. **277**(27): p. 24506-24514.
2. Fussenegger, M., J.E. Bailey, and J. Varner, *A mathematical model of caspase function in apoptosis.* Nature Biotechnology, 2000. **18**(7): p. 768-774.
3. Albeck, J.G., J.M. Burke, B.B. Aldridge, M.S. Zhang, D.A. Lauffenburger, and P.K. Sorger, *Quantitative analysis of pathways controlling extrinsic apoptosis in single cells.* Molecular Cell, 2008. **30**(1): p. 11-25.
4. Kramer, B.P. and M. Fussenegger, *Hysteresis in a synthetic mammalian gene network.* Proceedings of the National Academy of Sciences of the United States of America, 2005. **102**(27): p. 9517-9522.
5. Rao, B.M., D.A. Lauffenburger, and K.D. Wittrup, *Integrating cell-level kinetic modeling into the design of engineered protein therapeutics.* Nature Biotechnology, 2005. **23**(2): p. 191-194.
6. Lees, P., F.M. Cunningham, and J. Elliott, *Principles of pharmacodynamics and their applications in veterinary pharmacology.* Journal of Veterinary Pharmacology and Therapeutics, 2004. **27**(6): p. 397-414.

7. Steimer, J.L., M.E. Ebelin, and J. Van Bree, *Pharmacokinetic and pharmacodynamic data and models in clinical trials.* Eur J Drug Metab Pharmacokinet, 1993. **18**(1): p. 61-76.

8. Chien, J.Y., S. Friedrich, M.A. Heathman, D.P. de Alwis, and V. Sinha, *Pharmacokinetics/pharmacodynamics and the stages of drug development: Role of modeling and simulation.* Aaps Journal, 2005. **7**(3): p. E544-E559.

9. Dartois, C., K. Brendel, E. Comets, C.M. Laffont, C. Laveille, B. Tranchand, F. Mentre, A. Lemenuel-Diot, and P. Girard, *Overview of model-building strategies in population PK/PD analyses: 2002-2004 literature survey.* British Journal of Clinical Pharmacology, 2007. **64**(5): p. 603-612.

10. Proost, J.H., S. Schiere, D.J. Eleveld, and J.M.K.H. Wierda, *Simultaneous versus sequential pharmacokinetic-pharmacodynamic population analysis using an iterative two-stage Bayesian technique.* Biopharmaceutics & Drug Disposition, 2007. **28**(8): p. 455-473.

11. Tanaka, C., T. O'Reilly, J.M. Kovarik, N. Shand, K. Hazell, I. Judson, E. Raymond, S. Zumstein-Mecker, C. Stephan, A. Boulay, M. Hattenberger, G. Thomas, and H.A. Lane, *Identifying optimal biologic doses of everolimus (RAD001) in patients with cancer based on the modeling of preclinical and clinical pharmacokinetic and pharmacodynamic data.* J Clin Oncol, 2008. **26**(10): p. 1596-602.

12. Shaw, L.M., H.S. Bonner, L. Fields, and R. Lieberman, *The Use of Concentration Measurements of Parent Drug and Metabolites during Clinical-Trials.* Therapeutic Drug Monitoring, 1993. **15**(6): p. 483-487.

13. Wang, S.N., P. Guo, X.M. Wang, Q.Y. Zhou, and J.M. Gallo, *Preclinical pharmacokinetic/pharmacodynamic models of gefitinib and the design of*

equivalent dosing regimens in EGFR wild-type and mutant tumor models. Molecular Cancer Therapeutics, 2008. **7**(2): p. 407-417.

14. Werner, E., *In silico multicellular systems biology and minimal genomes.* Drug Discov Today, 2003. **8**(24): p. 1121-7.
15. Lakowicz, J.R., *Principles of Fluorescence Spectroscopy*. 2nd ed. 1999, New York: Kluwer Academic/Plenum.
16. Rudolph, W. and M. Kempe, *Trends in optical biomedical imaging.* Journal of Modern Optics, 1997. **44**(9): p. 1617-1642.
17. Chang, C.W., D. Sud, and M.A. Mycek, *Fluorescence lifetime imaging microscopy.* Methods Cell Biol, 2007. **81**: p. 495-524.
18. Lakowicz, J.R., *Principles of Fluorescence Spectroscopy*. 2nd Edition ed. 2004: Springer.
19. Takanishi, C.L., E.A. Bykova, W. Cheng, and J. Zheng, *GFP-based FRET analysis in live cells.* Brain Res, 2006. **1091**(1): p. 132-9.
20. Tsien, R.Y., *The green fluorescent protein.* Annual Review of Biochemistry, 1998. **67**: p. 509-544.
21. Zal, T. and N.R. Gascoigne, *Photobleaching-corrected FRET efficiency imaging of live cells.* Biophys J, 2004. **86**(6): p. 3923-39.
22. Derheimer, F.A., C.W. Chang, and M. Ljungman, *Transcription inhibition: A potential strategy for cancer therapeutics.* European Journal of Cancer, 2005. **41**(16): p. 2569-2576.
23. Hellwig, C.T., B.F. Kohler, A.K. Lehtivarjo, H. Dussmann, M.J. Courtney, J.H.M. Prehn, and M. Rehm, *Real time analysis of tumor necrosis factor-related apoptosis-inducing ligand/cycloheximide-induced caspase activities during apoptosis initiation.* Journal of Biological Chemistry, 2008. **283**(31): p. 21676-21685.

24. Hsu, C.P., P.H. Lee, C.W. Chang, and C.T. Lee, *Constructing quantitative models from qualitative mutant phenotypes: preferences in selecting sensory organ precursors.* Bioinformatics, 2006. **22**(11): p. 1375-1382.

25. Jepson, M.A., *Advances in fluorescence imaging: opportunities for pharmaceutical science - Preface.* Advanced Drug Delivery Reviews, 2005. **57**(1): p. 1-4.

26. Errington, R.J., S.M. Ameer-beg, B. Vojnovic, L.H. Patterson, M. Zloh, and P.J. Smith, *Advanced microscopy solutions for monitoring the kinetics and dynamics of drug-DNA targeting in living cells.* Advanced Drug Delivery Reviews, 2005. **57**(1): p. 153-167.

27. Mager, D.E. and D.R. Abernethy, *Use of wavelet and fast Fourier transforms in pharmacodynamics.* Journal of Pharmacology and Experimental Therapeutics, 2007. **321**(2): p. 423-430.

28. Braun, D.C., S.H. Garfield, and P.M. Blumberg, *Analysis by fluorescence resonance energy transfer of the interaction between ligands and protein kinase C delta in the intact cell.* Journal of Biological Chemistry, 2005. **280**(9): p. 8164-8171.

29. Konig, K., T.W. Becker, P. Fischer, I. Riemann, and K.J. Halbhuber, *Pulse-length dependence of cellular response to intense near-infrared laser pulses in multiphoton microscopes.* Optics Letters, 1999. **24**(2): p. 113-115.

30. Rau, K.R., A. Guerra, A. Vogel, and V. Venugopalan, *Investigation of laser-induced cell lysis using time-resolved imaging.* Applied Physics Letters, 2004. **84**(15): p. 2940-2942.

31. Urayama, P.K. and M.A. Mycek, *Fluorescence lifetime imaging microscopy of endogenous biological fluorescence*, in *Handbook of Biomedical Fluorescence*, M.A. Mycek and B.W. Pogue, Editors. 2003, Marcel Dekker, Inc.: New York.

32. Zhong, W., M. Wu, C.W. Chang, K.A. Merrick, S.D. Merajver, and M.A. Mycek, *Picosecond-resolution fluorescence lifetime imaging microscopy: a useful tool for sensing molecular interactions in vivo via FRET.* Optics Express, 2007. **15**(26): p. 18220-18235.

33. Zhong, W., *Developing a Novel Fluorescence Lifetime Imaging Microscope with Applications to Sensing Metabolic Function and Oncogene Activity in vivo*, in *Biomedical Engineering*. 2005, University of Michigan: Ann Arbor. p. 115.

34. Piston, D.W. and G.J. Kremers, *Fluorescent protein FRET: the good, the bad and the ugly.* Trends in Biochemical Sciences, 2007. **32**(9): p. 407-414.

35. Vogel, S.S., C. Thaler, and S.V. Koushik, *Fanciful FRET.* Sci STKE, 2006. **2006**(331): p. re2.

36. Berney, C. and G. Danuser, *FRET or no FRET: a quantitative comparison.* Biophys J, 2003. **84**(6): p. 3992-4010.

37. Koushik, S.V., H. Chen, C. Thaler, H.L. Puhl, 3rd, and S.S. Vogel, *Cerulean, Venus, and VenusY67C FRET reference standards.* Biophys J, 2006. **91**(12): p. L99-L101.

38. Shaner, N.C., P.A. Steinbach, and R.Y. Tsien, *A guide to choosing fluorescent proteins.* Nature Methods, 2005. **2**(12): p. 905-909.

39. Tsai, P.S., B. Friedman, A.I. Ifarraguerri, B.D. Thompson, V. Lev-Ram, C.B. Schaffer, C. Xiong, R.Y. Tsien, J.A. Squier, and D. Kleinfeld, *All-optical histology using ultrashort laser pulses.* Neuron, 2003. **39**(1): p. 27-41.

40. Louie, T.M., R.S. Jones, A.V. Sarma, and D. Fried, *Selective removal of composite sealants with near-ultraviolet laser pulses of nanosecond duration.* J Biomed Opt, 2005. **10**(1): p. 14001.

41. Konig, K., *Laser tweezers and multiphoton microscopes in life sciences.* Histochemistry and Cell Biology, 2000. **114**(2): p. 79-92.

42. Pelet, S., M.J. Previte, and P.T. So, *Comparing the quantification of Forster resonance energy transfer measurement accuracies based on intensity, spectral, and lifetime imaging.* J Biomed Opt, 2006. **11**(3): p. 34017.

43. Buades, A., B. Coll, and J.M. Morel, *A review of image denoising algorithms, with a new one.* Multiscale Modeling & Simulation, 2005. **4**(2): p. 490-530.

44. Osher, S., M. Burger, D. Goldfarb, J.J. Xu, and W.T. Yin, *An iterative regularization method for total variation-based image restoration.* Multiscale Modeling & Simulation, 2005. **4**(2): p. 460-489.

45. Tadmor, E., S. Nezzar, and L. Vese, *A multiscale image representation using hierarchical (BV, L2) decompositions.* Multiscale Modeling & Simulation, 2004. **2**(4): p. 554-579.

46. Urayama, P.K., W. Zhong, J.A. Beamish, F.K. Minn, R.D. Sloboda, K.H. Dragnev, E. Dmitrovsky, and M.-A. Mycek, *A UV-visible fluorescence lifetime imaging microscope for laser-based biological sensing with picosecond resolution.* Appl. Phys. B-Lasers Opt., 2003b. **76**(5): p. 483-496.

47. Sanders, R., A. Draaijer, H.C. Gerritsen, P.M. Houpt, and Y.K. Levine, *Quantitative pH imaging in cells using confocal fluorescence lifetime imaging microscopy.* Analytical Biochemistry, 1995. **227**(2): p. 302-308.

48. Lin, H.J., P. Herman, and J.R. Lakowicz, *Fluorescence lifetime-resolved pH imaging of living cells.* Cytometry A, 2003. **52**(2): p. 77-89.

49. Sud, D., W. Zhong, D.G. Beer, and M.-A. Mycek, *Time-resolved optical imaging provides a molecular snapshot of altered metabolic function in living human cancer cell models.* Optics Express, 2006. **14**(10): p. 4412-4426.

50. Gerritsen, H.C., R. Sanders, A. Draaijer, and Y.K. Levine, *Fluorescence lifetime imaging of oxygen in living cells.* Journal of Fluorescence, 1997. **7**: p. 11-16.

51. Lakowicz, J.R., H. Szmacinski, K. Nowaczyk, and M.L. Johnson, *Fluorescence lifetime imaging of free and protein-bound NADH.* Proc Natl Acad Sci U S A, 1992. **89**(4): p. 1271-5.

52. Oida, T., Y. Sako, and A. Kusumi, *Fluorescence lifetime imaging microscopy (flimscopy) - methodology development and application to studies of endosome fusion in single cells.* Biophysical Journal, 1993. **64**(3): p. 676-685.

53. French, T., P.T.C. So, C.Y. Dong, K.M. Berland, and E. Gratton, *Fluorescence lifetime imaging techniques for microscopy.* Methods in Cell Biology, 1998. **56**: p. 277-304.

54. Gadella, T.W.J., Jr., *Fluorescence lifetime imaging microscopy (FLIM): Instrumentation and application*, in *Fluorescent and Luminescent Probes for Biological Activity*, W.T. Masons, Editor. 1999, Academic Press: San Diego. p. 467-479.

55. Tadrous, P.J., *Methods for imaging the structure and function of living tissues and cells: 2. Fluorescence lifetime imaging.* Journal of Pathology, 2000. **191**(3): p. 229-234.

56. Wang, X.F., A. Periasamy, B. Herman, and D. Coleman, *Fluorescence lifetime imaging microscopy (FLIM): Instrumentation and applications.* Critical Reviews in Analytical Chemistry, 1992. **23**(5): p. 369-395.

57. Requejo-Isidro, J., J. McGinty, I. Munro, D.S. Elson, N.P. Galletly, M.J. Lever, M.A.A. Neil, G.W.H. Stamp, P.M.W. French, P.A. Kellett, J.D. Hares, and A.K.L. Dymoke-Bradshaw, *High-speed wide-field time-gated endoscopic fluorescence-lifetime imaging.* Optics Letters, 2004. **29**(19): p. 2249-2251.

58. Munro, I., J. McGinty, N. Galletly, J. Requejo-Isidro, P.M. Lanigan, D.S. Elson, C. Dunsby, M.A. Neil, M.J. Lever, G.W. Stamp, and P.M. French, *Toward the*

clinical application of time-domain fluorescence lifetime imaging. J Biomed Opt, 2005. **10**(5): p. 051403.

59. Cano-Raya, C., M.D.F. Ramos, L.F.C. Vallvey, O.S. Wolfbeis, and M. Schaferling, *Fluorescence quenching of the europium tetracycline hydrogen peroxide complex by copper(II) and other metal ions.* Applied Spectroscopy, 2005. **59**(10): p. 1209-1216.

60. Xu, Z., M. Raghavan, T.L. Hall, C.W. Chang, M.A. Mycek, J.B. Fowlkes, and C.A. Cain, *High speed imaging of bubble clouds generated in pulsed ultrasound cavitational therapy-histotripsy.* Ieee Transactions on Ultrasonics Ferroelectrics and Frequency Control, 2007. **54**(10): p. 2091-2101.

61. Bugiel, I., K. König, and H. Wabnitz, *Investigation of cell by fluorescence laser scanning microscopy with subnanosecond time resolution.* Lasers in the Life Sciences, 1989. **3**(1): p. 47-53.

62. Wang, X.F., T. Uchida, D.M. Coleman, and S. Minami, *A two-dimensional fluorescence lifetime imaging system using a gated image intensifier.* Applied Spectroscopy, 1991. **45**(3): p. 360-366.

63. Sharman, K.K., A. Periasamy, H. Ashworth, J.N. Demas, and N.H. Snow, *Error analysis of the rapid lifetime determination method for double-exponential decays and new windowing schemes.* Analytical Chemistry, 1999. **71**(5): p. 947-952.

64. Rasnik, I., T. French, K. Jacobson, and K. Berland, *Electronic cameras for low-light microscopy.* Methods Cell Biol, 2007. **81**: p. 219-49.

65. Moomaw, B., *Camera technologies for low light imaging: overview and relative advantages.* Methods Cell Biol, 2007. **81**: p. 251-83.

66. Frenkel, A., M.A. Sartor, and M.S. Wlodawski, *Photon-noise-limited operation of intensified CCD cameras.* Applied Optics, 1997. **36**(22): p. 5288-5297.

67. Ballew, R.M. and J.N. Demas, *An Error Analysis of the Rapid Lifetime Determination Method for the Evaluation of Single Exponential Decays.* Analytical Chemistry, 1989. **61**(1): p. 30-33.

68. Waters, P.D. and D.H. Burns, *Optimized Gated Detection for Lifetime Measurement over a Wide-Range of Single Exponential Decays.* Applied Spectroscopy, 1993. **47**(1): p. 111-115.

69. Hall, P. and B. Selinger, *Better Estimates of Exponential Decay Parameters.* Journal of Physical Chemistry, 1981. **85**(20): p. 2941-2946.

70. Moore, C., S.P. Chan, J.N. Demas, and B.A. DeGraff, *Comparison of methods for rapid evaluation of lifetimes of exponential decays.* Applied Spectroscopy, 2004. **58**(5): p. 603-607.

71. Soper, S.A. and B.L. Legendre, *Error Analysis of Simple Algorithms for Determining Fluorescence Lifetimes in Ultradilute Dye Solutions.* Applied Spectroscopy, 1994. **48**(3): p. 400-405.

72. Edel, J.B., J.S. Eid, and A. Meller, *Accurate single molecule FRET efficiency determination for surface immobilized DNA using maximum likelihood calculated lifetimes.* Journal of Physical Chemistry B, 2007. **111**(11): p. 2986-2990.

73. Maus, M., M. Cotlet, J. Hofkens, T. Gensch, F.C. De Schryver, J. Schaffer, and C.A.M. Seidel, *An experimental comparison of the maximum likelihood estimation and nonlinear least squares fluorescence lifetime analysis of single molecules.* Analytical Chemistry, 2001. **73**(9): p. 2078-2086.

74. Nishimura, G. and M. Tamura, *Artefacts in the analysis of temporal response functions measured by photon counting.* Physics in Medicine and Biology, 2005. **50**(6): p. 1327-1342.

75. Esposito, A., H.C. Gerritsen, and F.S. Wouters, *Optimizing frequency-domain fluorescence lifetime sensing for high-throughput applications: photon economy*

and acquisition speed. Journal of the Optical Society of America a-Optics Image Science and Vision, 2007. **24**(10): p. 3261-3273.

76. Chan, S.P., Z.J. Fuller, J.N. Demas, and B.A. DeGraff, *Optimized gating scheme for rapid lifetime determinations of single-exponential luminescence lifetimes.* Analytical Chemistry, 2001. **73**(18): p. 4486-4490.

77. de Grauw, C.J. and H.C. Gerritsen, *Multiple time-gate module for fluorescence lifetime imaging.* Applied Spectroscopy, 2001. **55**(6): p. 670-678.

78. Dey, N., L. Blanc-Feraud, C. Zimmer, P. Roux, Z. Kam, J.C. Olivo-Marin, and J. Zerubia, *Richardson-Lucy algorithm with total variation regularization for 3D confocal microscope deconvolution.* Microscopy Research and Technique, 2006. **69**(4): p. 260-266.

79. Wu, C.N., Y. Cheng, M.L. Liu, and Y. Jin, *Measurement of axisymmetric two-phase flows by an improved x-ray-computed tomography technique.* Industrial & Engineering Chemistry Research, 2008. **47**(6): p. 2063-2074.

80. Tohka, J. and A. Reilhac, *Deconvolution-based partial volume correction in Raclopride-PET and Monte Carlo comparison to MR-based method.* Neuroimage, 2008. **39**(4): p. 1570-1584.

81. Sofou, A. and P. Maragos, *Generalized flooding and multicue PDE-based image segmentation.* Ieee Transactions on Image Processing, 2008. **17**(3): p. 364-376.

82. Nilsson, B., M. Johansson, A. Heyden, S. Nelander, and T. Fioretos, *An improved method for detecting and delineating genomic regions with altered gene expression in cancer.* Genome Biol, 2008. **9**(1): p. R13.

83. Rudin, L.I., S. Osher, and E. Fatemi, *Nonlinear Total Variation Based Noise Removal Algorithms.* Physica D, 1992. **60**(1-4): p. 259-268.

84. Le, T., R. Chartrand, and T.J. Asaki, *A variational approach to reconstructing images corrupted by poisson noise.* Journal of Mathematical Imaging and Vision, 2007. **27**(3): p. 257-263.

85. Förster, T., *Intermolecular energy migration and fluorescence.* Ann. Phys. (Leitzig), 1948. **2**: p. 55-75.

86. Kreiss, P., B. Cameron, R. Rangara, P. Mailhe, O. Aguerre-Charriol, M. Airiau, D. Scherman, J. Crouzet, and B. Pitard, *Plasmid DNA size does not affect the physicochemical properties of lipoplexes but modulates gene transfer efficiency.* Nucleic Acids Research, 1999. **27**(19): p. 3792-3798.

87. Ross, P.C. and S.W. Hui, *Lipoplex size is a major determinant of in vitro lipofection efficiency.* Gene Therapy, 1999. **6**(4): p. 651-659.

88. Schmid, J.A. and H.H. Sitte, *Fluorescence resonance energy transfer in the study of cancer pathways.* Current Opinion in Oncology, 2003. **15**: p. 55-64.

89. Wallrabe, H. and A. Periasamy, *Imaging protein molecules using FRET and FLIM microscopy.* Curr Opin Biotechnol, 2005. **16**(1): p. 19-27.

90. Chen, Y., M. Elangovan, and A. Periasamy, *FRET Data Analysis: The Algorithm*, in *Molecular Imaging*, A. Periasamy and R.N. Day, Editors. 2005, Oxford University Press: New York. p. 126-145.

91. Demarco, I.A., A. Periasamy, C.F. Booker, and R.N. Day, *Monitoring dynamic protein interactions with photoquenching FRET.* Nature Methods, 2006. **3**(7): p. 519-524.

92. Hoppe, A., K. Christensen, and J.A. Swanson, *Fluorescence resonance energy transfer-based stoichiometry in living cells.* Biophysical Journal, 2002. **83**(6): p. 3652-3664.

93. Chen, Y., J.D. Mills, and A. Periasamy, *Protein localization in living cells and tissues using FRET and FLIM.* Differentiation, 2003. **71**(9-10): p. 528-541.

94. Urayama, P., W. Zhong, J.A. Beamish, F.K. Minn, R.D. Sloboda, K.H. Dragnev, E. Dmitrovsky, and M.A. Mycek, *A UV-visible-NIR fluorescence lifetime imaging microscope for laser-based biological sensing with picosecond resolution.* Applied Physics B-Lasers and Optics, 2003. **76**(5): p. 483-496.

95. Provenzano, P.P., K.W. Eliceiri, and P.J. Keely, *Multiphoton microscopy and fluorescence lifetime imaging microscopy (FLIM) to monitor metastasis and the tumor microenvironment.* Clin Exp Metastasis, 2008.

96. Yi, Y.H., P.Y. Ho, T.W. Chen, W.J. Lin, V. Gukassyan, T.H. Tsai, D.W. Wang, T.S. Lew, C.Y. Tang, S.J. Lo, T.Y. Chen, F.J. Kao, and C.H. Lin, *Membrane Targeting and Coupling of NHE1-Integrin{alpha}IIb{beta}3-NCX1 by Lipid Rafts following Integrin-Ligand Interactions Trigger Ca2+ Oscillations.* J Biol Chem, 2009. **284**(6): p. 3855-64.

97. Chen, Y. and A. Periasamy, *Characterization of two-photon excitation fluorescence lifetime imaging microscopy for protein localization.* Microsc Res Tech, 2004. **63**(1): p. 72-80.

98. Vermeer, J.E., E.B. Van Munster, N.O. Vischer, and T.W. Gadella, Jr., *Probing plasma membrane microdomains in cowpea protoplasts using lipidated GFP-fusion proteins and multimode FRET microscopy.* J Microsc, 2004. **214**(Pt 2): p. 190-200.

99. Ng, T., A. Squire, G. Hansra, F. Bornancin, C. Prevostel, A. Hanby, W. Harris, D. Barnes, S. Schmidt, H. Mellor, P.I. Bastiaens, and P.J. Parker, *Imaging protein kinase Calpha activation in cells.* Science, 1999. **283**(5410): p. 2085-9.

100. van Golen, K.L., Z.F. Wu, X.T. Qiao, L.W. Bao, and S.D. Merajver, *RhoC GTPase, a novel transforming oncogene for human mammary epithelial cells that partially recapitulates the inflammatory breast cancer phenotype.* Cancer Research, 2000. **60**(20): p. 5832-5838.

101. Holeiter, G., J. Heering, P. Erlmann, S. Schmid, R. Jahne, and M.A. Olayioye, *Deleted in Liver Cancer 1 Controls Cell Migration through a Dial-Dependent Signaling Pathway.* Cancer Research, 2008. **68**(21): p. 8743-8751.

102. Hoppe, A.D., S.L. Shorte, J.A. Swanson, and R. Heintzmannz, *Three-dimensional FRET reconstruction microscopy for analysis of dynamic molecular interactions in live cells.* Biophysical Journal, 2008. **95**(1): p. 400-418.

103. Pertz, O., L. Hodgson, R.L. Klemke, and K.M. Hahn, *Spatiotemporal dynamics of RhoA activity in migrating cells.* Nature, 2006. **440**(7087): p. 1069-1072.

104. Semenova, M.M., A.M.J. Maki-Hokkonen, J. Cao, V. Komarovski, K.M. Forsberg, M. Koistinaho, E.T. Coffey, and M.J. Courtney, *Rho mediates calcium-dependent activation of p38 alpha and subsequent excitotoxic cell death.* Nature Neuroscience, 2007. **10**(4): p. 436-443.

105. Hodgson, L., O. Pertz, and K.M. Hahn, *Design and optimization of genetically encoded fluorescent biosensors: GTPase biosensors.* Methods Cell Biol, 2008. **85**: p. 63-81.

106. Nakamura, T., K. Aoki, and M. Matsuda, *Monitoring spatio-temporal regulation of Ras and Rho GTPases with GFP-based FRET probes.* Methods, 2005. **37**(2): p. 146-153.

107. Ahmed, T., K. Shea, J.R.W. Masters, G.E. Jones, and C.M. Wells, *A PAK4-LIMK1 pathway drives prostate cancer cell migration downstream of HGF.* Cellular Signalling, 2008. **20**(7): p. 1320-1328.

108. Legg, J.W., C.A. Lewis, M. Parsons, T. Ng, and C.M. Isacke, *A novel PKC-regulated mechanism controls CD44-ezrin association and directional cell motility.* Nature Cell Biology, 2002. **4**(6): p. 399-407.

109. Parsons, M., J. Monypenny, S.M. Ameer-Beg, T.H. Millard, L.M. Machesky, M. Peter, M.D. Keppler, G. Schiavo, R. Watson, J. Chernoff, D. Zicha, B. Vojnovic,

and T. Ng, *Spatially distinct binding of Cdc42 to PAK1 and N-WASP in breast carcinoma cells.* Molecular and Cellular Biology, 2005. **25**(5): p. 1680-1695.

110. Rizzo, M.A., G.H. Springer, B. Granada, and D.W. Piston, *An improved cyan fluorescent protein variant useful for FRET.* Nature Biotechnology, 2004. **22**(4): p. 445-449.

111. Madaule, P., T. Furuyashiki, M. Eda, H. Bito, T. Ishizaki, and S. Narumiya, *Citron, a Rho target that affects contractility during cytokinesis.* Microscopy Research and Technique, 2000. **49**(2): p. 123-126.

112. Nakabayashi, T., H.P. Wang, K. Tsujimoto, S. Miyauchi, N. Kamo, and N. Ohta, *A correlation between pH and fluorescence lifetime of 2',7'-Bis(2-carboxyethyl)-5(6)-carboxyfluorescein (BCECF) in vivo and in vitro.* Chemistry Letters, 2007. **36**(2): p. 206-207.

113. Ryder, A.G., S. Power, and T.J. Glynn, *Evaluation of acridine in Nafion as a fluorescence-lifetime-based pH sensor.* Appl Spectrosc, 2003. **57**(1): p. 73-9.

114. Ryder, A.G., S. Power, and T.J. Glynn, *Fluorescence lifetime based pH sensing using Resorufin.* Proceedings of SPIE, 2003. **4876**.

115. Boens, N., W.W. Qin, N. Basaric, J. Hofkens, M. Ameloot, J. Pouget, J.P. Lefevre, B. Valeur, E. Gratton, M. Vandeven, N.D. Silva, Y. Engelborghs, K. Willaert, A. Sillen, G. Rumbles, D. Phillips, A.J.W.G. Visser, A. van Hoek, J.R. Lakowicz, H. Malak, I. Gryczynski, A.G. Szabo, D.T. Krajcarski, N. Tamai, and A. Miura, *Fluorescence lifetime standards for time and frequency domain fluorescence spectroscopy.* Analytical Chemistry, 2007. **79**(5): p. 2137-2149.

116. Geng, J.H., Y.M. Chen, D.Y. Yin, J.H. Tian, and S.Z. Chen, *Noise components on positron emission tomography images.* Bio-Medical Materials and Engineering, 2003. **13**(2): p. 181-186.

117. Sud, D. and M.A. Mycek, *Image restoration for fluorescence lifetime imaging microscopy (FLIM).* Optics Express, 2008. **16**(23): p. 19192-19200.